

# 江苏省研究生工作站申报书

## (企业填报)

申请设站单位全称： 阔然医学检验实验室（徐州）有限公司

单位组织机构代码： 91320300MA1XG5F726

单位所属行业： 医疗卫生

单位地址： 徐州市淮海国际港务区徐州永嘉科技园 B07 号楼

单位联系人： 刘秀财

联系电话： 18052122975

电子邮箱： 39469918@qq.com

合作高校名称： 江苏师范大学

江苏省教育厅 制  
江苏省科学技术厅 表  
2024 年 5 月

申请设站单位名称	阔然医学检验实验室(徐州)有限公司					
企业规模	中小企业	是否公益性企业				否
企业信用情况	良好	上年度研发经费投入（万）				700
专职研发人员(人)	22	其中	博士	3	硕士	5
			高级职称	10	中级职称	18
<b>市、县级科技创新平台情况</b> （重点实验室、工程技术研究中心、企业技术中心等，需提供立项批文佐证材料）						
平台名称		平台类别、级别		批准单位		获批时间
市级企业工程技术研究中心		市级		徐州市科学技术局		2021 年 9 月
市级工程研究中心		市级		徐州市发展和改革委员会		2023 年 12 月
徐州市产业研究院		市级		徐州市科学技术局		2020 年 12 月
<b>可获得优先支持情况</b> （院士工作站、博士后科研工作站，省级及以上企业重点实验室、工程技术研究中心、企业技术中心、产业技术研究院、人文社科基地等，需提供立项批文佐证材料）						
平台名称		平台类别、级别		批准单位		获批时间
市级企业工程技术研究中心		市级		徐州市科学技术局		2021 年 9 月
市级工程研究中心		市级		徐州市发展和改革委员会		2023 年 12 月
徐州市产业研究院		市级		徐州市科学技术局		2020 年 12 月

申请设站单位与合作高校已有的合作基础（分条目列出，限 1000 字以内。其中，联合承担的纵向和横向项目或合作成果限填近三年具有代表性的 3 项，需填写项目名称、批准单位、获批时间、项目内容、取得的成果等内容，并提供佐证材料）

阔然医学检验实验室（徐州）有限公司是集医疗、科研、产品销售为一体的高新技术企业，已获得国家高新技术企业、江苏省专精特新小巨人企业、长三角国家创新中心联合创新中心。公司依托大型基因测序技术平台和优质临床医学诊疗资源，打造检测技术和大数据中心的整体解决方案，覆盖肿瘤风险的评估与早期发现、用药指导、疗效监控和预后预测的肿瘤全周期检测服务，主营业务收入累计达 1.8 亿元，累计税收 400 余万元，在徐州共建立有 1 家实验室、1 家 IVD 生产工厂、1 家科技研究院。

阔然医学检验实验室（徐州）有限公司与江苏师范大学在项目联合申报、学术会议举办、学术交流等方面进行了深度合作，具体如下：

#### 1、获批在徐高校服务“343”产业发展项目 1 相

项目名称：数字免疫分析技术（gx2023013）

批准单位：徐州市财政局、徐州市科学技术局

获批时间：2023 年 12 月 28 日

项目内容：建立超高灵敏的均相数字免疫分析方法，达到亚 fM 水平的检测限，实现临床样本中稀有蛋白质标志物的精准分析。设计和搭建自动聚焦、自动扫描的多色荧光成像系统，解决多帧成像拼接和费时问题，实现单个荧光颗粒的自动扫描成像。建立机器学习识别单个量子点光谱的算法，优化信号计数程序，解决单分子免疫复合物信号甄别问题，实现单个目标蛋白质的自动计数。开展原理机的性能调试和优化工作，达到与临床检测技术相似的稳定性，实现临床血样的大批量分析和检测结果准确性评价。

取得的成果：发表学术论文 1 篇（Qingquan Zhang, Wenwen Chai, Xiaoyan Pan, Hongwei Gai, Amplification-Free Digital Immunoassay down to the Attomolar Level by Synergistic Sedimentation of Brownian Motion Suppression and Dehydration Transfer, *Anal. Chem.*, 2024, 96, 3054–3061）。

#### 2、参与江苏师范大学主办的学术论坛（医学跨学科前沿论坛暨 VIEW Medicine 期刊创刊仪式）建设

医学跨学科前沿论坛暨 VIEW Medicine 期刊创刊仪式是一个旨在促进医学领域跨学科合作和学术交流的综合活动，旨在汇集来自不同领域的医学专业人士，包括医生、研究人员、学者等，共同探讨医学领域的前沿课题和研究进展。论坛于 2023 年 11 月 26 日在江苏师范大学泉山校区举行，由 VIEW Medicine、江苏师范大学、江苏省材料学会主办，江苏师范大学化学与材料科学学院、江苏圣理工学院-中俄学院共同承办。来自中国

科技技术大学、浙江大学、复旦大学、上海交通大学等知名学府的专家、学者做了精彩的学术报告。

3、邀请江苏师范大学盖宏伟教授团队赴阔然医学检验实验室（徐州）有限公司总部和生产基地进行参观、指导和学术交流。



## 工作站条件保障情况

1.人员保障条件（包括高校和企业能指导研究生科研创新实践的专业技术或管理专家等情况）

阔然医学检验实验室建设有国内先进的 **NGS**（二代测序）平台，主要从事基因组学、蛋白质组学、表型组学的研究，开展肿瘤免疫微环境、肿瘤分子诊断等临床测序研究。公司首创 **NGP**（下一代病理）和 **NGS** 的临床应用平台，注重临床分子诊断试剂的研发，聘任大量高级职称专家，其丰富的科研经验和临床指导教学经验为在站研究生的培养提供指导和保障，具体如下：

李莉教授，阔然精准研究院外聘专家，博士生导师，上海市第一人民医院检验医学中心，学科带头人，美国匹兹堡大学医学院访问学者。

周文涛博士，公司创新研究院院长，毕业于中国科学院分子细胞科学卓越创新中心，在 *Nature Plant* 等杂志发表过多篇研究论文，拥有 10 余年 **NGS** 基因检测技术研发经验，熟悉 cfDNA、外泌体和 CTC 液体活检、液相杂交捕获、单细胞测序、分子检测自动化等技术，负责公司前沿分子诊断技术研发和产品开发，带领团队突破液体活检底层技术，研发出 **Tumor-informed + Tumor naïve** 双策略融合的微小病灶残留（MRD）检测产品。

陈鑫泽博士，公司创新研究院执行副院长，毕业于上海大学，有丰富的 **NGS** 临检项目管理及实验室生产管理经验，兼任徐州 **NGS** 生产实验室技术主管，组织研发微量核酸检测技术。

柴燕群博士，毕业于上海交大学生物化学与分子生物学专业，先后从事生物医药科研开发和服务，肿瘤精准医疗检测产品开发和转化，第三方医学实验室质量和运营管理等管理工作。担任实验室主任岗位，负责阔然实验室质量和项目管理。

江苏师范大学化学与材料科学学院，化学学科和材料科学学科均进入 **ESI** 排名 **1%**。化学专业 2019 年获批国家一流专业建设点，江苏省高校首批品牌专业、重点专业和特色专业。近年来，化学学科通过建设科研平台、组建科研团队、凝练科研方向，在功能杂环化合物的高效合成和杂环骨架的定向选择性构筑；疾病标志物的高灵敏检测；光敏金属有机材料的合成等领域取得显著进展。五年来，发表 **SCI** 论文近 400 余篇，其中二区以上 100 余篇，包括 *Journal of the American Chemical Society*, *Angewandte Chemie International Edition*, *Proceedings of the National Academy of Sciences of the United States of America* 等国际顶尖期刊。盖宏伟教授团队隶属于化学与材料科学学院，主要从事疾病标志物的高灵敏检测研究，团队成员均为博士和硕士生导师，既具有丰富的学术积累和扎实的科研功底，又具有指导和管理研究生的经验，可为在站研究生提供指导和帮助，团

队成员如下:

盖宏伟教授,理学博士,硕士生导师,主要从事单分子荧光检测和免疫分析研究。以显微成像为手段,在细胞和单分子层面开展以高灵敏检测和动态监测为特征的疾病早期诊断和致病机理研究。已发表 SCI 收录学术论文 50 多篇,多数发表于 *Anal Chem*, *Angew Chem Int Ed* 等国际权威刊物。申请发明专利 10 余项,已授权 9 项。出版《数字免疫分析》专著一部。主持国家自然科学基金面上项目 3 项、青年项目 1 项,江苏省高校自然科学研究重大项目 1 项。获得淮海科学技术奖(一等奖),江苏省分析测试协会科学技术奖(特等奖)。江苏省高校优秀科技创新团队负责人,江苏省高校“青蓝工程”中青年学术带头人,江苏省第五期“333 高层次人才培养工程”第三层次,江苏省“六大人才高峰”高层次人才。第十六届徐州市政协委员。第九届徐州市云龙区政协常委。

张清泉教授,理学博士,硕士生导师,主要从事微流控芯片的技术开发,高灵敏数字免疫分析技术的开发,以及微流控和数字免疫在临床检测方面的应用研究,在 *Chem. Commun.*, *Anal. Chem.* 等国内外学术期刊上发表 SCI 论文 20 多篇,近年来主持和完成国家自然科学基金 1 项,江苏省自然科学基金 1 项,徐州市重点研发计划 1 项,横向项目 1 项。

刘晓君教授,理学博士,硕士生导师,主要从事单颗粒的成像技术开发,以及单分子、单颗粒水平的蛋白质成像检测研究,在 *Analytical chemistry* 和 *ACS Sensors* 等学术期刊上发表 SCI 论文 20 多篇。近年来主持和完成国家自然科学基金 2 项。

宗成华副教授,理学博士,硕士生导师,围绕金、银纳米粒子的局域表面等离子体共振特性进行暗场光散射分析的应用,表面增强拉曼光谱分析的应用,探测 DNA 和小分子、离子的相互作用,在 *Anal. Chem*, *J. Mater. Chem*, *LANGMUIR* 等杂志上以第一作者或通讯作者身份发表文章十余篇,单篇论文引用次数最高 183 次。同时,主持国家自然科学基金青年项目 1 项,江苏省自然科学基金青年项目 1 项,徐州市社会发展项目 1 项,“十三五”第二批本科教育教学课程建设项目 1 项。荣获吉林省科学技术奖一等奖 1 项(第 8 完成人),江苏师范大学第九届青年教师教学优胜奖二等奖。

## 2.工作保障条件(如科研设施、实践场地等情况)

- 1) 公司拥有 2000 平米的 NGS 实验平台,按照国家临检中心高标准装修建设完成。
- 2) 公司拥有 NGS 平台建设的全套设备设施,主要包括打断仪、提取建库一体机、测序仪、western blot 琼脂糖凝胶电泳等等仪器设备、完全满足临床科研与实验的要求。
- 3) 公司拥有临床检测检验的全套资质、包括 QPCR 平台项目、临床检验项目、临床病理科等,已经通过美国 cap 认证,拥有全套高标准的质量管理体系。

3.生活保障条件（包括为进站研究生提供生活、交通、通讯等补助及食宿条件等情况）

1）公司每月可以为研究生同学提供 1500-2000 元生活补贴，满足生活所必要。

2）同时公司有职工的高等宿舍，单人单间，可以满足研究生同学的住宿要求。

3）公司园区有食堂、价格合理、菜品丰富，可以满足吃饭要求。

4）同时公司定期邀请国内外专家进行培训，满足学生求知需求

5）公司定期举行团建，开阔学生视野，加强社会经验的实习过程。

4.研究生进站培养计划和方案（具体培养方案需明确建设期内拟进站培养半年以上研究生人数，培养方式，工作站职责情况等，限 1000 字以内）

### 培养目标

（1）学以致用，将研究生掌握的理论知识和实验室技术与公司的分析仪器研发和检测业务需求结合，培养研究生的分析、解决问题能力，提升实践技能；

（2）合作精神和团队意识，二代测序技术、病理成像等团队实践活动开阔研究生的学术视野，培养合作精神和团队意识；

（3）专业自信，分析化学和临床检验是面向人民生命健康的重要支撑，通过市场调研和临床检验项目学习使研究生认识到专业重要性，增进专业归属感，培养专业自信心。

### 培养方式

#### （1）双导师负责制

进站研究生采取双导师负责制。设站单位为进站研究生配备在站导师，对研究生在站期间的培养进行全过程、全方位针对性指导。培养过程采取培训学习、生产实践和总结汇报相结合，导师指导和设站单位集体培养相结合的方式，加强实践创新能力培养。合作学校的导师定期了解研究生的学习和生活情况，掌握研究生的思想动态和需求，协助解决研究生的合理诉求，协助在站导师提高培养质量。

#### （2）培训学习与实践学习并重



研究生在系统掌握本学科基础理论和专业知识的基础上，通过完成进站学习培养实践创新能力。研究生在站期间需接受超洁净空间实验培训、生物安全培训、临床样本前处理培训等专业培训，考核合格才能参与相应的实践学习。实践学习包括二代测序技术实验全流程学习、IVD 试剂盒研发生产学习、临床检测项目学习、以及病理科检测项目学习。实践学习采取分类别专人管理模式，确保研究生接受到专业、正规的实践教育，了解新技术和新方法在临床检验的应用，将理论学习、实验研究和临床检验结合，培养解决实际问题的能力。

#### （3）汇报与考核相结合

专业培训采用考核制度，考核合格方可进行后续实践操作，确保培训效果，避免出现生产事故。核酸分析和临床检测等实践项目采用汇报制度。单个实践项目结束，研究生针对该实践项目进行汇报。所有实践项目完成，召开总结汇报会，在站研究生对在站期间的实践学习进行总结汇报，由导师和管理团队进行考核、评分。

### 工作站职责

建设期内拟进站培养半年以上研究生人数 **8-12** 人。设站单位负责进站研究生的全流程培养，配备专业技术或管理专家负责研究生的管理和指导工作，提供实验平台、工作场地、仪器设备、试剂耗材等工作条件，提供住宿、饮食、交通补贴等生活保障条件。设站单位合理分配在站研究生的实践活动、团队项目和学习生活，承担研究生培养质量的主体责任，既培养实践创新能力和团队协作能力，又培养正确的劳动观念、健康的体魄和良好的心理素质。

<div>申请设站单位意见 (盖章)</div> <div></div> <div>负责人签字 (签章)</div> <div></div> <div>年    月    日</div>	<div>高校所属院系意见 (盖章)</div> <div>负责人签字 (签章)</div> <div>年    月    日</div>	<div>高校意见 (盖章)</div> <div>负责人签字 (签章)</div> <div>年    月    日</div>
---	---	---

# 证明材料目录

## 1、企业资质

1.1 高新技术企业证书.....	1
1.2 专精特新小巨人企业证书.....	2
1.3 长三角联合创新中心证书.....	3

## 2、科技创新平台

2.1 徐州市市级工程研究中心立项批文.....	4
2.2 徐州市市级企业工程技术研究中心立项批文.....	7
2.3 徐州市产业研究院备案批文.....	10

## 3、合作基础

3.1 联合承担的项目：2023 年在徐高校服务“343”产业发展项目..	13
3.2 合作研究的成果：专著、获奖、论文.....	18

## 4、工作站条件保障

4.1 外聘专家聘书.....	55
4.2 知识产权情况.....	56
4.3 实验环境及仪器展示.....	83

## 5、共建协议

5.1 江苏省研究生工作站共建协议.....	86
------------------------	----

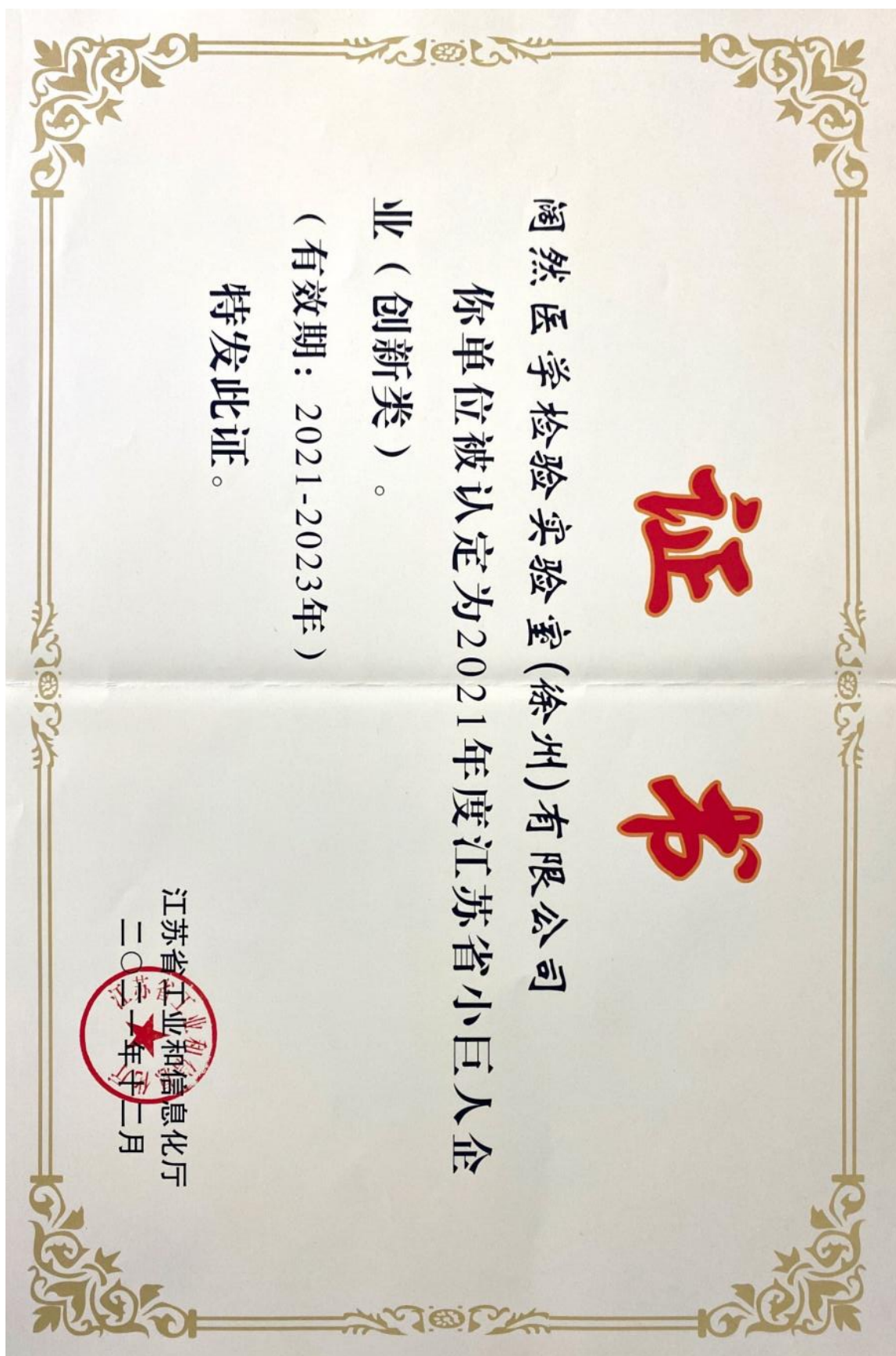
## 1、企业资质

### 1.1 高新技术企业证书





## 1.2 专精特新小巨人企业证书





### 1.3 长三角联合创新中心证书



## 2、科技创新平台

### 2.1 徐州市市级工程研究中心立项批文

# 徐州市发展和改革委员会文件



徐发改高技〔2023〕334号

## 关于同意建设 2023 年市级工程研究中心的通知

各县（市、区）经济发展局，徐州经济技术开发区发展改革局，徐州高新技术产业开发区经济发展局，徐州淮海国际港务区经济发展部：

根据《徐州市工程中心（工程实验室）管理办法（试行）》（徐发改高技发〔2017〕52号）及有关规定，我委会同有关专家对各地申请建设的 2023 年市级工程研究中心项目，就所属领域、研发方向、新增投资额、研发人员数量、研发场地面积等相关建设条件进行了审核，原则同意建设徐州市碳化硅衬底生长和加工工程研究中心等 36 家市级工程研究中心。

请各地督促依托单位尽快开展创新平台建设工作，加强对创新平台建设过程的服务和监管。在建设过程中，对于研发方

— 1 —

向发生重大变化的，需及时调整项目建设内容，报我委重新审批；对于组织建设不力或确实不再实施建设的，及时报我委撤销建设计划。

附件：徐州市 2023 年市级工程研究中心汇总表

徐州市发展和改革委员会  
2023 年 12 月 29 日



（此件依申请公开）

---

徐州市发展和改革委员会

2023 年 12 月 29 日印发

---

序号	名称	依托单位	建设内容	建设地点	主持部门
34	徐州市间充质干细胞治疗工程研究中心	徐州医科大学附属医院	围绕生物技术和新医药产业发展中的干细胞/干细胞外泌体临床治疗等问题，建设细胞治疗实验平台、组织修复与再生医学实验室、区域细胞中心公司研发场地等创新平台，开展干细胞GMP产业化生产和质量控制标准等方面研究，突破干细胞标准化药物转化等关键技术。建设总投资2000万元，建设期：2024年-2028年。	泉山区	泉山区经济发展局
35	徐州市生理健康监测和智能诊疗研究中心	江苏师范大学	围绕生物技术和新医药产业发展中的生理健康监测、疾病早期诊断和药物靶向递送等问题，建设基于光电感知生物电子器件的生理信号动态监测和基于柔性高分子的药物靶向递送及可控释放等创新平台，开展生理健康监测、疾病早期诊断和药物靶向递送等方面研究，突破生理健康监测准确性不足、疾病早期诊断指标难以捕捉、药物递送效率低等关键技术。建设总投资1500万元，建设期：2023年-2025年。	泉山区	泉山区经济发展局
36	徐州市基于血清miRNA肝癌早期辅助诊断试剂研发工程研究中心	阔然医学检验实验室（徐州）有限公司	围绕生物技术和新医药产业发展中的肝癌早期诊断等问题，开展肝癌早期诊断方面研究，突破血清miRNA组合在肝癌早期诊断中的预测效果等关键技术。建设总投资500万元，建设期：2022年-2024年。	徐州市港务区	徐州市港务区经济发展部



## 2.2 徐州市市级企业工程技术研究中心立项批文

# 徐州市科学技术局

---

## 关于对2021年度拟新建市级企业工程技术研究中心的公示

根据《关于下放市级工程技术研究中心管理权限的通知》（徐科发〔2018〕71号）、《关于做好2021年市级企业工程技术研究中心建设工作的通知》（徐科发〔2021〕30号）要求及2021年全市企业研发机构建设工作的统筹安排，徐州市科技局组织开展了2021年度市级企业工程技术研究中心新建工作。经各单位提交材料，各县（市）区科技局评审、推荐，市科技局审核等流程，现将2021年拟新建市级企业工程技术研究中心项目予以公示。公示时间自2021年9月15日起至9月21日止，为期7天。

公示期间，任何单位和个人对公示内容有异议的，请以书面形式提出，并提供必要的证明材料。为便于核实查证，确保客观公正处理异议，提出异议的单位或者个人应当表明真实身份，并提供有效联系方式。以单位名义提出的，须在异议材料上加盖本单位公章。个人提出异议的，须签署真实姓名。超出公示期的异议不予受理。

业务处室：市科技局科研条件处      83842134

---

监督处室：市科技局机关纪委           83842107

联系地址：徐州市新城区元和路1号行政中心东区综合楼B  
区6楼 徐州市科学技术局

邮政编码：221018

附件：2021年度拟新建市级企业工程技术研究中心清单

徐州市科学技术局

2021年9月15日

23	徐州市 (大光) 涂料工程技术研究中心	徐州大光涂料厂	贾汪区
24	徐州市 (华正) 玻璃钢管工程技术研究中心	徐州华正钢管有限公司	贾汪区
25	徐州市 (徐矿电厂) 循环流化床综合利用工程技术研究中心	江苏徐矿综合利用发电有限公司	贾汪区
26	徐州市 (聚城佳工) 装配式墙板体系一体化工程技术研究中心	徐州聚城住宅工业科技发展有限公司	贾汪区
27	徐州市 (山美环保) 废弃物资源化工程技术研究中心	徐州山美环保科技有限公司	贾汪区
28	徐州市 (七星机械) 纺织机工程技术研究中心	徐州七星机械有限公司	云龙区
29	徐州市 (美卓) 矿用永磁同步电动机变频调速控制系统工程技术研究中心	美卓矿山安全设备(徐州)有限公司	泉山区
30	徐州市 (迅普) 全自动实时荧光定量核酸检测仪工程技术研究中心	江苏迅普生物技术有限公司	经开区
31	徐州市 (集萃) 道路工程技术研究中心	江苏集萃道路工程技术与装备研究所有限公司	经开区
32	徐州市 (天科合达) 半导体碳化硅片智能检测分析工程技术研究中心	江苏天科合达半导体有限公司	经开区
33	徐州市 (爱砂) 半导体封装芯片智能检测分析工程技术研究中心	江苏爱砂半导体科技有限公司	经开区
34	徐州市 (徐工港机) 电动化流机工程技术研究中心	徐州徐工港口机械有限公司	经开区
35	徐州市 (庆亚) 智能化装备工程技术研究中心	江苏庆亚电子科技有限公司	高新区
36	徐州市 (福瑞士) 锂电池工程技术研究中心	江苏福瑞士电池科技有限公司	高新区
37	徐州市 (中矿汇弘) 矿山岩石破碎技术工程技术研究中心	徐州中矿汇弘矿山设备有限公司	高新区
38	徐州市 (博德纳) 自动化控制系统工程技术研究中心	江苏博德纳的系统工程股份有限公司	高新区
39	徐州市 (盛浩) 建筑施工装备工程技术研究中心	江苏盛浩工程科技有限公司	高新区
40	徐州市 (国然) 肝部标志物高灵敏、精准检测方法及其试剂盒工程技术研究中心	国然医学检验实验室(徐州)有限公司	港务区



## 2.3 徐州市产业研究院备案批文

徐州市科学技术局

kjj.xz.gov.cn

网站首页

政府信息公开

政务服务

政民互动

当前位置： 首页 > 政府信息公开 > 法定主动公开内容 > 通知公告

索引号:	01405133-5/2020-00032		
发布机构:	市科学技术局	成文日期:	2020-12-22
信息名称:	2020年第三批拟备案市级新型研发机构名单公示		
文号:			

### 2020年第三批拟备案市级新型研发机构名单公示

为贯彻落实市委、市政府《关于加快新型研发机构建设的实施意见》（徐委发〔2018〕58号）要求，加快建设高水平运行的新型研发机构，增强科技创新对产业发展的引领支撑作用，我局组织开展了2020年度第三批市级新型研发机构备案工作。现对通过形式审查和实地复核的25家新型研发机构进行备案公示，公示时间为2020年12月23日至12月29日。

如对公示中的新型研发机构有异议，请在公示时间内以书面方式反映。凡以单位名义反映情况的材料要加盖公章，以个人名义反映情况的材料要具实名并附联系方式。不受理匿名举报。

联系部门及电话：

市科技局科研条件处 0516-83842134

市科技局机关纪委 0516-83852568

地址：新城区元和路1号行政中心东综合楼B区6楼

附件：2020年第三批拟备案市级新型研发机构名单



徐州市科学技术局

2020年12月23日

附件下载: 1. 附件.docx

分享到:

打印

[网站地图](#) | [网站联系](#) | [网站数据报表](#) | [网站声明](#)

版权所有: 徐州市科学技术局

主办单位: 徐州市科学技术局

总访问量: 1509664

苏ICP备2021002917号-1

 苏公网安备 32039302000172号

网站识别码: 3203000037

序号	新型研发机构名称	运营机构名称
8	徐州智云安全技术研究院	徐州智云安全技术研究院有限公司
9	徐州夏尔智能焊接研究院	徐州夏尔智能焊接研究院有限公司
10	徐州远方药食同源健康产业研究院	徐州远方药食同源健康产业研究院有限公司
11	徐州金琳光电材料产业研究院	徐州金琳光电材料产业研究院有限公司
12	江苏金圣硅基新材料研究院	江苏金圣硅基新材料研究院有限公司
13	净视源研究院	江苏净视源研究院节能环保有限公司
14	徐州科然稀土新材料研究院	徐州科然稀土新材料研究院有限公司
15	徐州圣帕斯动力技术研究院	徐州圣帕斯动力技术研究院有限公司
16	阔然精准医学科技（徐州）研究院	阔然精准医学科技（徐州）研究院有限公司
17	徐州无废城市技术研究院	徐州无废城市技术研究院有限公司
18	诺航生物技术研究院	诺航生物技术研究院徐州有限公司

+

### 3、合作基础

#### 3.1 联合承担的项目：2023 年在徐高校服务“343”产业发展项目

## 徐州市财政局 文件 徐州市科学技术局

徐财教〔2023〕64 号

### 关于下达 2023 年在徐高校服务“343” 产业发展项目资金的通知

徐州工程学院、各有关单位：

根据《市政府关于印发在徐高校服务地方发展专项支持资金管理办法的通知》（徐政规〔2019〕2 号）、《关于印发〈在徐高校服务“343”产业发展项目实施方案（试行）〉的通知》（徐科发〔2023〕33 号），现将 2023 年在徐高校服务“343”产业发展项目支持资金下达给你们（详见附件），相应增列 2023 年度“其他技术与开发支出”（政府收支分类科目编码：2060499）预算支出指标。非市级部门预算单位的资金下达到市科技局，由市科技局按照国库集中支付的要求拨付至相关项目单位。

请依照资金管理办法要求，切实履行项目主管部门职责，加强项目组织协调和实施管理，认真落实企业自筹研发经费及时拨付

— 1 —

徐州市财政局文件

---

到位，确保资金科学使用、专款专用、专账管理，抓紧推进项目实施,早出成果和效益。

附件：1.2023 年在徐高校服务“343”产业发展项目资金分配表  
2.2023 年在徐高校服务“343”产业发展项目明细表

徐州市财政局

徐州市科学技术局

2023 年 12 月 28 日

---

徐州市财政局办公室

2023 年 12 月 28 日印发

---

-2-

徐州市财政局文件

项目编号	项目名称	项目负责人	需求企业	承担单位	财政支持 研发经费	2023年度 市级拨款	起止 时间
gx2023010	自然资源高分遥感影像解译及其耕地“双非”监测技术	张连蓬	徐州市物联网研究院有限公司	江苏师范大学	100	70	2023.09-2025.08
gx2023011	面向自主照料料的智能护理床研发	杨增汪	徐州市永康电子科技有限公司	江苏师范大学	100	70	2023.09-2025.08
gx2023012	甘薯膳食纤维产品关键技术研究	田俊	江苏派乐滋食品有限公司	江苏师范大学	100	70	2023.09-2025.08
gx2023013	数字免疫分析技术	盖宏伟	固然医学检验实验室（徐州）有限公司	江苏师范大学	200	140	2023.09-2025.08
gx2023014	新一代半导体复合衬底材料研究与制备技术	李延彬	江苏科达平昌体育科技有限公司	江苏师范大学	200	140	2023.09-2025.08
gx2023015	超大规模集成电路用超细球形硅微粉研究	周天元	江苏中腾石英材料科技有限公司	江苏师范大学	200	140	2023.09-2025.08
gx2023016	面向智能芯片、5G通讯的高端镀膜靶材的研发	张洪浩	徐州盛唐光电科技有限公司	江苏师范大学	100	70	2023.09-2025.08
gx2023017	新型生物农药杀菌防腐剂技术研发及产业化	杨绪勤	江苏诺恩作物科学股份有限公司	江苏师范大学	100	70	2023.09-2025.08
gx2023018	合成生物蓝菌的微生物细胞构建及应用技术	蒋继宏	徐州合谷生命科技有限公司	江苏师范大学	200	140	2023.09-2025.08
gx2023019	太阳能光伏硅片的高品质低碳技术的研究	徐晓东	江苏协鑫硅材料科技发展有限公司	江苏师范大学	200	140	2023.09-2025.08
gx2023020	矿山矮机身大功率智能化掘锚一体关键技术研发	张农	徐州徐工工程机械有限公司	徐州工程学院	300	210	2023.09-2025.08
gx2023021	小分子、高纤维、全营养植物基食品加工关键技术研究与应	李苏北	维维食品饮料股份有限公司	徐州工程学院	200	140	2023.09-2025.08



# 在徐高校服务“343”产业发展 项目合同

项目 编 号 gx2023013  
项目 名 称 数字免疫分析技术  
项目 负 责 人 盖宏伟  
需 求 企 业 阔然医学检验实验室（徐州）有限公司  
项目 主 管 部门 江苏师范大学  
起 止 年 限 2023 年 9 月至 2025 年 8 月

徐州市科学技术局

二〇二三年

## 十、签订合同各方

甲方:

法定代表人或委托代理人 (签字)



处室负责人 (签字)

经办人 (签字)



*[Handwritten signature]*



乙方:

项目负责人 (签字)

*[Handwritten signature]*

账户名称

开户银行

账 号

法定代表人 (签字)

*[Handwritten signature]*

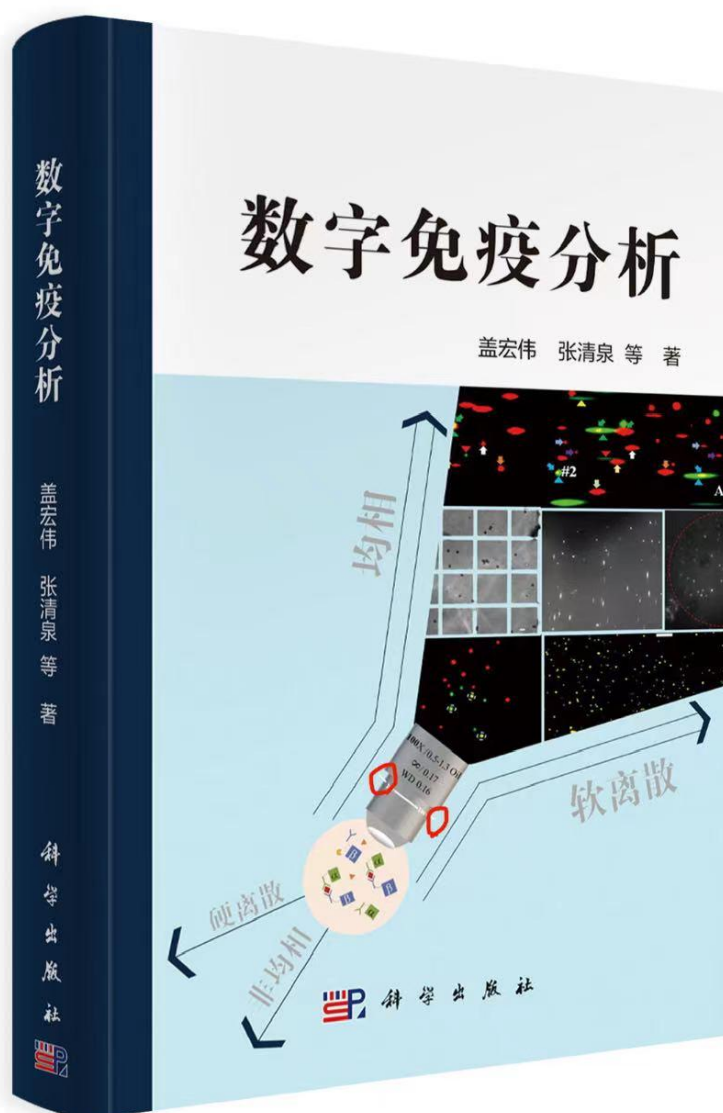


丙方:

法定代表人 (签字)



### 3.2 合作研究的成果





---

图书在版编目 ( CIP ) 数据

数字免疫分析/盖宏伟等著. —北京: 科学出版社, 2023.8

ISBN 978-7-03-076032-6

I. ①数… II. ①盖… III. ①免疫学-生物分析 IV. ①Q939.91

中国国家版本馆 CIP 数据核字 ( 2023 ) 第 134827 号

---

责任编辑: 杨 震 刘 冉 / 责任校对: 杨 赛

责任印制: 吴兆东 / 封面设计: 盖悦涵

科学出版社 出版

北京东黄城根北街 16 号

邮政编码: 100717

<http://www.sciencep.com>

印刷

科学出版社发行 各地新华书店经销

\*

2023 年 8 月第 一 版 开本: 720 × 1000 B5

2023 年 8 月第一次印刷 印张: 16 1/4

字数: 330 000

定价: 150.00 元

( 如有印装质量问题, 我社负责调换 )



# 江苏省分析测试协会科学技术奖

获奖者：盖宏伟

奖励等级：特等

奖励项目：数字免疫分析

奖励年度：二〇二二年

证书号：2022-FXCSJ-T2-R01

江苏省分析测试协会  
二〇二二年十二月





# Amplification-Free Digital Immunoassay down to the Attomolar Level by Synergistic Sedimentation of Brownian Motion Suppression and Dehydration Transfer

Qingquan Zhang,<sup>§</sup> Wenwen Chai,<sup>§</sup> Xiaoyan Pan, and Hongwei Gai\*

Cite This: *Anal. Chem.* 2024, 96, 3054–3061

Read Online

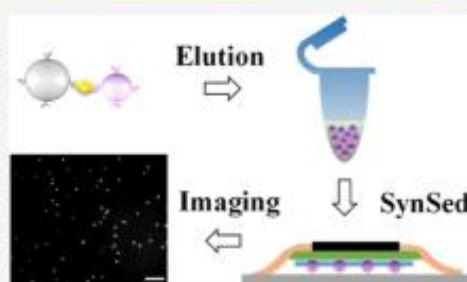
ACCESS |

Metrics & More

Article Recommendations

Supporting Information

**ABSTRACT:** Amplification-free digital immunoassays (DIAs) typically utilize optical nanoparticles to enhance single immunocomplex molecule detection. The efficiency and uniformity of transferring the nanoparticles from a bulk solution to a solid surface determine the limit of detection (LOD) and the accuracy of DIAs. Previous methods suffer from issues like low efficiency, nonuniform distribution, and particle aggregation. Here, we present a novel technique named synergistic sedimentation of Brownian motion suppression and dehydration transfer (SynSed) for nanoparticles using water-soluble polymers. The efficiency of transferring quantum dots (QDs) was increased from 10.7 to 91.4%, and the variation in QD distribution was restricted to 8.8%. By incorporating SynSed into DIAs, we achieved a remarkable reduction in the LOD (down to 3.9 aM) for carcinoembryonic antigen and expanded the dynamic range to cover 3 orders of magnitude in concentration, ranging from 0.01 to 10 fM. DIAs enhanced with SynSed possess ultrahigh sensitivity, advanced accuracy, and specificity, offering a great premise in early disease diagnostics, risk stratification, and treatment response monitoring.



## 1. INTRODUCTION

Proteins whose dysregulation is related to serious disease always serve as drug targets or biomarkers. Detection and quantification of protein biomarkers in clinical samples are beneficial for disease progression monitoring and early diagnosis.<sup>1</sup> The concentrations of a portion of biomarkers may be down to subpicomolar or even subfemtomolar in the early stages of disease.<sup>2</sup> For example, the p24 capsid antigen in the serum of early HIV-infected individuals is in the range of 50 aM to 15 fM.<sup>3</sup> P-Tau181 in the serum of neurodegenerative disorders is 1.81 pg/mL,<sup>4</sup> and ORF 1p in carcinomas and high-risk precursors during carcinogenesis is 10<sup>−17</sup> M.<sup>5</sup> Conventional techniques, including ELISA,<sup>6</sup> Western blot,<sup>7</sup> and mass spectrometry,<sup>8</sup> are not able to quantify these rare biomarkers. A digital immunoassay (DIA) is a type of immunoassay known for its ultrahigh sensitivity and specificity.<sup>9</sup> In DIAs, proteins are quantified by counting individual signals correlated with the target protein rather than detecting the signal intensity generated by groups of target proteins. DIAs can be categorized into two types: signal amplification detection and direct amplification-free detection. For signal amplification, a single target protein has to be conjugated to an enzyme or a DNA fragment after the immunoreaction.<sup>10</sup> The enzyme catalyzes substrates in microspaces to generate fluorescent compounds<sup>10,c,e</sup> or deposits fluorescent substances around the immunocomplex using tyramide signal amplification.<sup>10,d</sup> The

number of microspaces or immunocomplexes with activated fluorescence is used to quantify the target protein. Additionally, DNA can be extended into concatemers via rolling circle amplification (RCA) and hybridized with fluorescently labeled probes to achieve signal amplification.<sup>10b</sup> A typical single-enzyme reaction takes approximately 20 min,<sup>10a</sup> while RCA requires over 1 h.<sup>10b,11</sup> These amplification techniques require more reaction time and a larger amount of reagents, increasing the risk of generating false-positive signals.<sup>12</sup>

Amplification-free DIAs are straightforward and can reduce the aforementioned risks, but the direct detection of a weak signal from a single dye molecule is not an easy way. Micro-/nanoparticles with strong optical signals, such as noble metal nanoparticles,<sup>13</sup> quantum dots (QDs),<sup>14</sup> or upconversion nanoparticles,<sup>15</sup> are used to label immunocomplexes. Target proteins are usually quantified through massive imaging and counting of individual particles or particle aggregates in amplification-free DIAs. Optical observation of single nanoparticles is ready to be realized whether in a solution or on a

Received: November 9, 2023

Revised: January 16, 2024

Accepted: January 23, 2024

Published: February 8, 2024





solid surface<sup>16</sup> using techniques like fluorescence,<sup>17</sup> surface-enhanced Raman spectroscopy,<sup>18</sup> or dark-field microscopy.<sup>19</sup> However, it is still a great challenge to simultaneously image massive particles with Brownian motion in solution. Therefore, nanotags must be transferred from the reacting medium to the solid substrate before imaging. The efficiency and uniformity of this particle transfer directly and significantly affect the sensitivity and accuracy of DIAs. To enhance the particle transferring efficiency, a combination of electrostatic attraction and liquid layer compression is employed.<sup>14b,20</sup> Substrates are modified with opposite charges to particles through ionic polymer assembly or the silylation reaction. The migration of nanoparticles toward the substrate is accelerated by electrostatic attraction. Meanwhile, coverslips are pressed above the substrates to control the liquid thickness and shorten the diffusion distance. Even so, the sedimentation efficiency of nanoparticles is still low, leading to LODs at the fM level,<sup>14b</sup> far from LODs achieved with amplification methods.<sup>10b</sup> Comparisons of typical DIAs are listed in Table S1. Generally, the LODs of amplification DIAs are lower by 2–3 orders of magnitude than those of the amplification-free methods labeled with nanotags. This is because those immunocomplex molecules labeled with nanotags cannot be completely sedimented and counted. When the dehydration-driven transfer was adopted to sediment microspheres labeled immunocomplex molecules, a sedimentation efficiency of 100% and lowering the LOD to the aM level were achieved.<sup>21</sup> However, dehydration-driven transfer is effective only for microspheres. When applied to nanoparticles, it induces aggregation and nonuniform distribution, which is fatal for resolving single nanoparticles and accurately counting them. To date, the highly efficient and uniform transfer of nanoscale particles to solid surfaces is still a great challenge and urgently needs to be solved for lowering the LOD and improving the accuracy of amplification-free DIAs.

Here, we present a highly efficient and uniform nanoparticle sedimentation method named synergistic sedimentation of Brownian motion suppression and dehydration transfer (SynSed). Using SynSed, the QD sedimentation efficiency exceeds 90%, and the uniformity is comparable to that of electrostatic attraction. This highly efficient, uniform, and low-cost particle transfer method enables a remarkable decrease in the LOD of amplification-free DIAs down to several aM levels, which is the lowest LOD of DIA to date, showing great potential in disease progression monitoring and early diagnostics.

## 2. EXPERIMENTAL SECTION

**2.1. Materials and Instruments.** The Sylgard 184 polydimethylsiloxane (PDMS) oligomer and curing agent were from Dow Corning (Midland, MI). mPEG-silane (5 kDa) was from the Deltabio Company (China). Dextran (DEX, 40, 100, and 500 kDa), polyethylene glycol (PEG, 6, 8, and 20 kDa), 2-(*N*-morpholino)ethanesulfonic acid (MES), dimethyl sulfoxide (DMSO), and tween 20 were from the J&K Scientific Company (China). Oxygen Maximum Recovery Pipet Tips (10 and 200  $\mu$ L) were purchased from Corning. Protein LoBinding Tubes (0.5 and 1.5 mL) were provided by Eppendorf Corporation. 1-Ethyl-3-(3-(dimethylamino)propyl)-carbodiimide (EDC) and poly(diallyldimethylammonium chloride) solution (average Mw 40,000–50,000) were from Sigma-Aldrich (USA). Monoclonal capture antibody, monoclonal detection antibody, and human carcinoembryonic

antigen (CEA) were purchased from Shanghai Linc-Bio Science Co., Ltd. (China). Carboxyl magnetic beads (Dynabeads M-270), SuperBlock (PBS) buffer, carboxyl QDs (Qdot655ITKTM), and coverslips were purchased from Thermo Fisher Scientific (USA). Carboxyl polystyrene (PS) spheres (0.198  $\mu$ m diameter) were provided by Bangs Laboratories (USA). Glass slides were obtained from Jiangsu ShiTai Experimental Equipment Co., Ltd. (China).  $\text{NaH}_2\text{CO}_3$ ,  $\text{Na}_2\text{HCO}_3$ , NaCl, NaOH, and  $\text{NaHCO}_3$  were purchased from Sinopharm Chemical Reagent Co., Ltd. (China). Ultrafilters with a 30 kDa molecular weight cutoff were from Millipore (USA).

An inverted fluorescence microscope (IX71) equipped with an electron-multiplying charge-coupled device (EMCCD) and 100 $\times$ /1.40 objective lens (UplanSApo) was purchased from the Olympus company (Japan). HPLC (1200 Series) was obtained from Agilent Technologies (USA). A magnetic separator (DynaMagTM-2), a low-temperature, high-speed centrifuge (Sorvall Legend Micro 17R), and a fixed-speed vortex mixer (Hulamixer) were obtained from Thermo Fisher Scientific (USA). A fluorescence spectrophotometer (FL-8500) was purchased from PerkinElmer (USA). Atomic force microscopy (Dimension Icon) was from Bruker (USA).

### 2.2. QD and Fluorescent PS Nanosphere Sedimentation.

**2.2.1. PDMS Microwell Surface Treatment.** PDMS pieces were perforated through holes and adhered reversibly to a coverslip to create PDMS microwells. The diameter of the microwells was adjusted within the range of 2.5–4 mm. A 10% (w/v) mPEG-silane solution was prepared by mixing 10 mg of mPEG-silane with 100  $\mu$ L of DMSO. Subsequently, the PDMS microwells were filled with the 10% (w/v) mPEG-silane solution and incubated at room temperature for 15–25 min. Then, the residual solution was removed by a vacuum pump.

**2.2.2. SynSed.** A 0.1% (w/v) DEX solution was prepared by dissolving 3.6 mg of DEX in 3.6 mL of deionized (DI) water. To create a 1 pM QD solution for sedimentation, 1  $\mu$ L of 1.0 nM QD solution was mixed with 999  $\mu$ L of the 0.1% (w/v) DEX solution. 1  $\mu$ L of the QDs and DEX mixture was added to the pretreated PDMS microwell. After 20 min of evaporation at room temperature, DEX precipitated and formed a single-layer membrane at the bottom of the microwell. The QDs were forcibly transferred and immobilized on the substrate surface. Subsequently, the PDMS piece was peeled off. The coverslip with QDs was then sealed onto a glass slide by using transparent tape. For SynSed of PS nanospheres, 1.0  $\mu$ L of 0.0002 mg/mL PS nanospheres suspended in 0.1% (w/v) DEX solution was used.

**2.2.3. Electrostatic Attraction Sedimentation.** Glass slides were soaked in a chromic acid solution for 12 h and rinsed with DI water three times. To prepare a 1.0% (v/v) cationic polymer solution, 1.0 mL of poly dimethyl diallyl ammonium chloride was mixed with 100 mL of DI water and subjected to 30 min of ultrasonic processing. Afterward, the cleaned glass slides were submerged in the 1.0% (v/v) cationic polymer solution, subjected to 30 min of ultrasonication, and left to incubate for 12 h. Subsequently, the glass slides were removed and dried in an oven at 80  $^{\circ}\text{C}$ . This process resulted in the formation of a positively charged layer on the surface of the glass slides. 2  $\mu$ L of a 50 pM QD solution was pipetted onto a glass slide with a positive charge. A cleaned coverslip was carefully placed over the liquid layer, and tweezers were used to gently compress it. The edges of the coverslip were sealed with nail polish. Due to electrostatic attraction, the QDs



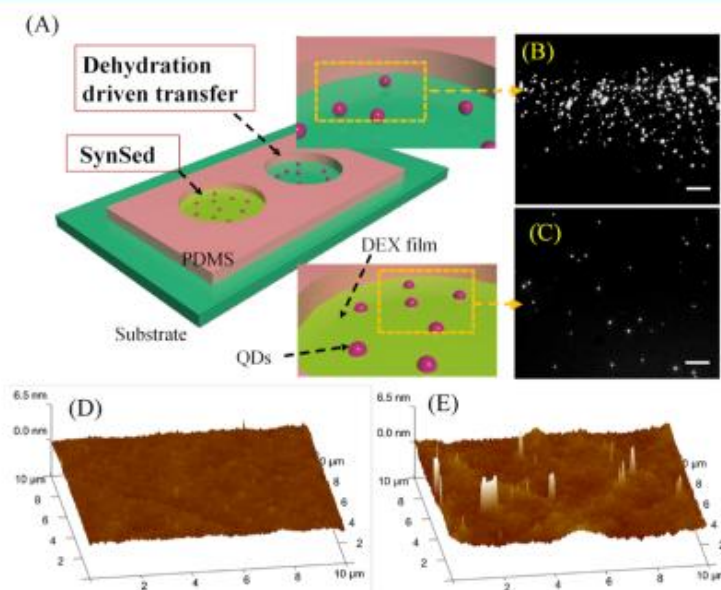


**Figure 1.** (A) Schematic of QD sedimentation via SynSed and dehydration-driven transfer. (B,C) Fluorescence images of QDs at the edge of the microwell shown in (A). (D,E) Atomic force microscopy images of pure DEX membrane (D) and QDs in the DEX film (E). Scale bars: 8  $\mu\text{m}$ .

gradually settled on the glass slide over a 20 min period. Subsequently, the sedimented QDs were imaged by using an inverted microscope (IX71) equipped with a 100 $\times$  objective and an EMCCD. The images were processed using ImageJ, and the number of QDs was determined through manual counting. For the sedimentation of PS nanospheres, we replaced the QD solution with 3  $\mu\text{L}$  of a 0.0002 mg/mL PS nanosphere solution. The remaining procedures were identical to those used for the QD sedimentation.

**2.3. DIAs of CEA.** **2.3.1. Capture Beads' Preparation.** A 25  $\mu\text{L}$  portion of magnetic bead suspension ( $2 \times 10^9$  beads/mL) was mixed with 25  $\mu\text{L}$  of 0.01 M NaOH in a low-adsorption tube. After magnetic separation and removal of the supernatant, the remaining magnetic beads were then incubated with 25  $\mu\text{L}$  of 0.01 M NaOH for 10 min. Subsequently, the beads were washed three times with 25  $\mu\text{L}$  of DI water. Next, we added 50  $\mu\text{L}$  of a freshly prepared EDC solution with a concentration of 25 mg/mL in the tube and incubated it for 30 min. After this incubation, we repeated the washing step twice: once with cold water and once with 50 mM MES buffer at pH 5.0.

Following this, we added 20  $\mu\text{L}$  of capture antibodies for CEA with a concentration of 1.7 mg/mL and 30  $\mu\text{L}$  of MES buffer at pH 5.0 to the tube, incubating it for 1 h to form capture beads. Any unbound capture antibodies were removed through magnetic separation. The capture beads were then washed four times with PBS containing 0.05% (v/v) Tween 20 (PBST). Finally, the capture beads were resuspended in 250  $\mu\text{L}$  of PBST and were ready for use. The effective modification of capture antibodies on magnetic beads was evidenced by the

variation in the zeta potential at the bead surface. The zeta potential of unmodified magnetic beads was  $-69.35$  mV. After the capture antibody modification, the zeta potential of the capture beads decreased to  $-23.44$  mV (Figure S7A).

**2.3.2. Detection QDs Preparation.** 3.0  $\mu\text{L}$  of 8.0  $\mu\text{M}$  QD solution was mixed with 6.0  $\mu\text{L}$  of 1 mg/mL EDC solution and 21  $\mu\text{L}$  of cold  $\text{NaHCO}_3$  solution with a pH of 9.0. The 1 mg/mL EDC solution was freshly prepared using cold 50 mM  $\text{NaHCO}_3$  at pH 9.0 and the appropriate amount of EDC. This mixture was incubated at room temperature for 25 min. 8.0  $\mu\text{L}$  of 4 mg/mL detection antibody solution for CEA was mixed with 13.5  $\mu\text{L}$  of the EDC-activated QD suspension and incubated for 5 h, resulting in the formation of detection QDs. This mixture was then centrifuged for 5 min at 14,000g. The supernatant, which contained detection QDs and unbound detection antibodies, was separated using an HPLC system equipped with a homemade column. This process allowed us to purify and collect the detection QDs in a low-adsorption tube (Figure S7B).

**2.3.3. Immunoassay.** We mixed the detection-QD solution with SuperBlock buffer in a volume ratio of 30:1 and incubated it in the dark for 30 min. At the same time, we prepared a 10% (v/v) superblocking solution by mixing 0.4 mL of SuperBlock solution, 3.6 mL of PBS, and 2  $\mu\text{L}$  of Tween 20. We then suspended 800,000 capture beads in 100  $\mu\text{L}$  of the 10% (v/v) superblocking solution and incubated them for 30 min. This step effectively blocked nonspecific adsorption sites on both the capture beads and the detection QDs. After magnetic separation and removal of the supernatant, we combined the blocked capture beads with the blocked detection-QD solution



and CEA in precise quantities. We added PBS to make the final volume 150  $\mu\text{L}$  and maintained the concentration of detection QDs at 100 pM. The mixture was then incubated for 2 h. Following incubation, magnetic separation was used to remove the supernatant. The remaining materials were washed three times with 200  $\mu\text{L}$  of PBST, effectively removing any unbound CEA and detection QDs.

To elute the detection QDs within the immunocomplexes, we added 10  $\mu\text{L}$  of an alkaline solution (pH = 10.9) containing 1.0% (w/v) DEX. Because pH simultaneously affects density and distribution of surface charge, the degree of collapse of protein structure, and the interaction of protein molecules,<sup>22</sup> the elution function is primarily governed by the pH of the solution, with DEX serving as an additive for the subsequent SynSed process of the eluted detection QDs. After another round of magnetic separation, the supernatant containing the eluted detection QDs was collected in a low-adsorption tube. Subsequently, we transferred and immobilized the collected detection QDs onto a coverslip by using SynSed for imaging and counting.

**2.4. Measurement of CEA in Serum.** 300  $\mu\text{L}$  of serum was pipetted into an ultrafilter with a molecular cutoff of 30 kDa to remove CEA from the serum. The resulting CEA-free serum was then diluted by 4, 10, 6000, and 60000 folds, respectively. These CEA-free serums underwent the same DIA procedures as those mentioned earlier to evaluate the matrix effect.

For serum no. 1, it was diluted with PBS (pH 7.4) to the appropriate degree and dispensed into five low-adsorption tubes in precise quantities. In these tubes, we added 0, 1.2, 2.4, 3.6, and 4.8  $\mu\text{L}$  of a 5 fM CEA solution. After the addition of the blocked capture beads and detection QDs for CEA, PBS was added to each tube to ensure a final reaction volume of 150  $\mu\text{L}$ . The finally achieved dilution factor of serum no. 1 was 60,000. These CEA-spiked serum samples were subsequently analyzed by following the DIA procedures. The measured numbers of detection QDs were plotted against the concentrations of spiked CEA, resulting in a standard addition curve. We used the equation of this curve to calculate the CEA concentration in the diluted serum sample. To determine the CEA concentration in the initial serum no. 1, we restored it by multiplying the measured value with the dilution factor. Serum no. 2 was diluted using the same method, with a final dilution factor of 6000-fold and spiked CEA concentrations of 0, 1.0, 2.0, 3.0, and 4.0 fM. The subsequent steps for serum no. 2 were identical to those for serum no. 1.

### 3. RESULTS AND DISCUSSION

**3.1. SynSed of Nanoscale Particles.** SynSed processes are shown in Figure S1A. The mixed solution of QDs and DEX is pipetted into a PDMS microwell that was pretreated with mPEG-silane. As the aqueous solution gradually evaporates at room temperature (25  $^{\circ}\text{C}$ ), the DEX is concentrated, and the viscosity of the mixture increases. High-viscosity solution suppresses the Brownian motion of QDs and effectively prevents QD aggregation. Simultaneously, the thinning of the liquid layer in the microwell forces the QDs to move toward the coverslip. After 20 min, when the dehydration process is completed, the DEX precipitates and forms a film, embedding all QDs within it. Carefully, the PDMS piece is removed from the coverslip, and the coverslip is sealed with a glass slide using transparent tape, allowing for imaging under fluorescence microscopy. Figure 1A schematically illustrates the difference

between QD sedimentation using SynSed and dehydration-driven transfer. In dehydration-driven transfer, QDs are transferred onto the substrate, but the distribution of QDs is nonuniform. QDs tend to accumulate at the edges of the microwell, while conversely, in the central region of the microwell, the bright spots of QDs are nearly absent. Furthermore, particle aggregation is substantial, and a single QD within the aggregates cannot be resolved by the microscope (Figure 1B). In SynSed, QDs are uniformly distributed across the entire substrate, extending from the edge to the center, and they remain as single particles without significant aggregation, as shown in Figure 1C. The atomic force microscopy images reveal that the precipitated DEX film without QDs is uniform and flat (Figure 1D), and the roughness average value is down to 0.549 nm when measured over a sampling line of 10  $\mu\text{m}$ . The transferred QDs are partially embedded in the DEX film (Figure 1E). We measured the viscosity of the polymer solution shown in Figure S2 and calculated the corresponding diffusion coefficient following the Stokes–Einstein equation

$$D = \frac{kT}{6\pi\eta r}$$

where  $D$  is the diffusion coefficient,  $k$  is Boltzmann's constant,  $\eta$  is the solution viscosity,  $r$  is the particle radius, and  $T$  is the absolute temperature.

When the DEX concentration is increased from 0.01 to 50% (w/v), the viscosity of solution is increased from 0.005 to 1.57 Pa s (Figure S2), and the diffusion coefficient of QDs is reduced from  $441.6 \times 10^{-14}$  to  $1.406 \times 10^{-14}$   $\text{m}^2/\text{s}$  by considering the QD size as 10 nm, which demonstrates that solution variation during SynSed can effectively suppress the Brownian motion of QDs. Furthermore, the highest sedimentation efficiency is achieved through the process of dehydration-driven transfer, as supported by previous research findings.<sup>21,23</sup> The synergistic effect of Brownian motion suppression and dehydration-driven transfer can efficiently and uniformly sediment nanoparticles from a bulk solution to solid substrates while preventing particle aggregation, which holds promise for addressing the challenges associated with the transfer efficiency and distribution uniformity.

In SynSed, the microwell serves the function of controlling the sedimentation area with its diameter ranging from 2.5 to 4.0 mm. Precise regulation of the microwell's area is crucial for effectively controlling the density of nanoparticles in the plane. When dealing with high-concentration samples, enlarging the microwell ensures that adjacent particles can be resolved by the microscope. Conversely, for ultralow-concentration samples, shrinking the microwell can enhance the imaging efficiency. To prevent the adsorption of the PDMS wall to proteins, the microwell requires pretreatment with mPEG-silane (5 kDa). The efficacy of antiadsorption is shown in Figure S3. Following the SynSed process, images of a 10  $\mu\text{L}$  detection-QD solution at a concentration of 600 fM show bright fluorescence spots when the microwell is treated with mPEG-silane. In contrast, with no mPEG-silane treatment, there are nearly no observable light spots, which are caused by the adsorption of the PDMS wall to proteins.<sup>24</sup> These observations confirm the effectiveness of mPEG-silane treatment in preventing nonspecific adsorption of the PDMS wall.

**3.2. Optimization and Performance of SynSed.** The properties of the polymer added in the QDs solution are important for the successful SynSed and must meet specific



requirements: (1) water solubility, (2) high biocompatibility, (3) appropriate viscosity, and (4) low impact on the emission of QDs. As DEX and PEG are commonly used water-soluble polymers in biochemical analysis,<sup>25</sup> we have examined DEX and PEG with different molecular weights in our study from fluorescence intensity and distribution.

For the assessment of fluorescence intensity, QDs are sedimented from the solution onto the substrate by three methods: dehydration-driven transfer, SynSed with PEG, and SynSed with DEX. The emission of QDs is found to be minimal when they are dried in the air using dehydration-driven transfer. The presence of PEG and DEX films intensified the emission of QDs significantly (Figure S4A,B). So, PEG with molecular weights of 6, 8, and 20 kDa, as well as DEX with molecular weights of 40, 100, and 500 kDa, is further screened to find the best sedimentation effects.

In the investigation of distribution, a solution of 1 pM QDs is mixed with two polymers: 40 kDa DEX and 8 kDa PEG. The final concentration of these two polymers is 0.1% (w/v). After the SynSed and imaging, five frames of images are randomly selected from the central region, and another five frames are selected from the peripheral region randomly for counting. In the case of 40 kDa DEX, the average number of QDs ( $N_{\text{QD}}$ ) in a single-frame image displays minimal differences among the central region, peripheral region, and combined region. The standard deviation of the QD count under each condition is also quite low, as shown in Figure S4C. These findings indicate a uniform distribution of QDs within the 40 kDa DEX film. In contrast, when using 8 kDa PEG, its standard deviation is noticeably larger than that observed with 40 kDa DEX. The variance in distribution between 40 kDa DEX and 8 kDa PEG may be attributed to the higher viscosities of PEG solutions with concentrations exceeding 10% (w/v) (Figure S2). In the subsequent SynSed procedures, 40 kDa DEX was employed at a concentration of 0.1% (w/v) unless otherwise specified.

Accurately quantifying the sedimentation efficiency requires the real concentration of QDs used in the experiment. Although the supplier provided a nominal concentration calculated from the mass and molar mass, it may not be exact because the molar mass of QDs cannot be accurately measured due to the shell cladding and surface modification of functional molecules. To determine the actual number of QDs in a given volume, we employ a dehydration-driven transfer method to ensure that all QDs sediment on the substrate. To minimize the aggregation of QDs, we reduced the quantity of QDs by diluting their concentration and sampling the minimum volume. Simultaneously, we expanded the sedimentation area by allowing the QDs to spread freely without being confined to microwells. These strategies enable all QDs to be individually resolved by the microscope. Subsequently, we capture images of all the QDs within the entire sedimented area using sequential multiframe imaging techniques and manually count them to determine their true number. For 0.1  $\mu\text{L}$  of QD solution, the counted number of QDs has a good linear relationship with the nominal concentrations ranging from 0.25 to 1 pM (Figure S5). However, the counted number of QDs is only 8.0% of that calculated from the nominal concentration. The discrepancy may come from the calculation of mass and molar mass versus single-particle counting. The number of QDs calibrated from this curve is referred to as the "true value" in this report, denoted as  $N_{\text{true}}$ . The sediment efficiency (SE) is then calculated using  $N_{\text{true}}$  and eq 1 provided.

$$\text{SE} = \frac{N_m}{N_{\text{true}}} = \frac{N_{\text{df}} \times \frac{S_{\text{total}}}{S_{\text{df}}}}{N_{\text{true}}} = \frac{N_{\text{df}} \times S_{\text{total}}}{N_{\text{true}} \times S_{\text{df}}} \times 100\% \quad (1)$$

where  $N_m$  represents the counted number of QDs.  $N_{\text{df}}$ ,  $S_{\text{total}}$ , and  $S_{\text{df}}$  represent the average number of QDs in each frame image, the sedimentation area, and the area of the single frame image, respectively.

For 1  $\mu\text{L}$  of 1 pM QD solution, the fluorescence image of QDs via SynSed reveals that QDs are in a single-particle state and distributed uniformly on the substrate (Figure 2A).  $N_{\text{true}}$  as

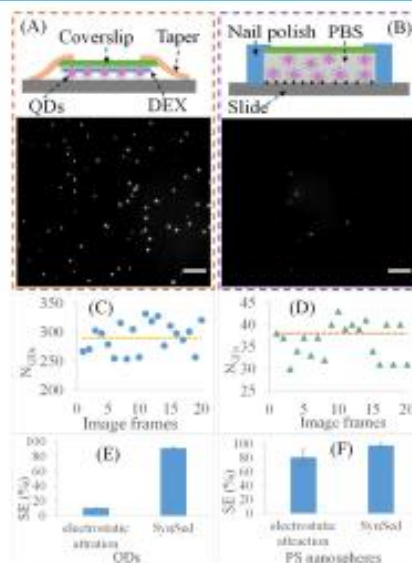


**Figure 2.** Comparison of SynSed (A) and electrostatic attraction sedimentation (B). The concentrations and volumes of QDs solution are 1.0 pM and 1  $\mu\text{L}$  for SynSed, as well as 50 pM and 2  $\mu\text{L}$  for electrostatic attraction sedimentation. Fluctuation in the number of QDs in 20 frames of images obtained from SynSed (C) and electrostatic attraction sedimentation (D). SEs of QDs (E) and PS nanospheres (F) through SynSed and electrostatic attraction sedimentation. Scale bars: 10  $\mu\text{m}$ .

determined by eq 1, is 37568.  $N_{\text{true}}$  is calculated as 41093 using the established calibration curve. The SE of QDs via SynSed reaches 91.4%. Under the same conditions, including sample volume, QD concentration, and microwell, electrostatic attraction sedimentation does not yield any bright and blinking spots. When the concentration and volume of QDs are increased to 50 pM and 2  $\mu\text{L}$ , blinking spots reappear in the images (Figure 2B). The calculated SE for electrostatic attraction is 10.7% (Figure 2E), which is much lower than that of SynSed. The lower SE in electrostatic attraction can be attributed to three factors: (1) a significant portion of QDs remaining in the bulk solution; (2) QDs adsorbed on both the glass slide and coverslip; and (3) loss of QDs along the coverslip's edge. Furthermore, the distribution of QDs is assessed by counting QDs in 20 frames of images. The fluctuation in the number of QDs in each frame is shown in Figure 2C,D. The relative standard deviations (RSDs) of the QDs' numbers are 8.8% for SynSed and 11.0% for electrostatic



attraction, indicating that QDs are distributed uniformly on the substrate through SynSed.

The SE difference between the SynSed and electrostatic attraction methods depends on the particle size. Smaller particles result in a more substantial improvement in SE, whereas larger particles lead to a lower SE ratio between these two methods. As an example, for 1  $\mu\text{L}$  of 0.0002 mg/mL PS nanosphere (198 nm diameter) solution,  $N_m$  is 19656 via SynSed, which is 42.3% of the value provided by the supplier (46440). The SEs are 97.5% for SynSed and 80.7% for electrostatic attraction (Figure 2F). Notably, when the particle size is larger, the SE tends to be higher, but the gap in SE between these two methods becomes smaller. SynSed exhibits a distinct advantage in transferring nanoparticles with ultra-small sizes, such as QDs, noble metal clusters, and carbon dots.

**3.3. Amplification-Free DIAs Using QD Labeling and SynSed.** The processes of DIAs of CEA are shown in Figure 3A. CEA, capture beads, and detection QDs are mixed

times are optimized by using 0.7 fM CEA as a positive control and PBS as a blank (Figure S6). The optimal conditions for immunoreaction are as follows: 100 pM QDs, 800,000 capture beads, 2 h incubation, and 1 round elution. In the final fluorescence images, the bright spots representing detection QDs are increased gradually with the CEA concentration in the range of 0–10 fM (Figure 3B).

The quantitative plots, depicted in Figure 3C, are generated by summing the number of QDs in 10 frames of images. The standard deviations are obtained through triple measurements. The dynamic curve can be divided into two distinct stages. In the initial stage (with concentrations ranging from 10 to 500 aM), the number of QDs is linearly increased with the CEA concentration, and the curve has an exceptionally steep slope, which represents an extremely high detection sensitivity. Within this range, the number of both the capture beads and the QDs significantly surpasses the number of CEA molecules present, which ensures effective immunocapture and highly efficient formation of sandwich immunocomplexes. With the assistance of SynSed, the QDs from immunocomplexes are transferred on the substrate with remarkable efficiency and controllability. The detection sensitivity and precision of DIAs are both enhanced, a fact underscored by the consistently low standard deviation observed at each data point. In the second stage, spanning from 0.5 to 10 fM concentrations, the correlation between the number of detected QDs and the concentration remains linear. However, the slope of this relationship becomes less steep, and the standard deviations at each data point are noticeably higher compared to those of the first stage. This phenomenon could be attributed to a decrease in the efficiency of immunocapture. As the CEA concentration rises, the number of target protein molecules increases rapidly, and there may not be a sufficient number of capture beads available to guarantee effective immunocapture. As a demonstration, we calculated the number ratio of CEA and capture beads, which were 28.1, 140.6, and 281.3% for 1, 5, and 10 fM CEA solutions, respectively, with a fixed volume of 150  $\mu\text{L}$ . Half immunocomplexes, like CEA with detection QDs and CEA with capture beads, appear and become more prominent within the high concentration range. The entire range of CEA measurement spanned from 0.01 to 10 fM, encompassing a remarkable 3 orders of magnitude in concentration. The LOD for the CEA assay, calculated using the blank value plus three standard deviations, was pushed down to an impressively low value of 3.9 aM. However, once the CEA concentration exceeded 10 fM, the fluorescence spots exhibited only minimal increases. This phenomenon can be attributed to what is commonly referred to as the "hook effect". Even at a concentration as high as 10 fM, there are still some unoccupied spaces amidst the fluorescence spots, suggesting that there is room for further augmentation of the density of detection QDs. This, in turn, opens up possibilities for achieving higher concentration detection by improving the immunoreaction efficiency or for the development of multiplex DIAs in the future. To evaluate the repeatability of the established method, we used the capture beads and detection QDs fabricated in the same batch to measure 0.075 fM CEA on different days. The intrabatch variability of the signals is 4.4%. Subsequently, we counted the signals using 1 fM CEA, employing capture beads and detection QDs fabricated in different batches. The interbatch variability of the signals is 10.1%. These results prove that the repeatability and stability of our method are acceptable.

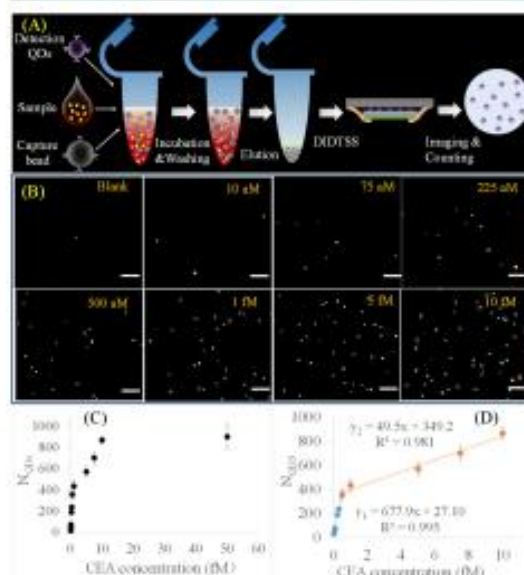


**Figure 3.** (A) Procedure of DIAs incorporating SynSed. (B) Fluorescence images of the detection QDs generated by DIAs at different CEA concentrations. (C) Plots of  $N_{QDs}$  against the CEA concentration acquired from images. (D) Dynamic curve for the measurement of CEA in DIAs. Scale bars: 10  $\mu\text{m}$ .

together, and immunocomplexes are generated by one-step incubation. Unbound CEA and QDs were removed by magnetic separation and washing. QDs in immunocomplexes are eluted by an alkaline solution (pH = 10.9) containing 1.0% (w/v) DEX and collected in tubes via magnetic separation. The number of eluted QDs is linked to the CEA concentration. Then, the collected QD eluent is pipetted into the microwell, and QDs are transferred onto the coverslip uniformly and efficiently via SynSed. After tape sealing, the immobilized QDs were imaged and counted accurately. The performance of DIAs is mainly affected by the efficiency of immunocapture, particle transferring, and imaging. To increase the efficiency of immunocapture, the incubation time, the concentration of detection QDs, the quantity of capture beads, and elution



**3.4. Serum Measurement.** Serum is a complex matrix containing a multitude of proteins spanning a broad concentration range, from nanomolar (nM) to subfemtomolar (sub-fM) levels. To evaluate the impact of the complex matrix, we diluted serum samples without CEA with varying degrees of dilution, ranging from 0 to 60,000-fold. Subsequently, these diluted CEA-free serum samples were analyzed by following the DIA procedure. When the dilution factor increased from 0 to 4-fold, the number of QDs ( $N_{\text{QDs}}$ ) decreased significantly. However, as the dilution factor continued to increase beyond 4-fold,  $N_{\text{QDs}}$  showed only a marginal reduction (Figure 4A),

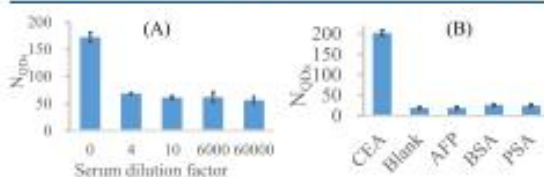


**Figure 4.** (A) DIAs of CEA-free serum with different dilution factors. (B) Specificity evaluation of the CEA measurement. The concentration of all four proteins is 0.7 fM.

indicating that the matrix effect of the serum was minimized when the dilution factor exceeded 4. In the measurement of clinical serum, it is imperative to dilute serum by a factor greater than 4, which is essential for obtaining accurate assay results.

Specificity is a crucial parameter in DIAs as it determines whether immunocomplexes are formed by the target protein or not. Here, we introduced three proteins, namely, AFP, PSA, and BSA, as interfering proteins to assess the specificity of our method. To ensure consistency, we set the concentration of all four proteins at 0.7 fM, thus eliminating the influence of the concentration deviations. Among these proteins, CEA exhibited the highest signal, while the other interfering proteins produced signals that were comparable to the blank sample (Figure 4B). This outcome demonstrates that our method exhibits a remarkable level of specificity when it comes to the CEA assay.

In addition to dilution, another commonly employed method to mitigate the matrix effect in complex matrices is standard addition analysis. In our study, we quantified the diluted serum samples using the standard addition analysis approach. Considering the two-stage curve observed in the buffer, two serum samples containing CEA were diluted to achieve concentrations at aM and fM levels, respectively. The results of the CEA measurements are presented in Figure 5. In the case of sample no. 1, a dilution factor of 60,000 was

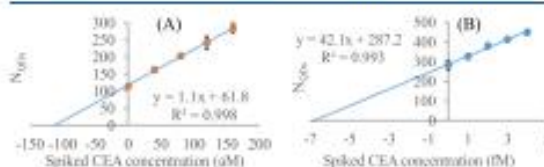


**Figure 5.** (A) Calibration curve of standard addition analysis for serum no. 1 with a dilution factor of 60,000. The measured value of CEA is 58.86 aM. (B) Calibration curve of standard addition analysis for serum no. 2 with a dilution factor of 6000. The measured CEA value is 6.817 fM.

applied, bringing the final CEA concentration into the range corresponding to stage 1 of the calibration curve. The measured CEA concentration was found to be 58.86 aM, equivalent to an initial CEA concentration of 1.34 ng/mL in the serum. The provided CEA value was 0.70 ng/mL. The measured value of CEA is essentially consistent with that provided by the hospital. For sample no. 2, a dilution factor of 6000 was used, placing the final CEA concentration within the range corresponding to stage 2 of the calibration curve. The CEA concentration was determined to be 6.817 fM. The initial CEA concentration in the serum was calculated by multiplying the measured value by the dilution factor, yielding a concentration of 8.16 ng/mL. The hospital-provided value for CEA was 1.71 ng/mL. There is indeed a discrepancy between the measured values and those provided by the hospital. This deviation could be attributed to three factors: (1) different sources of antibodies, (2) variations in the purity and bioactivity of the standard CEA, and (3) a substantial dilution factor (6000), which has the potential to amplify measuring errors during the recovery from the diluted sample to the initial serum. The successful measurement of CEA in serum at aM levels demonstrates that the established method exhibits exceptional sensitivity, specificity, accuracy, and robustness, which holds great promise as a potential technique for quantifying rare proteins in complex clinical samples such as NFL and P-tau 181.

## 4. CONCLUSIONS

We have developed a novel technique that enables the efficient and uniform transfer of nanoparticles from a solution to a solid-phase surface via the synergistic effect of Brownian motion suppression and dehydration transfer. After optimizing the types, concentrations, and molecular weights of polymers, the highest achieved SEs reach 91.7% for QDs and 97.5% for PS nanospheres when utilizing the SynSed method. These SE values are markedly superior to those attained through the electrostatic attraction method, which yielded SEs of only 10.7% for QDs and 80.7% for PS nanospheres. Furthermore, the distribution of nanoparticles on the substrate via SynSed is comparable or slightly more uniform to that via electrostatic attraction. Using CEA as a model, DIAs for CEA are carried out through a single-step incubation of capture beads, CEA, and detection QDs; subsequent elution of the bound detection QDs; and highly efficient SynSed. The incorporation of SynSed in DIAs addresses the shortcomings related to sampling efficiency, effectively reducing the LOD to 3.9 aM and expanding the dynamic range to cover 3 orders of magnitude in concentration, ranging from 0.01 to 10 fM. Based on the established method, the CEA values measured in serum using standard addition analysis match those provided by the hospital across the entire dynamic range. This method possesses high sensitivity, specificity, accuracy, and precision, highlighting its significant potential in the early screening of biomarkers and disease progression monitoring.

## ■ ASSOCIATED CONTENT

### Supporting Information

The Supporting Information is available free of charge at <https://pubs.acs.org/doi/10.1021/acs.analchem.3c05066>.

Performance comparison of various DIAs, processes of two sedimentation methods, solution viscosity–concentration plot, calibration curve of QD number,



optimization of immunoassay conditions, and demonstration of the successful modification of antibodies (PDF)

## AUTHOR INFORMATION

### Corresponding Author

Hongwei Gai – School of Chemistry and Materials Science,  
Jiangsu Normal University, Xuzhou, Jiangsu 221116, China;  
orcid.org/0000-0002-1069-9543; Email: gai@  
jnu.edu.cn

### Authors

Qingquan Zhang – School of Chemistry and Materials  
Science, Jiangsu Normal University, Xuzhou, Jiangsu 221116,  
China

Wenwen Chai – School of Chemistry and Materials Science,  
Jiangsu Normal University, Xuzhou, Jiangsu 221116, China

Xiaoyan Pan – Department of Laboratory Medicine, The  
Second Affiliated Hospital of Zhejiang University School of  
Medicine, Hangzhou 310009, China

Complete contact information is available at:

<https://pubs.acs.org/10.1021/acs.analchem.3c05066>

### Author Contributions

<sup>§</sup>Q.Z. and W.C. contributed equally.

### Notes

The authors declare no competing financial interest.

## ACKNOWLEDGMENTS

We thank the support from the Natural Science Foundation of China (NSFC grant 22174056) and the Xuzhou Key Plan of R&D (grant KC20170).

## REFERENCES

- (a) Abdelhak, A.; Foschi, M.; Abu-Rumelleh, S.; Yue, J. K.; D'Anna, L.; Huss, A.; Oeckl, P.; Ludolph, A. C.; Kuhle, J.; Petzold, A.; Manley, G. T.; Green, A. J.; Otto, M.; Tumani, H. *Nat. Rev. Neurol.* **2022**, *18* (3), 158–172. (b) Teunissen, C. E.; Verberk, I. M. W.; Thijssen, E. H.; Vermunt, L.; Hansson, O.; Zetterberg, H.; van der Flier, W. M.; Mielke, M. M.; Del Campo, M. *Lancet Neurol.* **2022**, *21* (1), 66–77.
- (a) Wu, Y.; Tilley, R. D.; Gooding, J. J. *J. Am. Chem. Soc.* **2019**, *141* (3), 1162–1170.
- (a) Barletta, J. M.; Edelman, D. C.; Constantine, N. T. *Am. J. Clin. Pathol.* **2004**, *122* (1), 20–27.
- (a) Janelidze, S.; Mattsson, N.; Palmqvist, S.; Smith, R.; Beach, T. G.; Serrano, G. E.; Chai, X.; Proctor, N. K.; Eichenlaub, U.; Zetterberg, H.; Blennow, K.; Reiman, E. M.; Stomrud, E.; Dage, J. L.; Hansson, O. *Nat. Methods* **2020**, *26* (3), 379–386.
- (a) Taylor, M. S.; Wu, C.; Fridy, P. C.; Zhang, S. J.; Senussi, Y.; Wolters, J. C.; Cajuso, T.; Cheng, W.-C.; Heaps, J. D.; Miller, B. D.; Mori, K.; Cohen, L.; Jiang, H.; Molloy, K. R.; Chait, B. T.; Goggins, M. G.; Bhan, L.; Franses, J. W.; Yang, X.; Taplin, M.-E.; Wang, X.; Christiani, D. C.; Johnson, B. E.; Meyerson, M.; Uppaluri, R.; Egloff, A. M.; Denault, E. N.; Spring, L. M.; Wang, T.-L.; Shih, I.-M.; Fairman, J. E.; Jung, E.; Arora, K. S.; Yilmaz, O. H.; Cohen, S.; Sharova, T.; Chi, G.; Norden, B. L.; Song, Y.; Nieman, L. T.; Pappas, L.; Parikh, A. R.; Strickland, M. R.; Corcoran, R. B.; Mustelin, T.; Eng, G.; Yilmaz, O. H.; Matulonis, U. A.; Chan, A. T.; Skates, S. J.; Rueda, B. R.; Drapkin, R.; Klempner, S. J.; Deshpande, V.; Ting, D. T.; Rout, M. P.; LaCava, J.; Walt, D. R.; et al. *Cancer Discovery* **2023**, *13*, 2532–2547.
- (a) Zhdanov, A.; Keefe, J.; Franco-Walke, L.; Konnalyan, K. R.; Pyayt, A. *Biosens. Bioelectron.* **2018**, *103*, 138–142.

- (a) Pillai-Kastoori, L.; Schutz-Geschwender, A. R.; Harford, J. A. *Anal. Biochem.* **2020**, *593*, 113608. (b) Sule, R.; Rivera, G.; Gomes, A. *Biotechniques* **2023**, *75*, 99–114.
- (a) Schoof, E. M.; Furtwangler, B.; Uresin, N.; Rapin, N.; Savickas, S.; Gentil, C.; Lechman, E.; Keller, U. A. D.; Dick, J. E.; Porse, B. T. *Nat. Commun.* **2021**, *12* (1), 3341.
- (a) Kuo, C.-W.; Smith, A. M. *Acc. Chem. Res.* **2023**, *56* (9), 1031–1042. (b) Liu, H.; Lei, Y. *Biosens. Bioelectron.* **2021**, *177*, 112901.
- (a) Shim, J.-u.; Ranasinghe, R. T.; Smith, C. A.; Ibrahim, S. M.; Hoffelder, F.; Huck, W. T. S.; Klenerman, D.; Abell, C. *ACS Nano* **2013**, *7*, 5955–5964. (b) Wu, C.; Garden, P. M.; Walt, D. R. *J. Am. Chem. Soc.* **2020**, *142* (28), 12314–12323. (c) Yellenwarapu, V.; Buser, J. R.; Haber, M.; Baron, J.; Inapuri, E.; Issadore, D. *Proc. Natl. Acad. Sci. U.S.A.* **2019**, *116* (10), 4489–4495. (d) Akama, K.; Shirai, K.; Suzuki, S. *Anal. Chem.* **2016**, *88* (14), 7123–7129. (e) Rissin, D. M.; Kan, C. W.; Campbell, T. G.; Howes, S. C.; Fournier, D. R.; Song, L.; Piech, T.; Patel, P. P.; Chang, L.; Rivnak, A. J.; Ferrell, E. P.; Randall, J. D.; Provuncher, G. K.; Walt, D. R.; Duffy, D. C. *Nat. Biotechnol.* **2010**, *28* (6), 595–599.
- (a) Kony, T.; Hayman, R. B.; Walt, D. R. *Anal. Chem.* **2009**, *81*, 5777–5782.
- (a) Ma, C.; Wang, F.; Wang, X.; Han, L.; Jing, H.; Zhang, H.; Shi, C. *Chem. Commun.* **2017**, *53*, 10696–10699. (b) Skarratt, K. K.; Fuller, S. J. *J. Microbiol. Methods* **2014**, *96*, 99–100.
- (a) Ma, J.; Zhan, L.; Li, R. S.; Gao, P. F.; Huang, C. Z. *Anal. Chem.* **2017**, *89* (16), 8484–8489.
- (a) Zhang, Q.; Li, J.; Pan, X.; Liu, X.; Gai, H. *Anal. Chem.* **2021**, *93* (38), 12848–12853. (b) Liu, X.; Huang, C.; Dong, X.; Liang, A.; Zhang, Y.; Zhang, Q.; Wang, Q.; Gai, H. *Chem. Commun.* **2018**, *54* (93), 13103–13106. (c) Liu, X.; Huang, C.; Zong, C.; Liang, A.; Wu, Z.; Zhang, Y.; Zhang, Q.; Zhao, W.; Gai, H. *ACS Sens.* **2018**, *3*, 2644–2650. (d) Liu, X.; Sun, Y.; Lin, X.; Pan, X.; Wu, Z.; Gai, H. *Anal. Chem.* **2021**, *93*, 3089–3095.
- (a) Farika, Z.; Mickert, M. J.; Hlavacek, A.; Skladal, P.; Gorris, H. *H. Anal. Chem.* **2017**, *89* (21), 11825–11830. (b) Li, X.; Wei, L.; Pan, L. L.; Yi, Z. Y.; Wang, X.; Ye, Z. J.; Xiao, L. H.; Li, H.-W.; Wang, J. F. *Anal. Chem.* **2018**, *90*, 4807–4814.
- (a) Kusumi, A.; Tsunoyama, T. A.; Hirose, K. M.; Kasai, R. S.; Fujiwara, T. K. *Nat. Chem. Biol.* **2014**, *10*, 524–532.
- (a) Palacios, M. A.; Lacy, M. M.; Schubert, S. M.; Manesse, M.; Walt, D. R. *Anal. Chem.* **2013**, *85* (14), 6639–6645.
- (a) Li, J.; Wuethrich, A.; Sina, A. A. L.; Cheng, H.-H.; Wang, Y.; Behren, A.; Mainwaring, P. N.; Trau, M. *Nat. Commun.* **2021**, *12*, 1087.
- (a) Liu, X.; Wu, Z.; Zhang, Q.; Zhao, W.; Zong, C.; Gai, H. *Anal. Chem.* **2016**, *88*, 2119–2124.
- (a) Liu, X.; Lin, X.; Pan, X.; Gai, H. *Anal. Chem.* **2022**, *94*, 5830–5837.
- (a) Zhang, Q.; Zhang, X.; Li, J.; Gai, H. *Anal. Chem.* **2020**, *92* (1), 654–658.
- (a) Mahler, H. C.; Friess, W.; Grauschopf, U.; Kiese, S. J. *Pharmaceut. Sci.* **2009**, *98* (9), 2909–2934.
- (a) Hlavacek, A.; Krivankova, J.; Brozkova, H.; Weissova, J.; Pizurova, N.; Foret, F. *Anal. Chem.* **2022**, *94* (41), 14340–14348.
- (a) Xu, Y.; Jiang, H.; Wang, E. *Electrophoresis* **2007**, *28* (24), 4597–4605. (b) Shen, K.; Hu, X.; Li, Z.; Liao, M.; Zhuang, Z.; Ruane, S.; Wang, Z.; Li, P.; Micciulla, S.; Kasinathan, N.; Kalonia, C.; Lu, J. R. *Mol. Pharm.* **2023**, *20* (5), 2502–2512.
- (a) Zhang, Q.; Chen, J.; Zhong, Z.; Li, B.; Gai, H. *Anal. Chim. Acta* **2022**, *1197*, 339540.



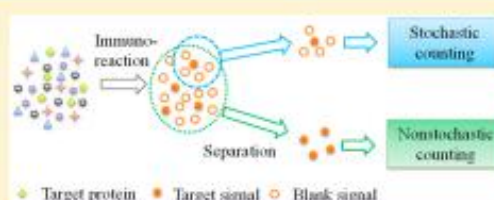
# Nonstochastic Protein Counting Analysis for Precision Biomarker Detection: Suppressing Poisson Noise at Ultralow Concentration

Qingquan Zhang,<sup>†</sup> Xuebing Zhang,<sup>†</sup> Jiajia Li, and Hongwei Gai<sup>\*†</sup>

Jiangsu Key Laboratory of Green Synthesis for Functional Materials, School of Chemistry and Materials Science, Jiangsu Normal University, Xuzhou, Jiangsu 221116, China

<sup>†</sup> Supporting Information

**ABSTRACT:** Protein counting analysis obtains the quantitative results of specific protein through counting the number of target signals and displays a great value in disease diagnosis. Current protein counting techniques just stochastically count a small portion of the target signal, which causes a considerable information loss and limits the accuracy and precision of the protein assay at ultralow concentration. Here, we present a nonstochastic and ultrasensitive protein counting method through combining multiround evaporation-induced particle sedimentation, grid-assisted multiframe imaging, and microscope-enhanced high-resolution signals. Using carcinoembryonic antigen (CEA) as the model, the dynamic range was from  $5 \times 10^{-18}$  M (aM) to  $5 \times 10^{-16}$  M, and the limit of detection was 4.9 aM. For CEA-spiked plasma detection, the relative standard deviation and the relative error of CEA concentrations were both lower than 8.0%, and the recoveries reached 92.5% and 98.8% for 20.0 aM and 40.0 aM CEA respectively. Two clinical plasma samples were measured by the standard addition method, and the results showed little deviation with the values provided by the hospital. The established approach suppresses Poisson noise of the stochastic counting, offers ultrahigh sensitivity, and features a remarkable potential in early disease screening.



The onset, progression, and recurrence of diseases are associated with the abnormal expression of proteins or expression of unique proteins,<sup>1</sup> such as cancer protein biomarkers,<sup>2</sup> neurodegenerative biomarkers,<sup>3</sup> and specific cytokines.<sup>4</sup> Accurate quantitative analysis of disease-relevant proteins is useful in disease prevention and control, early cancer screening, and precision diagnostics.<sup>5,6</sup>

Clinically, the gold standard method for specific protein measurement is immune assay, including enzyme-linked immunosorbent assays (ELISAs), and its variants.<sup>7</sup> The quantitative data of ELISAs depends on the exact intensity of ensemble signal from tubes or microtiter plates. As proteins are present in complex biological samples with high background and sensitive to ambient environments, the typical limit of detection (LOD) of ELISAs is at the picomolar level.<sup>8</sup> Various approaches are developed to amplify the signal, such as PCR reaction,<sup>9</sup> enzyme reaction,<sup>10</sup> and functional nanopores (e.g., quantum dots, Au nanoparticles, etc.).<sup>11</sup> However, the fluctuation of signal intensity is inevitable and may be exacerbated by the bias effect in some signal amplification methods,<sup>12</sup> which restricts the lowering of LOD and the improvement of reproducibility.

The protein counting assay is an ultrasensitive protein quantification technique developed in recent years.<sup>13</sup> The quantitative results are extracted from the number of generated targeted signals, not requiring the intensity of each target signal. The yes/no measurement model overcomes the influence of intensity fluctuation and presents an outstanding

potential in low-abundant protein measurement.<sup>14</sup> To date, protein counting assay techniques are developed into three categories: digital ELISA,<sup>15,16</sup> single particle counting,<sup>17–19</sup> and single-fluorescent-molecule flow counting.<sup>20</sup> In digital ELISA and single-particle counting, target signals coexist with massive blank signals. Under limited detection throughput, blank signals occupy a majority of detection sites, and only a small portion of target signals are counted.<sup>21</sup> The stochastic counting of a small part of the signals leads to a significant Poisson noise at ultralow concentration ( $10^{-15}$ – $10^{-18}$  M) and small sample volume ( $10^{-6}$  L). In order to prevent the occupation of blank signals, single-fluorescent-molecule flow counting utilizes a separation and enrich strategy and achieves a detection of fluorescent molecules one by one through capillary electrophoresis. However, the fluorescence of a single molecule is so weak as to require a very tiny detection volume ( $10^{-15}$  L level).<sup>22</sup> A large number of fluorescent molecules bypass the laser spot, causing an intolerable signal loss. When the fluorescent molecules are less than 3000, the counting date is not reproducible.<sup>23</sup> Therefore, the omission of the target signal during the counting process is becoming the bottleneck of protein counting techniques.<sup>24</sup> It is essential to develop a

Received: October 21, 2019

Accepted: December 10, 2019

Published: December 10, 2019



novel counting approach to achieve 100% counting of target signal.

Herein, we present a nonstochastic and inexpensive protein counting method for low-abundant protein analysis. Using carcinoembryonic antigen (CEA) as a model, the LODs reach  $4.9 \times 10^{-18}$  M (aM) in a buffer and 6.1 aM in a 10-fold diluted plasma.

## EXPERIMENTAL SECTION

**CEA Immunoassay Procedure.** Here, 300  $\mu$ L of capture-antibody-modified magnetic bead (capture bead) solution ( $2 \times 10^6$  beads/mL) was transferred into a low-adsorption tube. The supernatant was removed by magnetic separation. Then, 100  $\mu$ L of CEA standards (concentration could be varied) was added into the tube and incubated for 1 h at room temperature with slow tilt and rotation. After the removal of the supernatant, 300  $\mu$ L of a 10-fold diluted SuperBlock (PBS) blocking buffer (containing 0.1% tween 20) was added to inhibit specific adsorption for 0.5 h. Then, 100  $\mu$ L of detection-antibody-coated polystyrene sphere (DPS sphere) solution was added and incubated for 1 h. After magnetic separation, the unbound DPS spheres were removed by three times washing with a PBS buffer containing 0.1% Tween 20. Immuno-complexes and unoccupied capture beads were left in the tube.

Next, 100  $\mu$ L of citrate buffer (pH 3.1) was added in the tube and mixed for 2 min. The bound DPS spheres were stripped from immuno-complexes. Based on magnetic separation, the supernatant containing eluted DPS spheres was transferred into a new tube. After three times elution, all the eluted DPS spheres were collected with a volume of  $\sim 300$   $\mu$ L. Then, the DPS sphere solution was centrifuged for 5 min (6000  $r/min$ ), and  $\sim 290$   $\mu$ L of supernatant was removed. The final obtained target DPS sphere suspension was  $\sim 10$   $\mu$ L.

We pipetted 4  $\mu$ L of enriched DPS sphere suspension into the microwell and evaporated the liquid on a 90  $^{\circ}$ C hot plate. By repeating the above processes for three or four rounds, all the eluted DPS spheres were precipitated in a microwell of a counting device (Figure S1). Then, we pipetted 3  $\mu$ L of DI water and placed a coverslip. The immobilized DPS spheres were recorded by an inverted microscope equipped with a 40 $\times$  objective (numerical aperture of the 40 $\times$  objective was 0.6) and an EMCCD frame by frame and counted by software. The total immunoassay procedure needed about 3.0 h.

**Matrix Effect and Specificity Investigation.** Here, 0.5 mL of human plasma was added in an ultrafilter with a 100 kDa molecular weight cutoff and centrifuged for 5 min (12,000  $r/min$ ) to obtain CEA-free plasma. Then, a portion of CEA-free plasma was diluted 4-, 10-, 100-, 1000-, and 100,000-fold, respectively, by a PBS buffer and detected. To evaluate the specificity, we spiked proper volumes of the CEA standards into 100  $\mu$ L of 10% CEA-free plasma with final concentrations of 0.0, 20.0, and 40.0 aM, respectively. After immunoreaction, all the eluted DPS spheres were counted by software.

**Analysis of Clinical Plasma.** Two human plasmas were diluted by PBS buffer with a dilution factor of 100,000. The diluted plasmas were measured by a standard addition method.

## RESULTS AND DISCUSSION

**Principle of Protein Counting Analysis.** Figure 1 shows the protein counting processes based on sandwich immunoassay. Capture beads, target proteins, and DPS spheres were incubated in sequence. Since the ratio of antigen to capture

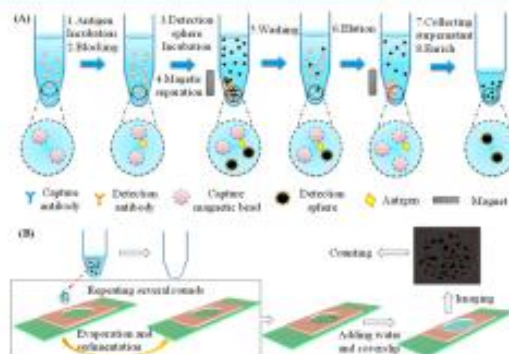


Figure 1. Scheme of nonstochastic protein counting analysis. (A) Processes of digital immunoassay. (B) Counting method of particle signal.

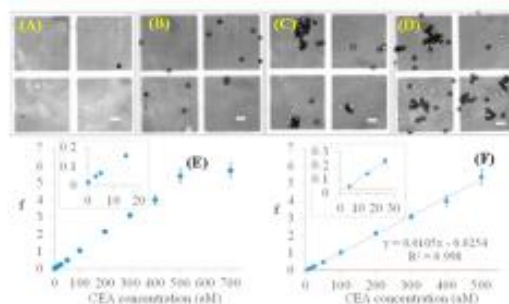


Figure 2. Measurement of CEA in buffer. (A–D) Distribution of DPS spheres by using 0 aM (A), 15 aM (B), 50 aM (C), and 100 aM (D) CEA solution. (E) Plots of calculated  $f$  against CEA concentration. Inset: plots in 0–15 aM. (F) Linear dose curve of  $f$  and CEA concentration. Inset: curve in 5–25 aM. Broken line represents the LOD. Error bars: s.d. over three replicates. Scale bars: 8  $\mu$ m.

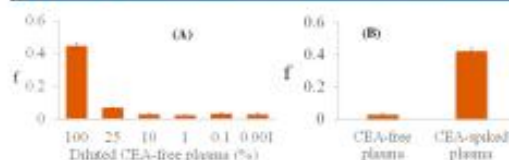


Figure 3. Matrix effect and specificity of immunoassay. (A) Variation of background noise by using CEA-free plasma with different dilutions. (B) Results of specificity test. The final concentration of spiked CEA in 10% CEA-free plasma was 40.0 aM.

bead was typically smaller than 1:10, each immuno-complex was just composed of one capture bead, one antigen molecule, and one DPS sphere. The unbound DPS spheres were removed by washing. Then, the bound DPS spheres were stripped off from the immuno-complexes by elution and enriched in a tube (Figure 1A). Through several rounds of suspension pipetting and a liquid evaporation process, the eluted DPS spheres were immobilized in a microwell, imaged frame by frame under the help of locating grids, and counted by a custom-built software (Figure 1B). To calibrate the



Table 1. Accuracy, Precision, and Recovery for Measurement of CEA spiked into 10% CEA-Free Plasma ( $n = 3$ )

For marker	Reference value (aM)	Detection value (aM)	Accuracy (RE %)	Precision (RSD %)	Recovery (%)
CEA	20.0	18.5 ± 1.3	7.5	7.0	92.5 ± 6.5
CEA	40.0	39.5 ± 1.6	1.3	4.1	98.8 ± 4.0

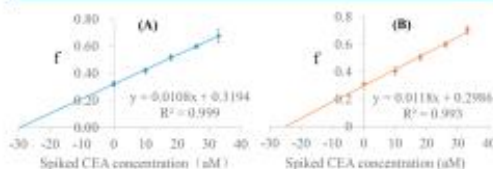


**Figure 4.** Calibration curves of standard addition analysis. Experimental conditions: 600,000 beads, 0.72  $\mu$ g of capture antibody, 1.5 h of antigen incubation, 0.5 h of blocking, 1.0 h of DPS sphere incubation, 340,000 DPS spheres (3.0  $\mu$ m), 1.18  $\mu$ g of detection antibody, three times washing and elution. (A) #1 plasma and (B) #2 plasma.

protein concentration, we introduced a ratio coefficient ( $f$ ).  $f$  was calculated as

$$f = \frac{N_{\text{DPS}}}{N_{\text{CB}}} \times 100 \quad (1)$$

where  $N_{\text{DPS}}$  and  $N_{\text{CB}}$  represent the number of target DPS spheres and capture beads, respectively.

In eq 1,  $N_{\text{CB}}$  affected the capture efficiency of the target protein.  $N_{\text{DPS}}$  was determined by the protein concentration. Under the optimal value of  $N_{\text{CB}}$ , the  $f$  value was mainly affected by the protein concentration and should have a linear relationship with the concentration. As the original ratio of  $N_{\text{DPS}}$  and  $N_{\text{CB}}$  was too small, we added an amplification factor of 100 to display the results clearly.

To achieve complete counting of all target signals, we improved the counting efficiency from three aspects: (1) Micrometer-scale DPS spheres were used to enhance signal resolution, preventing the information loss caused by signal overlapping in particle clusters. (2) Multiple rounds of evaporation-induced sedimentation ensured that all target DPS spheres were immobilized in a limited area with a high density. (3) Grid-assisted multiframe imaging enabled the immobilized DPS spheres to be imaged without omission and overlap. Therefore, we could count all target DPS spheres exactly, suppress the Poisson noise resulting from stochastic counting of a portion of the target signal, and improve the performance of the protein counting analysis.

**Optimization of Experimental Parameters.** The basis of the protein counting assay is the formation of immune-complexes. By using 5 aM CEA molecules, 400,000 capture beads, and 340,000 DPS spheres, we observed asymmetric complexes formed with one capture bead (smaller bead) and one DPS sphere prior to elution (Figure S2A). Meanwhile, almost no complex appeared in the blank experiment (Figure S2B). These results demonstrated the possibility of protein counting preliminarily.

To obtain as many as possible immune-complexes, some experimental parameters were optimized by using a 5 aM CEA solution as the positive control and PBS buffer as the negative control (Figure S3). For the antigen capture, the optimal conditions were 600,000 capture beads, 1.5 h of antigen incubation, 0.72  $\mu$ g of capture antibodies, and 0.5 h of blocking

time. For the binding of DPS spheres to captured antigens, the best parameters were as follows: 340,000 DPS spheres, 1 h of DPS sphere incubation, and 1.18  $\mu$ g of detection antibodies.

The concentration of antibodies was considerably higher than that of antigens, implying that the captured antigen was surrounded by numerous unoccupied antibodies. The antigen dissociated from an antibody could rebound to the surface with a high probability,<sup>25</sup> which ensured the highly efficient binding of target proteins to antibodies and allowed the washing of immuno-complexes. In this case, we washed the immuno-complexes with different times (Figure S3D). During the first magnetic separation (washing times was zero), a large number of free DPS spheres existed in the solution. Some free DPS spheres might co-sediment with capture beads, resulting in a relatively high value of  $f$ . In the first washing, the co-sediment phenomena were reduced greatly. Thus, the  $f$  value lowered more than 50%. The optimal signal-to-noise ratio was obtained by washing three times.

The elution process is to separate the DPS spheres and preclude interference of capture beads during counting. In this study, a citrate buffer (pH 3.1) was used as the elution buffer. We have carried out the elution experiment more than three times to improve the elution efficiency. By counting the DPS spheres (4.5  $\mu$ m) left in the capture beads (Figure 1A, step 4), we discovered that the number of noneluted DPS spheres (20–30) was negligible after three times elution (Figure S3H). Thus, the immuno-complexes were eluted three times in subsequent experiments.

Current nanoparticle-based protein counting techniques fail in counting all target signals because of two reasons: (1) The sedimentation efficiency is difficult to reach 100% even under electrostatic attraction. (2) The signals overlap in particle clusters. In this study, we developed an evaporation-induced particle sedimentation method to ensure that all DPS spheres were immobilized onto the substrate surface. It was noted that evaporation-induced precipitation led to obvious particle aggregation, limiting its application in nanoparticle sedimentation because a single nanoparticle was not resolved in clusters. To enhance the resolution of single particles, we used 2.0 and 3.0  $\mu$ m DPS spheres to carry out immune reactions and found that 3.0  $\mu$ m DPS spheres could be distinguished in clusters clearly (Figure S4). Thus, 3.0  $\mu$ m DPS spheres were used in the immune assay.

Once the DPS spheres were immobilized, multiframe bright-field photos were captured in sequence under the help of locating grids. Then, all photos were assembled together, and a combined image of the circular microwell was recovered (Figure S5A), demonstrating that all immobilized DPS spheres were imaged without omission and overlap. The DPS spheres in each frame were clear and sharp (Figures S5B and C). To accelerate the counting speed, a particle counting software was established. The counting accuracy was tested by comparing the results obtained by the software and the operator (Table S1). For 14 random frames, the counted DPS spheres displayed a high level of consistency between the operator and software.



**Performance of CEA Standards Measurement.** To evaluate the performance, CEA standards were analyzed under optimal conditions. The density of DPS spheres steadily increased with CEA concentration (Figure 2A–D). The quantitative results were obtained by plotting the calculated  $f$  values against the CEA concentrations (Figure 2E). The plots of the calculated  $f$  values exhibited a linear dose curve from 5 to 500 aM (Figure 2F). The relative standard deviation (RSD,  $n = 3$ ) varied from 2.2% to 7.7%, which was acceptable for a protein assay. In the dynamic range, RSD and the relative error (RE,  $n = 3$ ) fluctuated randomly, displaying no clear tendency. When the CEA concentration exceeded 500 aM,  $f$  deviated from a linear curve, which might be caused by two reasons: (1) More than one capture bead were bound to the same DPS sphere. (2) The effective collision for an antigen-bound capture bead was decreased with an increase in antigen-bound capture beads. The LOD was estimated to be 4.9 aM by extrapolating the concentration at background plus thrice the standard deviation (s.d.). In contrast with other protein counting assays, this method achieved the counting of all target DPS spheres, suppressed Poisson noise, and improved the LOD.

**Specificity, Accuracy, and Precision.** Clinical samples typically contain tens of thousands of protein species, which interfere with the detection of target proteins. To investigate the matrix effects, CEA-free plasmas were analyzed at different dilution folds. The background noise declined within a 0–10-fold dilution. When the dilution fold was more than 10, the background noise varied slightly (Figure 3A). In the 10-fold-diluted CEA-free plasma, the blank value was  $0.027 \pm 0.005$ , and a LOD of  $\sim 6.1$  aM was obtained, which was equivalent to a LOD of  $\sim 61$  aM in the whole plasma. This detection sensitivity was at least  $\sim 5$ -fold lower than that of digital ELISA<sup>30</sup> and 1–3 orders of magnitude lower than that of the single-nanoparticle counting analysis.<sup>17</sup> For the specificity test, the great gap between CEA-free plasma and CEA-spiked plasma revealed that CEA measurements were not interfered with by nontarget proteins (Figure 3B). In addition, RSD and RE of CEA concentrations were lower than 8.0%, and the recoveries reached  $92.5\% \pm 6.5\%$  and  $98.8\% \pm 4.0\%$  for 20.0 and 40.0 aM CEA spiked plasma, respectively (Table 1). These results ensured the accuracy and precision of trace target protein detection.

**Clinical Sample Detection.** The CEA concentration in the whole plasma of normal peoples is  $\sim 5$  ng/mL, exceeding the dynamic range of our method. So, we performed a  $10^5$ -fold dilution to the plasmas before analysis. To eliminate the matrix effect, the standard addition method was applied to calibrate concentration. We measured the  $f$  values of two diluted plasmas and calculated the original CEA concentration in the whole plasma on the basis of the standard addition curves (Figure 4). The final obtained CEA concentrations were 0.53 and 0.46 ng/mL respectively. These data showed a little difference with those provided by the hospital (0.54 and 0.78 ng/mL). This might be attributed to the different sources of the proteins and antibodies because the sources of proteins usually affected the activities and purity of the proteins.

## CONCLUSION

In conclusion, we present a nonstochastic protein counting method for the quantification of low-abundant protein. Through a combination of multiround evaporation-induced particle sedimentation and grid-assisted multiframe imaging, all

the target signals counted exactly. The dynamic range of the CEA measurement was 5–500 aM, and the LODs were 4.9 aM in buffer and 6.1 aM in 10-fold diluted plasma. For spiked-CEA detection in 10% CEA-free plasma, the accuracy (RE < 8.0%), precision (RSD < 7.0%), and recoveries were acceptable. Following the established procedure, two clinical plasmas were quantified by the standard addition method and showed comparable values with those provided by the hospital. The proposed method suppressed Poisson noise of the stochastic counting, improved the LOD and accuracy of the low-abundant protein assay, and displayed considerable potential in rare biomarker detection and early disease screening.

## ASSOCIATED CONTENT

### Supporting Information

The Supporting Information is available free of charge at <https://pubs.acs.org/doi/10.1021/acs.analchem.9b04809>.

Additional experiments, figures, and tables(PDF)

## AUTHOR INFORMATION

### Corresponding Author

\*E-mail: [gai@jnu.edu.cn](mailto:gai@jnu.edu.cn). Fax: 86-516-83536972.

### ORCID

Hongwei Gai: 0000-0002-1069-9543

### Author Contributions

<sup>†</sup>These authors contributed equally.

### Notes

The authors declare no competing financial interest.

## ACKNOWLEDGMENTS

The authors are grateful to the Natural Science Foundation of China (NSFC 21575053), the project of Six Talent Peaks (2017SWYY-013), the “333” project of Jiangsu Province, and the Natural Science Foundation of the Jiangsu Higher Education Institutions of China (16KJJA150006).

## REFERENCES

- Walt, D. R. *Lab Chip* **2014**, *14*, 3195–3200.
- Wu, L.; Qu, X. *Chem. Soc. Rev.* **2015**, *44*, 2963–2997.
- Georganopoulou, D. G.; Chang, L.; Nam, J. M.; Thaxton, C. S.; Mufson, E. J.; Klein, W. L.; Mirkin, C. A. *Proc. Natl. Acad. Sci. U. S. A.* **2005**, *102*, 2273–2276.
- Wollert, K. C.; Kempf, T.; Wallentin, L. *Clin. Chem.* **2017**, *63*, 140–151.
- Kim, S.-J.; Choi, S.-J.; Jang, J.-S.; Cho, H.-J.; Kim, L.-D. *Acc. Chem. Res.* **2017**, *50*, 1587–1596.
- Borrebaeck, C. A. K. *Nat. Rev. Cancer* **2017**, *17*, 199–204.
- Kelley, S. O. *Acc. Chem. Res.* **2017**, *50*, 503–507.
- Ma, F.; Li, Y.; Tang, B.; Zhang, C. Y. *Acc. Chem. Res.* **2016**, *49*, 1722–1730.
- Chang, L.; Li, J.; Wang, L. *Anal. Chim. Acta* **2016**, *910*, 12–24.
- Numata, S.; Katakami, H.; Inoue, S.; Sawada, H.; Hashida, S. *Ann. Clin. Biochem.* **2016**, *53*, 495–503.
- Zhou, W.; Gao, X.; Liu, D.; Chen, X. *Chem. Rev.* **2015**, *115*, 10575–10636.
- Fu, Y.; Li, C.; Lu, S.; Zhou, W.; Tang, F.; Xie, X. S.; Huang, Y. *Proc. Natl. Acad. Sci. U. S. A.* **2015**, *112*, 11923–11928.
- Witters, D.; Sun, B.; Begolo, S.; Rodriguez-Manzano, J.; Robles, W.; Ismagilov, R. F. *Lab Chip* **2014**, *14*, 3225–3232.
- Basu, A. S. *SLAS Technol.* **2017**, *22*, 387–405.
- Shim, J.-u.; Ranasinghe, R. T.; Smith, C. A.; Ibrahim, S. M.; Hollfelder, F.; Huck, W. T. S.; Klenerman, D.; Abell, C. *ACS Nano* **2013**, *7*, 5955–5964.



- (16) Leirs, K.; Tewari Kumar, P.; Decrop, D.; Perez-Ruiz, E.; Leblebici, P.; Van Kelst, B.; Compernelle, G.; Meeuws, H.; Van Wesenbeeck, L.; Lagatie, O.; Stuyver, L.; Gils, A.; Lammertyn, J.; Spasic, D. *Anal. Chem.* **2016**, *88*, 8450–8458.
- (17) Liu, X.; Huang, C.; Dong, X.; Liang, A.; Zhang, Y.; Zhang, Q.; Wang, Q.; Gai, H. *Chem. Commun.* **2018**, *54*, 13103–13106.
- (18) Liu, X.; Huang, C.; Zong, C.; Liang, A.; Wu, Z.; Zhang, Y.; Zhang, Q.; Zhao, W.; Gai, H. *ACS Sensors* **2018**, *3*, 2644–2650.
- (19) Liu, X.; Zhang, Y.; Liang, A.; Ding, H.; Gai, H. *Chem. Commun.* **2019**, *55*, 11442–11445.
- (20) Gilbert, M.; Livingston, R.; Felberg, J.; Bishop, J. J. *Anal. Biochem.* **2016**, *503*, 11–20.
- (21) Rissin, D. M.; Kan, C. W.; Campbell, T. G.; Howes, S. C.; Fournier, D. R.; Song, L.; Piech, T.; Patel, P. P.; Chang, L.; Rivnak, A. J.; Ferrell, E. P.; Randall, J. D.; Provuncher, G. K.; Walt, D. R.; Duffy, D. C. *Nat. Biotechnol.* **2010**, *28*, 595–599.
- (22) Gooding, J. J.; Gaus, K. *Angew. Chem., Int. Ed.* **2016**, *55*, 11354–11366.
- (23) Chen, D.; Dovichi, N. J. *Anal. Chem.* **1996**, *68*, 690–696.
- (24) Zhang, Y.; Noji, H. *Anal. Chem.* **2017**, *89*, 92–101.
- (25) Chang, L.; Rissin, D. M.; Fournier, D. R.; Piech, T.; Patel, P. P.; Wilson, D. H.; Duffy, D. C. *J. Immunol. Methods* **2012**, *378*, 102–115.
- (26) Song, L.; Lachno, D. R.; Hanlon, D.; Shepro, A.; Jeromin, A.; Gemani, D.; Talbot, J. A.; Racke, M. M.; Dage, J. L.; Dean, R. A. *Alzheimer's Res. Ther.* **2016**, *8*, 58.

## Digital Duplex Homogeneous Immunoassay by Counting Immunocomplex Labeled with Quantum Dots

Xiaojun Liu,<sup>§</sup> Yuanyuan Sun,<sup>§</sup> Xinyi Lin, Xiaoyan Pan, Zhangjian Wu, and Hongwei Gai\*

Cite This: *Anal. Chem.* 2021, 93, 3089–3095

Read Online

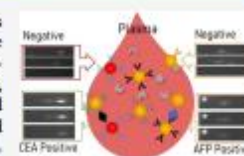
ACCESS |

Metrics & More

Article Recommendations

Supporting Information

**ABSTRACT:** Digital multiplexed homogeneous immunoassay is supposed to have the advantages of high sensitivity, high analytical throughput, small sampling errors, and low consumption. We present a spectral imaging-based multiplex, homogenous immunoassay by counting sandwich-structured immunocomplexes in the form of quantum dot (QD) aggregates. As a proof of concept, the method was utilized to detect two tumor biomarkers: carcino-embryonic antigen (CEA) and  $\alpha$ -fetoprotein (AFP). The immunocomplex induced by CEA contained QD 655 and QD 585 and were recognized by the spectral pattern of dual-color QD aggregates under a transmission-grating-based spectral imaging microscope. Immunocomplexes induced by AFP were labeled with the QD 585 aggregate and were identified by the spectral blue-shift pattern of same-color QD aggregates. Limits of detection for AFP and CEA were calculated to be 0.02 and 0.10 pM at a signal-to-noise ratio of 3, respectively. Further successful quantification of the model proteins in human plasma demonstrated the accuracy and reliability of our approach.



Single-molecule counting (digital detection) is at the forefront of immunoassays because it meets the requirements of early diagnosis,<sup>1–3</sup> quantifying biomarkers in the range of sub-fM to aM. In theory, digital immunoassay has the potential to detect a single molecule of a biomarker by “visualizing” a tag-labeled antibody or a sandwich-structured immunocomplex containing at least two tag-labeled antibodies. Similar to immunoassays, digital immunoassays are divided into two classes, heterogeneous<sup>4–9</sup> and homogeneous.<sup>3,10–16</sup> In homogeneous immunoassays, sandwich-structured immunocomplexes can be distinguished from the free tag-labeled antibodies, without any separation steps. Therefore, digital homogeneous immunoassays are considered more promising due to easy operation, cost-effectiveness, and minimal artificial interference. To count sandwich-structured immunocomplexes, various detection strategies were developed, such as fluorescence and scattering light cross-correlation spectrum from a compound of a silver nanoparticle and organic dye,<sup>10</sup> quenching of upconversion nanoparticles by gold nanoparticles,<sup>11</sup> Förster resonance energy transfer (FRET) between organic dyes,<sup>12,16</sup> asynchronous spectral shift of aggregated quantum dots (QDs) in the same color (same-color QD aggregate),<sup>15</sup> dual-color fluorescent dyes or QD colocalization,<sup>13,14</sup> and plasmonic resonance energy transfer (PRET) between QD and gold nanoparticles.<sup>15</sup> However, such strategies were only used to detect single protein biomarkers.

A panel of protein biomarkers provides more comprehensive information on pathological processes than a single biomarker and remarkably improves diagnosis and prognosis.<sup>17</sup> Multiplex immunoassays offer significant advantages over a series of single-plex assays, including decreased sampling errors and reduction in labor, time, sample, and reagent.<sup>18–21</sup> Low sample consumption is crucial for rare samples such as cerebrospinal

fluid obtained through lumbar puncture. Therefore, multiplex immunoassays with the desired sensitivity and specificity are urgently needed for clinical applications.

To recognize immunocomplexes in heterogeneous multiplex immunoassays, researchers usually use two strategies. One is the spatial position, where the signal is detected.<sup>18–20,22–26</sup> Specific domains of the sensor are decorated with destined antibodies, and thus, immunocomplexes can be easily identified by the signal location. Typical examples are various array-based immunoassays, such as electrode arrays,<sup>18</sup> nanowire arrays,<sup>22</sup> microfluidic channel arrays,<sup>23,24</sup> nanopore arrays,<sup>25</sup> and dot arrays of surface-enhanced Raman scattering (SERS) substrates.<sup>26</sup> Another was a destined tag-labeled antibody for a specific immunocomplex.<sup>21,27–32</sup> Nanoplasmonic particles,<sup>27</sup> SERS tags,<sup>28,29</sup> electrochemical tags,<sup>30</sup> QDs,<sup>31</sup> organic fluorescent dyes,<sup>30</sup> and magnetic beads<sup>32</sup> were exploited for these assays. By removing the analyte unbound to the sensor and the tag-labeled antibody unbound to the analyte, limits of detection (LODs) of multiplexed heterogeneous immunoassays were in the range of sub-nM to fM. However, multiple cycles of incubation and washing were needed during measurement. Each cycle increased the risk of cumulative error, cost time, and labor. Therefore, multiplex, separation-free homogeneous immunoassays are desirable.

Received: September 22, 2020

Accepted: January 27, 2021

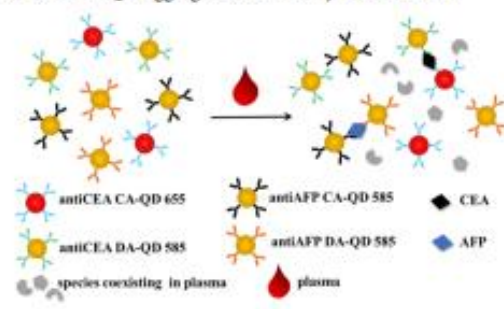
Published: February 4, 2021





The key of multiplex homogeneous immunoassays is how to distinguish signals of each sandwich-structured immunocomplex without isolating the immunocomplex, which makes multiplexed homogenous immunoassays a challenge. To the best of our knowledge, rare studies achieved multiplexed, homogeneous immunoassays at the cost of sensitivity.<sup>33–37</sup> In their studies, signal enhancement between the SERS tag and noble metal nanoparticles,<sup>33</sup> localized surface plasmon resonance shift of gold nanorods caused by analytes,<sup>37</sup> time-resolved FRET between dyes,<sup>34</sup> and fluorescent intensity of online-captured microbeads<sup>35,36</sup> were used for simultaneous quantitative analysis of proteins. The aforementioned studies were performed at the ensemble level and could not achieve the ultimate detection sensitivity of chemical assays, to count the number of single molecules without any further chemical amplification or enrichment steps. This study developed a spectral imaging-based multiplex homogenous immunoassay by counting sandwich-structured immunocomplexes in the form of QD aggregates. As a proof of concept, carcinoembryonic antigen (CEA) and  $\alpha$ -fetoprotein (AFP) were selected as model targets, and QD 585 and QD 655 were used as fluorescent tags. As shown in Scheme 1, a tumor marker

Scheme 1. QD Aggregates Induced by CEA and AFP



protein and its two corresponding antibodies immobilized onto their own QDs formed a sandwich-structured immunocomplex. An immunocomplex induced by AFP and CEA was considered as a same-color QD aggregate (QD 585s) and a two-color QD aggregate (QD 585 and QD 655), respectively. Observed under a transmission-grating-based single-particle spectral imaging microscope, the spectrum of the two-color QD aggregate showed a zeroth-order dot and two first-order streaks, while the spectra of the remaining species, including the dispersed QDs and the same-color QD aggregates, originally exhibited one zeroth-order dot and one first-order streak. Therefore, the immunocomplex induced by CEA was identified by the spectral pattern of two first-order streaks and then counted. In our previous studies, we found that the first-order streak of same-color QD aggregates split before bleaching, whereas that of a dispersed QD did not.<sup>39,40</sup> Therefore, the immunocomplex induced by AFP was recognized by the criterion, the first-order streak splitting under continuous irradiation, and then was counted. The LODs in solution for AFP and CEA were calculated to be 0.02 and 0.10 pM at a signal-to-noise ratio of 3, respectively. The successful quantification of the model targets in human plasma demonstrated the reliability of our approach in clinical applications.

## EXPERIMENTAL SECTION

**Chemicals and Materials.** AFP, AFP capture antibody (CA), AFP detection antibody (DA), CEA, CEA CA, and CEA DA were ordered from Shanghai Linc-Bio Science Co. Ltd. (Shanghai, China). Bovine serum albumin, chicken egg albumin, trypsin inhibitor, human serum albumin, phytohemagglutinin, transferrin, fibrinogen, poly (diallyldimethylammonium chloride), and *N*-(3-(dimethylamino)propyl)-*N*-ethylcarbodiimide hydrochloride (EDC) were purchased from Sigma-Aldrich (St. Louis, MO). A total of 4.0 mM phosphate-buffered saline (PBS, pH 7.2) containing 155.2 mM NaCl, carboxylic QD 655 (Cat. No. Q21321MP), carboxylic QD 585 (Cat. No. Q21311MP), a blocking reagent (Cat. No. 37580), positively charged glass slides (Cat. No. 4951plus4), and coverslips were obtained from Thermo Scientific (Waltham, MA). The chromatographic matrix, Superose 6, was purchased from GE Healthcare Life Science (Pittsburgh, PA). A transmission grating with 70 lines/mm was purchased from Edmund Scientific (Barrington, NJ).

**Instruments.** A Cary Eclipse fluorescence spectrophotometer and 1260 Infinity liquid chromatography (Agilent Technologies) were used to measure the QD fluorescence intensity and to purify QDs coated with antibodies, respectively. Single-particle spectral images were taken by an Olympus IX71 microscope equipped with an Evolve 512 electron-multiplied charge-coupled device (EMCCD) (Photometrics, Tucson).

**QDs Modified with Antibody.** QDs were modified with a destined antibody according to the procedure provided by the manufacturer. Taking an example of QD 655 modified with CEA CA (antiCEA CA-QD 655), 5.0  $\mu$ L of QD 655 was activated with 10.0  $\mu$ L of freshly prepared 1.0 mg/mL EDC. The solution was filtered in a centrifugal ultrafiltration tube of 50 kDa cutoff molecular weight to get rid of excessive EDC, and then 12.0  $\mu$ L of CEA CA was added into this QD 655 solution. The reaction lasted for 4 h in the dark. AntiCEA CA-QD 655 was purified with size exclusion chromatography (details in the Supporting Information and Figure S1). Figure S1 shows that antiCEA CA-QD 655 was separated from the excessive CEA CA and QD 655. AntiCEA CA-QD 655 was collected and stored in a 4  $^{\circ}$ C refrigerator. The AntiCEA CA-QD 655 concentration was determined according to the fluorescence intensity of QD 655. QD 585 modified with CEA DA (antiCEA DA-QD 585), QD 585 modified with AFP DA (antiAFP DA-QD 585), and QD 585 modified with AFP CA (antiAFP CA-QD 585) were prepared following the above procedure. The working curves for QD 655 and QD 585 were  $y = 841.7x - 360.2$  (correlation coefficient of 0.997) and  $y = 1007.9x - 602.5$  (correlation coefficient of 0.999), respectively.

**Immunoreaction in PBS Buffer.** All of the probes were blocked with a 5.0% (v/v) blocking reagent for 30.0 min prior to use. A total of 9.5  $\mu$ L of 8.43 nM antiCEA CA-QD 655, 8.4  $\mu$ L of 9.55 nM antiCEA DA-QD 585, 8.5  $\mu$ L of 9.40 nM antiAFP DA-QD 585, 7.3  $\mu$ L of 11.00 nM antiAFP CA-QD 585, and 4.0  $\mu$ L of protein in PBS buffer were mixed. The mixture was filled up to 80.0  $\mu$ L with PBS buffer, and the 80.0  $\mu$ L solution was referred to as the immunoreaction solution. The reaction lasted for 0.5 h in the dark. Each experiment was repeated at least three times.

**Immunoreaction in Plasma.** The plasma samples were from Xuzhou Center Hospital. All subjects signed the written



informed consents. Blank plasma was used as a matrix whose background and recovery were supposed to be matched with plasma. The blank plasma was prepared by removing AFP and CEA through filtering the plasma in a centrifugal ultrafiltration tube of 30 kDa cutoff molecular weight. The immunoreaction was conducted according to the above protocol, except that 4.0  $\mu\text{L}$  of protein in PBS buffer was replaced with 10.0  $\mu\text{L}$  of protein in the blank plasma or 10.0  $\mu\text{L}$  of the plasma sample or 10.0  $\mu\text{L}$  of the plasma sample spiked with CEA and AFP (the concentration of the spiked CEA and AFP was 160.0 pM). CEA and AFP in the plasma samples were measured with an electrochemiluminescence immunoassay analyzer, Cobas 8000,<sup>38</sup> by Xuzhou Center Hospital.

**Specimen for Single-Particle Spectral Imaging.** Each antibody-modified QD in the immunoreaction solution was diluted to 0.025 nM with PBS buffer, and this diluted solution was referred to as the test solution. A total of 1.5  $\mu\text{L}$  of the test solution was dropped onto a positively charged glass slide from Thermo Scientific, covered with a coverslip, and sealed with nail polishing oil. The commercial glass slide was coated with poly-L-lysine and used without any treatment. It was supposed that the immunocomplex was adsorbed onto this slide through the binding of its negatively charged, acidic amino acids to the positively charged poly-L-lysine. Only QDs adsorbed onto a glass slide could be imaged. Compared to a normal glass slide that was negatively charged, this positively charged glass slide made adhesion of the negatively charged QDs faster and easier due to electrostatic attraction. The specimen was ready for single-particle spectral imaging.

**Transmission-Grating-Based Single-Particle Spectral Imaging.** Scheme S1 shows the principle of a transmission-grating-based spectral imaging. A transmission grating was inserted before EMCCD. The transmission grating split light from one emitter into two beams: a zeroth-order beam in the shape of a dot and a first-order beam in the shape of a streak. The zeroth-order beam and the first-order beam were referred to as the zeroth-order dot and the first-order streak, respectively. The wavelength ( $\lambda$ ) conformed to the formula  $\lambda = L \times d/S$ , where  $S$ ,  $d$ , and  $L$  are the distance between the transmission grating and the EMCCD, the grating constant, and the distance between the zeroth-order dot and the corresponding first-order streak, respectively. In our setup, the value of  $d/S$  was measured to be 2.95 nm/pixel using QD 655 as the standard.

To ensure single-particle spectral imaging, the total concentration of QDs in the test solution should be below 0.40 nM. For each specimen, 13 locations were randomly imaged. For each location, images were automatically taken into a group with a 300 ms interval until QD 585 was bleached.

**Image Analysis.** The images were opened with Image J. Figure S2 shows a typical single-particle spectral image. The first step was to make a pair of the zeroth-order dot and the first-order streak from the same emitter by their positions. As shown in Figure S2, when the graph drawn by connecting the dots was similar to that by the streaks, the dot and the streak in the same positions of the graphs were paired. The graph was adjusted by deleting (inserting) the dot (the streak). The zeroth-order dot and the first-order streak that could not make a pair were not counted in the subsequent analysis. Totally, 10 images out of 13 were randomly selected, and all of the QDs in these images were processed. The number of QDs was around 300. The second step was to identify the QD color by the distance between the zeroth-order dot and the first-order

streak, which could be done by the naked eye because the distance difference between QD 655 and QD 585 was obvious (Figure S3). The QD with a large distance was identified as QD 655. The rest of the QDs were identified as QD 585s. The third step was to count the QD 655, the QDs with one dot and two streaks, and the QD 585 whose first-order streak split before bleaching.

## RESULTS AND DISCUSSION

**Proposed Principle.** The core of the multiplexed homogenous immunoassay is to distinguish the signal of each immunocomplex from that of the rest of the substances without separation.<sup>34–37</sup> Single-particle detection can directly observe single particles and discover particle heterogeneity hidden in ensemble detection.<sup>1–3</sup> For example, single-particle transmission-grating-based spectral imaging is capable of distinguishing the same-color QD aggregate from the dispersed QD by its spectral blue-shift pattern.<sup>39,40</sup> The first-order streak of the same-color QD aggregate splits before bleaching, whereas that of the dispersed QD does not. This characteristic was exploited for a single-plex homogenous immunoassay with femtomolar LOD.<sup>15</sup> Based on these studies, we believe that single-particle detection might have great potential in multiplex homogeneous immunoassays.

As a concept, a duplex homogenous immunoassay based on single-particle detection was developed with QD 585 and QD 655 as probes and with CEA and AFP as model biomarkers. As shown in Scheme 1, a specific biomarker and two corresponding antibodies that were immobilized onto their own QDs formed a sandwich-structured immunocomplex when they met. The immunocomplex induced by CEA and AFP could be regarded as the two-color QD aggregate (QD 585 and QD 655) and the same-color QD aggregate (QD 585), respectively. When observed under an optical microscope, the aggregated QDs in an immunocomplex could not be observed as multiobjects but as one because the distance between the QDs was less than the optical diffraction limitation.<sup>14,15</sup> When observed under a single-particle transmission-grating-based spectral microscope, it is reasonable to deduce that (1) the QD aggregate exhibits one zeroth-order dot because its dots, which spread in the direct transmission direction, overlap; (2) the two-color QD aggregate shows two first-order streaks because the streaks of the aggregated QD 655 and QD 585 cannot overlap (Figure S2); and (3) the rest of the QDs (the same-color QD aggregates and the dispersed QDs) exhibit one first-order streak at the beginning of imaging. Therefore, the immunocomplex induced by CEA can be recognized by the unique spectral pattern of the two-color QD aggregate, one dot and two streaks. The aggregate of QD 585 is supposed to be identified by the criterion, the first-order streak splitting before bleaching, as mentioned previously.

To test our hypothesis, we compared the response of the two pairs of probes in the presence of CEA and AFP to that in the absence of CEA and AFP. Videos S1–S4 show the typical spectral changes with time. For convenient reading, the videos were edited into a series of frames and are shown in Figure 1A–D. As expected, in the absence of the targets, the spectrum patterns of all of the probes were the same, a dot and a streak at the beginning of imaging, and the streaks did not split with irradiation time increasing (Figure 1A,B). By contrast, in the presence of targets, the spectrum patterns of a dot and two streaks appeared at the beginning of imaging (Figure 1C). Some streaks split before bleaching (Figure 1D). These



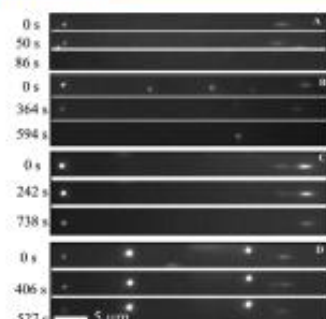


**Figure 1.** Typical spectral change with time. (A) Antibody-modified QD 585 and (B) antibody-modified QD 655 in the absence of CEA and AFP; (C) two-color QD aggregate (QD 585 and QD 655) and (D) same-color QD aggregate (QD 585) in the presence of CEA and AFP. The concentration of each antibody-modified QD was 0.025 nM, and the concentration of both CEA and AFP was 0.035 nM.

phenomena supported the existence of the two-color QD aggregate and the same-color QD aggregate (QD 585), respectively. Therefore, the sandwich-structured immunocomplex induced by CEA and that by AFP were successfully identified.

The multiplexed capacity of our approach might be further increased. Theoretically, each two-QD aggregate represents one biomarker, and thus the number of two-QD aggregates is equal to that of biomarkers that can be simultaneously quantified by our approach. The number of two-QD aggregates is the sum of the two-color QD aggregates and the same-color QD aggregates. The number of two-color QD aggregates is  $C(n, 2) = n!/[2!(n-2)!] = n(n-1)/2$ , and the number of same-color QD aggregates is  $n$ . Therefore,  $n(n+1)/2$  kinds of biomarkers can be simultaneously detected using  $n$  kinds of QDs. For example, for two QDs in different colors, three biomarkers can be detected.

**Cross-Reactivity and Selectivity.** Multiplex immunoassays must exclude cross-talking between targets. Two sets of comparisons were performed to evaluate the cross-talking between the targets. One was to compare the responses of a specific probe pair to its matched target with that to all of the targets (Figure 2). Another was to compare the response of a specific probe pair to the nonmatched target with that to PBS buffer (Figure 2). Since QDs were randomly adsorbed onto a slide through electrostatic attraction, the number of adsorbed sandwich-structured immunocomplexes was normalized by the adsorbed QD 655 according to the following equation:

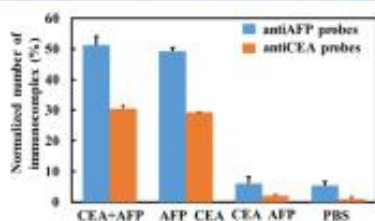


**Figure 2.** Cross-reactivity between targets. The concentration of both CEA and AFP is 0.025 nM.

$nN_{\text{immuno}} = N_{\text{immuno}}/N_{\text{QD 655}}$ , where  $nN_{\text{immuno}}$ ,  $N_{\text{immuno}}$ , and  $N_{\text{QD 655}}$  represent the normalized number of adsorbed sandwich-structured immunocomplexes, the number of adsorbed sandwich-structured immunocomplexes, and the number of adsorbed QD 655, respectively. For each pair of probes, we draw the following conclusions from Figure 2. (1) The  $nN_{\text{immuno}}$  value of the matched target alone was close to that of all of the targets. (2) The  $nN_{\text{immuno}}$  value of the nonmatched target was close to that of the PBS buffer. (3) The  $nN_{\text{immuno}}$  value of the matched target was much higher than that of the PBS buffer. These results indicated there was no cross-talking between the targets.

Good selectivity is crucial to accurately quantify targets when dealing with clinical samples. To assess selectivity, we compared the response of the probes to the targets (2.8 nM) with that to some species (13.8 nM) existing in plasma in Figure 3. The  $nN_{\text{immuno}}$  values of those species were almost

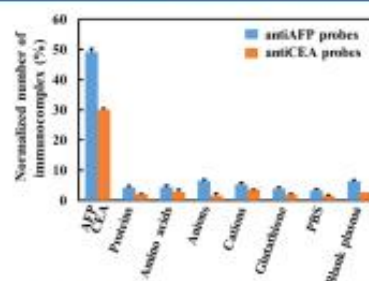


**Figure 3.** Selectivity. Proteins: human serum albumin, fibrinogen, transferrin, epidermal growth factor, concanavalin A, trypsin inhibitor, lectin, and oval albumin. Amino acids: glycine, alanine, valine, isoleucine, leucine, proline, phenylalanine, tryptophan, methionine, tyrosine, serine, cysteine, threonine, asparagine, aspartic acid, glutamine, glutamic acid, lysine, arginine, and histidine. Anions:  $\text{Cl}^-$ ,  $\text{SO}_4^{2-}$ , and  $\text{CO}_3^{2-}$ . Cations:  $\text{K}^+$ ,  $\text{Na}^+$ ,  $\text{Mg}^{2+}$ ,  $\text{Ca}^{2+}$ ,  $\text{Fe}^{2+}$ , and  $\text{Cu}^{2+}$ . The blank plasma was prepared through filtering the plasma with a centrifugal ultrafiltration tube with 30 kDa cutoff molecular weight.

equal to that of the PBS buffer and much lower than that of the targets. To further evaluate selectivity, the response of the probes to the targets was compared with that of blank plasma (Figure 3). The  $nN_{\text{immuno}}$  values of the blank plasma were a little bigger than that of the PBS buffer and by far smaller than that of the targets. The results demonstrated the good selectivity of our duplex homogenous immunoassay.

**Detection in PBS Buffer.** The performance of the duplex homogenous immunoassay was evaluated in PBS buffer. Figure 4 shows the relationship between the  $nN_{\text{immuno}}$  value and the target concentration. For each target, the  $nN_{\text{immuno}}$  value was in positive proportion to the logarithm of the target concentration at low concentration and in negative proportion to the logarithm of the target concentration at high concentration. The working curve in the shape of an inverted "V" had been reported in studies on singleplex homogenous immunoassays.<sup>13–15</sup> The reasons for the inverted V working curve were as follows. (1) When the probes were excessive, all of the immunocomplexes existed in the form of a sandwich-structured complex that contained QD aggregates. Therefore, the  $nN_{\text{immuno}}$  value increased with target concentration. (2) When the target was excessive, the immunocomplex existed in two forms: the sandwich-structured immunocomplex and the

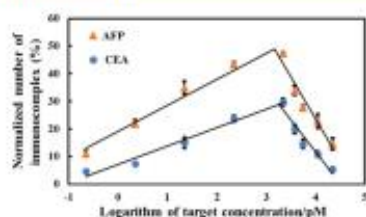


Figure 4. Plot of normalized number of immunocomplexes against the logarithm of target concentration in PBS buffer.

target-antibody immobilized onto a QD. With the target concentration increasing, less QD aggregate immunocomplexes formed and, correspondingly, more one-QD immunocomplexes formed. Therefore, the  $nN_{\text{immuno}}$  value decreased with target concentration. To use the inverted V working curve correctly, the sample and the sample spiked with a small amount of standard target are required to be measured. If the  $nN_{\text{immuno}}$  value of the sample is bigger, then the negative slope will be used. Otherwise, the positive slope will be used. The LODs for CEA and AFP were estimated to be 0.10 and 0.02 pM at a signal-to-noise ratio of 3, respectively. The LOD values were comparable to those of high-quality, multiplexed, and heterogeneous immunoassays.<sup>16–21</sup> The limits of quantification (LOQs) for CEA and AFP were calculated to be 0.3 and 0.1 pM at a signal-to-noise ratio of 10, respectively. The high sensitivity of our immunoassay might be attributed to the excellent resolution of each immunocomplex.

**Stability.** Stability was reflected by the response of the probes from the same batch to the same sample every 2 days and the response of the probes from different batches to the same sample. The  $nN_{\text{immuno}}$  values in the two groups are quite stable, as shown in Figure 5A,B. The relative standard deviations (RSD) of the  $nN_{\text{immuno}}$  values were in the range of 0.6–3.9%, indicating that our approach has good reproducibility.

**Detection in Plasma.** Duplex homogeneous immunoassays were subsequently performed in blank plasma. The

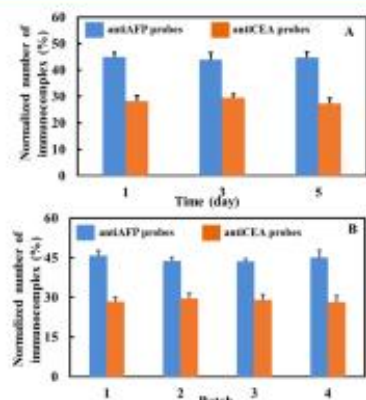


Figure 5. Stability. (A) Response of the probes from the same batch and (B) response of the probes from different batches to the same sample.

blank plasma was prepared by filtering the plasma in a centrifugal ultrafiltration tube of 30 kDa cutoff molecular weight to remove CEA and AFP. The  $nN_{\text{immuno}}$  values of the blank plasma spiked with different amounts of CEA and AFP were measured following the aforementioned procedures. Figure 6 presents the standard calibration curves in blank

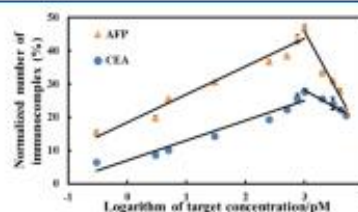


Figure 6. Plot of the normalized number of immunocomplexes against the logarithm of target concentration in blank plasma.

plasma. The curves were highly similar to those in PBS buffer. The LODs in blank plasma for CEA and AFP were estimated to be 0.02 and 0.10 pM, respectively. The LOQs for both CEA and AFP appeared to be 0.30 pM. The values basically agreed with those in PBS buffer, indicating that the blank plasma worked well.

Plasma samples were spiked with AFP and CEA, and the concentration of both spiked AFP and CEA was 160 pM. The  $nN_{\text{immuno}}$  values of the plasma samples and the spiked plasma samples were determined and used to quantify AFP and CEA according to the standard calibration curve in blank plasma. Table 1 summarizes our AFP and CEA concentration values in

Table 1. Comparison between Values Measured by Us and by the Hospital

sample number		our values (pM)		recovery (%)	plasma by hospital (pM)
		plasma	spiked plasma		
1	CEA	9.2 ± 0.2	173.1 ± 0.4	102.4 ± 0.6	15.5 ± 1.8
	AFP	53.9 ± 0.5	235.9 ± 0.2	113.8 ± 0.7	51.5 ± 2.4
2	CEA	6.9 ± 0.1	172.2 ± 1.0	103.3 ± 1.1	9.5 ± 2.0
	AFP	72.6 ± 0.2	227.1 ± 0.3	93.8 ± 0.5	92.9 ± 1.3
3	CEA	45.2 ± 0.6	217.3 ± 0.6	107.6 ± 1.2	43.5 ± 1.9
	AFP	28.4 ± 1.0	180.7 ± 0.8	95.2 ± 1.8	32.9 ± 2.6
4	CEA	33.3 ± 0.4	182.4 ± 0.3	93.2 ± 0.7	39.0 ± 1.7
	AFP	27.0 ± 0.6	196.6 ± 0.9	106.0 ± 1.5	25.7 ± 1.3

the plasma and the spiked plasma and the plasma values measured by the hospital. Our values were close to those by the hospital. The recoveries ranged from 93.2 to 113.8%, as shown in Table 1. The results verified the reliability of our approach in clinical tests.

## CONCLUSIONS

A duplex homogenous immunoassay was conducted by counting each immunocomplex. Immunocomplexes induced by CEA and AFP were identified by the unique spectral pattern of a two-color QD aggregate and the unique blue-shift pattern of the same-color QD aggregate, respectively. The LODs are comparable to those of high-quality heterogeneous immunoassays. Our approach has great potential in clinical



applications, as verified by the successful quantification of the model targets in human plasma.

## ■ ASSOCIATED CONTENT

### Supporting Information

The Supporting Information is available free of charge at <https://pubs.acs.org/doi/10.1021/acs.analchem.0c04020>.

Antibody-modified QD purification, transmission-grating-based spectral imaging microscope, experimental condition optimization, clinical sample test by standard addition, and fraction of the immunocomplexes imaged (PDF)

Spectral changes of an antibody-modified QD 655 with time in the absence of CEA and AFP (Video S1) (AVI)

Spectral changes of an antibody-modified QD 585 with time in the absence of CEA and AFP (Video S2) (AVI)

Spectral changes of an aggregate of QD 585 and QD 655 induced by CEA with time in the presence of CEA and AFP (Video S3) (AVI)

Spectral changes of an aggregate of QD 585 and QD 585 induced by AFP with time in the presence of CEA and AFP (Video S4) (AVI)

## ■ AUTHOR INFORMATION

### Corresponding Author

Hongwei Gai – School of Chemistry and Materials Science, Jiangsu Normal University, Xuzhou 221116, Jiangsu, China; [orcid.org/0000-0002-1069-9543](mailto:orcid.org/0000-0002-1069-9543); Email: [gai@jssu.edu.cn](mailto:gai@jssu.edu.cn)

### Authors

Xiaojun Liu – School of Chemistry and Materials Science, Jiangsu Normal University, Xuzhou 221116, Jiangsu, China

Yuan Yuan Sun – School of Chemistry and Materials Science, Jiangsu Normal University, Xuzhou 221116, Jiangsu, China

Xinyi Lin – School of Chemistry and Materials Science, Jiangsu Normal University, Xuzhou 221116, Jiangsu, China

Xiaoyan Pan – School of Medicine, The Second Affiliated Hospital of Zhejiang University, Hangzhou 310009, Zhejiang, China

Zhangjian Wu – School of Chemistry and Materials Science, Jiangsu Normal University, Xuzhou 221116, Jiangsu, China

Complete contact information is available at:

<https://pubs.acs.org/doi/10.1021/acs.analchem.0c04020>

### Author Contributions

<sup>3</sup>X. Liu and Y. Y. Sun contributed equally.

### Notes

The authors declare no competing financial interest.

## ■ ACKNOWLEDGMENTS

The authors thank the support from the Natural Science Foundation of China (NSFC 21775057) and Natural Science Foundation of the Higher Education Institutions of Jiangsu Province (16KJA150006).

## ■ REFERENCES

- (1) Farka, Z.; Mickert, M. J.; Pastucha, M.; Mikusova, Z.; Skladal, P.; Gorris, H. H. *Angew. Chem., Int. Ed.* **2020**, *59*, 10746–10773.
- (2) Gooding, J. J.; Gaus, K. *Angew. Chem., Int. Ed.* **2016**, *55*, 11354–11366.

- (3) Ma, F.; Li, Y.; Tang, B.; Zhang, C. Y. *Acc. Chem. Res.* **2016**, *49*, 1722–1730.
- (4) Macdonald, P. J.; Ruan, Q.; Tetin, S. Y. *Anal. Biochem.* **2019**, *566*, 139–145.
- (5) Zhang, Q.; Zhang, X.; Li, J.; Gai, H. *Anal. Chem.* **2020**, *92*, 654–658.
- (6) Wang, X.; Walt, D. R. *Chem. Sci.* **2020**, *11*, 7896–7903.
- (7) Cohen, L.; Cul, N.; Cai, Y.; Garden, P. M.; Li, X.; Weitz, D. A.; Walt, D. R. *ACS Nano* **2020**, *14*, 9491–9501.
- (8) Farka, Z.; Mickert, M. J.; Hlavacek, A.; Skladal, P.; Gorris, H. H. *Anal. Chem.* **2017**, *89*, 11825–11830.
- (9) Wang, Y.; Yang, Y.; Chen, C.; Wang, S.; Wang, H.; Jing, W.; Tao, N. *ACS Sens.* **2020**, *5*, 1126–1131.
- (10) Wang, J.; Huang, X.; Liu, H.; Dong, C.; Ren, J. *Anal. Chem.* **2017**, *89*, 5230–5237.
- (11) Li, X.; Wei, L.; Pan, L.; Yi, Z.; Wang, X.; Ye, Z.; Xiao, L.; Li, H.-W.; Wang, J. *Anal. Chem.* **2018**, *90*, 4807–4814.
- (12) Li, H. T.; Zhou, D. J.; Beowne, H.; Balasubramanian, S.; Klennerman, D. *Anal. Chem.* **2004**, *76*, 4446–4451.
- (13) Liu, X.; Zhang, Y.; Liang, A.; Ding, H.; Gai, H. *Chem. Commun.* **2019**, *55*, 11442–11445.
- (14) Liu, X.; Huang, C.; Zong, C.; Liang, A.; Wu, Z.; Zhang, Y.; Zhang, Q.; Zhao, W.; Gai, H. *ACS Sens.* **2018**, *3*, 2644–2650.
- (15) Liu, X.; Huang, C.; Dong, X.; Liang, A.; Zhang, Y.; Zhang, Q.; Wang, Q.; Gai, H. *Chem. Commun.* **2018**, *54*, 13103–13106.
- (16) Gooding, J. J.; Gaus, K. *Angew. Chem., Int. Ed.* **2016**, *55*, 11354–11366.
- (17) Frampton, J. P.; White, J. B.; Simon, A. B.; Tsuei, M.; Paczesny, S.; Takayama, S. *Sci. Rep.* **2014**, *4*, No. 4878.
- (18) Munge, B. S.; Stracensky, T.; Gamez, K.; DiBiase, D.; Rusling, J. F. *Electroanalysis* **2016**, *28*, 2644–2658.
- (19) Li, J.; Macdonald, J. *Biosens. Bioelectron.* **2016**, *85*, 998–999.
- (20) Kingsmore, S. F. *Nat. Rev. Drug Discovery* **2006**, *5*, 310–320.
- (21) Leng, Y.; Sun, K.; Chen, X.; Li, W. *Chem. Soc. Rev.* **2015**, *44*, 5552–5595.
- (22) Gao, A.; Yang, X.; Tong, J.; Zhou, L.; Wang, Y.; Zhao, J.; Mao, H.; Li, T. *Biosens. Bioelectron.* **2017**, *91*, 482–488.
- (23) Tang, C. K.; Vaze, A.; Shen, M.; Rusling, J. F. *ACS Sens.* **2016**, *1*, 1036–1043.
- (24) Chen, P.; Chung, M. T.; McHugh, W.; Nidetz, R.; Li, Y.; Fu, J.; Cornell, T. T.; Shanley, T. P.; Kurabayashi, K. *ACS Nano* **2015**, *9*, 4173–4181.
- (25) Duan, L.; Yobas, L. *ACS Nano* **2018**, *12*, 7892–7900.
- (26) Hendriks, J.; Stojanovic, L.; Schasfoort, R. B. M.; Saris, D. B. F.; Kaizerman, M. *Anal. Chem.* **2018**, *90*, 6563–6571.
- (27) Kim, H.; Lee, J. U.; Song, S.; Kim, S.; Sim, S. J. *Biosens. Bioelectron.* **2018**, *101*, 96–102.
- (28) Reza, K. K.; Wang, J.; Vaidyanathan, R.; Dey, S.; Wang, Y.; Trau, M. *Small* **2017**, *13*, No. 1602902.
- (29) Ma, H.; Sun, X.; Chen, L.; Cheng, W.; Han, X. X.; Zhao, B.; He, C. *Anal. Chem.* **2017**, *89*, 8877–8883.
- (30) Lv, Y.; Zhou, Z.; Shen, Y.; Zhou, Q.; Ji, J.; Liu, S.; Zhang, Y. *ACS Sens.* **2018**, *3*, 1362–1367.
- (31) Liu, D.; Wu, F.; Zhou, C.; Shen, H.; Yuan, H.; Du, Z.; Ma, L.; Li, L. S. *Sens. Actuators, B* **2013**, *186*, 235–243.
- (32) Li, D.; Chiu, H.; Chen, J.; Zhang, H.; Chan, D. W. *Clin. Chem.* **2013**, *59*, 315–324.
- (33) Wang, Y.; Tang, L. J.; Jiang, J. H. *Anal. Chem.* **2013**, *85*, 9213–9220.
- (34) Geißler, D.; Stuffer, S.; Loehmannsroeben, H.-G.; Hildebrandt, N. *J. Am. Chem. Soc.* **2013**, *135*, 1102–1109.
- (35) Ho, S. L.; Xu, D.; Wong, M. S.; Li, H. W. *Chem. Sci.* **2016**, *7*, 2695–2700.
- (36) Li, C. Y.; Cao, D.; Qi, C. B.; Kang, Y. F.; Song, C. Y.; Xu, D. D.; Zheng, B.; Pang, D. W.; Tang, H. W. *Anal. Chem.* **2018**, *90*, 2639–2647.
- (37) Tang, L.; Casas, J. *Biosens. Bioelectron.* **2014**, *61*, 70–75.
- (38) Lim, S.; Lee, K.; Woo, H. Y.; Park, H.; Kwon, M. J. *Ann. Clin. Lab. Sci.* **2019**, *9*, 372–379.

- (39) Shi, X.; Dong, S.; Li, M.; Liu, X.; Zhang, Q.; Zhao, W.; Zong, C.; Zhang, Y.; Gai, H. *Chem. Commun.* **2015**, *51*, 2353–2356.
- (40) Shi, X.; Xie, Z.; Song, Y.; Tan, Y.; Yeung, E. S.; Gai, H. *Anal. Chem.* **2012**, *84*, 1504–1509.

# Low-Numerical Aperture Microscope Objective Boosted by Liquid-Immersed Dielectric Microspheres for Quantum Dot-Based Digital Immunoassays

Qingquan Zhang, Jiajia Li, Xiaoyan Pan, Xiaojun Liu, and Hongwei Gai\*

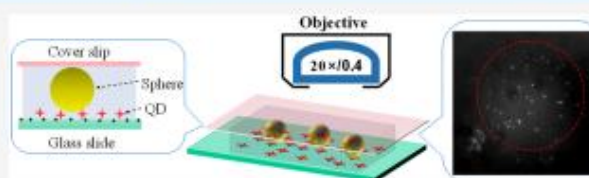
Cite This: *Anal. Chem.* 2021, 93, 12848–12853

Read Online

ACCESS |

Metrics & More

Article Recommendations



**ABSTRACT:** Quantum dot (QD)-based digital immunoassays play an important role in ultrasensitive biomarker detection. However, the requirement of an objective with a high numerical aperture (NA) limits the application of this immunoassay. Here, high-quality imaging of massive single-QDs was achieved by the combination of an air objective (20 $\times$ /0.4 NA) and liquid-immersed microspheres (150  $\mu$ m,  $n = 2.2$ ). The signal-to-noise ratio was comparable to that of a 100 $\times$ /1.4 NA oil objective. Digital analysis of prostate-specific antigen (PSA) was performed within the dynamic range of 0–50 ng/mL and a limit of detection of 0.17 ng/mL. The measured serum data from the PSA were close to the values provided by a hospital. Using a low-magnification and low-NA objective may reduce the barrier of microscopy miniaturization and is beneficial to popularize biomolecular digital analysis.

Quantum dots (QDs) are excellent fluorescent tags for labeling biomolecules, viruses, and cells.<sup>1,2</sup> Single-QD imaging technology has been proven to be effective for the high-sensitivity detection of biomarkers by a counting process.<sup>3,4</sup> Compared with conventional intensity-determined measurements, single-molecule analysis exhibits ultrahigh sensitivity and is not affected by fluctuations in intensity.<sup>5</sup> Various biomolecules, including ctDNA,<sup>6</sup> protein biomarkers, and enzymes,<sup>8</sup> have been measured accurately by counting single-QD emissions,<sup>9</sup> colocalization of QD dimers,<sup>10</sup> or single-molecule FRET signals.<sup>11</sup> To the best of our knowledge, most, if not all, single-QD counting procedures are performed using a total internal reflection fluorescence (TIRF)<sup>12</sup> or a wide-field epifluorescence microscope<sup>13</sup> equipped with an oil-immersion objective. To maximize the collected rays and achieve enough resolution, the numerical aperture (NA) of the oil-immersion objective should be higher than 1.2 (Table 1). These high-NA objectives are expensive and complex, which increases the experiment cost and sets a high barrier for application outside research laboratories.<sup>14</sup> In addition, heat conduction of oil is quick, causing a sustained observation at high temperature impossible.<sup>15</sup> Therefore, acquiring single-QD images by using a low-NA and oil-free objective is indispensable and challenging.

Dielectric colloids (DCs) are classic micro-optics elements<sup>16,17</sup> due to their high focusing ability, large commercial availability, and low cost. These elements play an important

Table 1. Review of Objectives Used in Single-QD Imaging

applications of QDs	objective	magnification	NA	refs
optical properties	oil	60 $\times$	1.4	26
	oil	100 $\times$	1.42	27
single molecule tracking	oil	60 $\times$	1.49	28
	oil	100 $\times$	1.3	29
	oil	100 $\times$	1.45	30
direct single-particle counting	oil	60 $\times$	1.49	31
	oil	60 $\times$	1.45	32
colocalization of dimers	oil	100 $\times$	1.3	33
	oil	100 $\times$	1.4	34
single-molecule FRET	oil	100 $\times$	1.4	35
	oil	100 $\times$	1.46	36
our method	air	20 $\times$	0.4	

role in the detection of single-molecule fluorescence. The fluorescence enhancing effect of DCs, which is also known as the “photonic nanojet” effect,<sup>18</sup> is ascribed to the focused

Received: June 28, 2021

Published: September 14, 2021





excitation intensity and the improved collection efficiency.<sup>19</sup> Single-molecule fluorescence-correlation spectroscopy has been measured by using a confocal fluorescence microscope with a 40 $\times$ /1.2 NA objective plus 2.0–5.0  $\mu$ m latex spheres.<sup>20</sup> The small confocal volume of colloids and the precise alignment limit the applications. Schwartz et al. obtained the images of single Cy3-labeled streptavidin or dsDNA by using a TIRF microscope with a 20 $\times$ /0.5 NA air objective plus 2.0  $\mu$ m TiO<sub>2</sub> spheres.<sup>15</sup> The field of view (FOV) of a 2  $\mu$ m sphere is too small to quantify massive molecules. The direct solution is using spheres with a larger diameter. However, the photonic nanojet effect decays drastically with the increasing particle size. From the theoretical calculations,<sup>21</sup> the proper size range of spheres is 2–9  $\mu$ m to obtain adequate intensity and resolution. To increase the detection throughput, a micro-device integrated with a large number of DCs has been fabricated to detect gold nanoparticles in flow either by backscattering or fluorescence.<sup>22</sup> The minimum detectable size is 50 nm (backscattering) or 20 nm (fluorescence), which is not adequate for a single-molecule or a single-QD. The complex microfabrication and elaborate particle assembly are also issues for practical application. To date, single-molecule quantification by using a popularly applied wide-field microscope and a low-NA objective (NA < 0.5) remains a challenge.<sup>23</sup>

Here, high-quality imaging of a single-QD was achieved by using a wide-field microscope with liquid-immersed barium titanate glass microspheres (BTGMs,  $n = 2.2$ ) and a 20 $\times$ /0.4 NA air objective. Given their large size and high refraction index, the liquid-immersed BTGMs increased the efficiency of detecting fluorescence, improved the resolution, and offered a relatively high FOV ( $\sim 100 \mu$ m), which were suitable for massive single-QD imaging. Taking prostate-specific antigen (PSA) as an example, the digital assay of a protein biomarker was realized using a low-cost and simple operation. The proposed method avoided the use of a high-NA objective (NA > 1.2), lowered the threshold of single-QD imaging, and was beneficial to popularize single-molecule research.

## EXPERIMENTAL SECTION

**Materials and Instruments.** BTGMs with different sizes (5–22, 30–100, and 145–150  $\mu$ m) were purchased from Cospheric. Polystyrene (PS) microspheres (20  $\mu$ m), *N*-hydroxysuccinimide (NHS), *N*-(3-dimethylaminopropyl)-*N*'-ethylcarbodiimide hydrochloride (EDC), and 3-aminopropyltriethoxysilane (APTES) were purchased from Sigma-Aldrich. Capture antibody (CAb), detection antibody (DAb), and prostate cancer antigen (PSA) were purchased from Shanghai Linc-Bio Science Co., Ltd. (China). Carboxyl-terminated QDs (emission, 655 nm), SuperBlock (PBS) blocking buffer, glass slides with positive charge, and coverslips were purchased from Thermo Fisher Scientific. Sylgard 184 PDMS oligomer and curing agent were from Dow Corning. Bovine serum albumin (BSA), glutaraldehyde, Tween 20, NaHCO<sub>3</sub>, and acetone were from J&K Scientific Ltd. (Beijing, China). Ultrafilters with a 3 kDa molecular weight cutoff (Amicon ultra-0.5 mL centrifugal filters) were from Millipore. Glass slides without a surface charge were obtained from Citotest Scientific Co., Ltd. (China).

A 4 in. single-sided lithography machine (H94-25C) was purchased from Sichuan Nanguang Vacuum Technology Co., Ltd. The plasma cleaner (PDC-32G-2\*) was provided by Harrick Plasma. A blade coater (MSK-AFA-ES200) was

purchased from Shen Zheng Kejing Star Technology Co., Ltd. An inverted fluorescence microscope (ECLIPSE Ti-U) was from Nikon (Japan), and a CMOS camera (Prime-95B) was from Photometrics. An LWD-CA20-PL 20 $\times$ /0.4 NA objective and UPlan-FLN 10 $\times$ /0.3 NA objective were from Olympus (Japan). A Plan-Apo-Vc 100 $\times$ /1.4 NA oil objective was from Nikon (Japan).

**QD Sedimentation and Imaging.** A PDMS membrane with a height of 2 mm was fabricated on a blade coater, and a 0.5 cm of circular hole was punched through it. The resulting PDMS membrane was attached to a glass slide with a positively charged surface to form a reservoir. Then, 20  $\mu$ L of the QD solution (50 pM) with an emission of 655 nm (QDs<sub>655</sub>) was pipetted into the reservoir and incubated for 30 min. After being washed thrice with NaHCO<sub>3</sub> (50 mM, pH 9.0) solution, the PDMS membrane was peeled off from the slide. The BTGM suspension (20  $\mu$ L) was added to the slide and sealed by a coverslip. Afterward, the QDs<sub>655</sub> was observed under a 10 $\times$ /0.3 NA or 20 $\times$ /0.4 NA objective and imaged by using a CMOS camera. For the 100 $\times$ /1.4 NA objective, 2  $\mu$ L of NaHCO<sub>3</sub> (50 mM, pH 9.0) solution, instead of the BTGM suspension, was added.

**Fabrication of the QD-Labeled DABs and PSA Immunoassay.** The QDs<sub>655</sub> solution (5  $\mu$ L, 8  $\mu$ M) was mixed with 10  $\mu$ L of NHS (5 mg/mL) and 10  $\mu$ L of EDC (5 mg/mL) solution. The mixtures were reacted at 25  $^{\circ}$ C for 25 min to activate QDs<sub>655</sub>. Then, 20  $\mu$ L of DABs (2.2  $\mu$ g/mL) were mixed with 9.2  $\mu$ L of the activated QDs<sub>655</sub> solution and incubated for 4 h at 25  $^{\circ}$ C. After centrifugation, a superblocking buffer was added to block the active sites for 30 min at 25  $^{\circ}$ C. The volume of the superblocking buffer was 4% of the total volume.

Clean glass slides were immersed in 1% (v/v) APTES solution for 30 min and washed thrice by acetone. Then, the glass slides were dried in a vacuum oven at 80  $^{\circ}$ C for 30 min and immersed in 10% (v/v) glutaraldehyde solution at 37  $^{\circ}$ C for 40 min. After several times of washing by DI water, a PDMS membrane with holes (diameter, 5 mm) was attached to the slide to form reservoirs. The CAb solution (20  $\mu$ L, 0.7  $\mu$ g/mL) was added in one reservoir and kept overnight at 4  $^{\circ}$ C. The reservoirs were blocked with 2% (w/v) BSA solution for 30 min.

The PSA solution (20  $\mu$ L) was pipetted into one reservoir and reacted at 25  $^{\circ}$ C for 1 h. After removing the reacting solution, the reservoir was washed thrice by 0.1% (v/v) Tween 20 buffer (10 mM PBS, pH 7.4). Then, 20  $\mu$ L of QD-labeled DABs (400 mM) was added and incubated at 25  $^{\circ}$ C for 1 h. Then, the reservoir was washed several times by 0.1% (v/v) Tween 20 buffer. The PDMS membrane was peeled off. The BTGM suspension (20  $\mu$ L) was added to the substrate and sealed by a coverslip. Afterward, the immunocomplexes were imaged by an inverted microscope with a 20 $\times$ /0.4 NA objective. A circular region with a diameter of 82.5  $\mu$ m was chosen at the center of a BTGM as the counting region. The number of immunocomplexes was recorded within the counting region from five or ten BTGMs.

**Serum Analysis.** Serum was diluted by PBS by 2-fold. The PSA standard was spiked in 50% (v/v) serum. The final concentrations of the spiked PSA were 0, 1, 2, 3, 4, and 5 ng/mL. Then, the PSA-spiked serum were measured by the established immunoassay procedure.



## RESULTS AND DISCUSSION

## BTGM-Boosted Fluorescence Imaging of Single QDs.

The setup of BTGM-boosted QD imaging is shown in Figure 1A. QDs were immobilized on the surface of a glass slide with

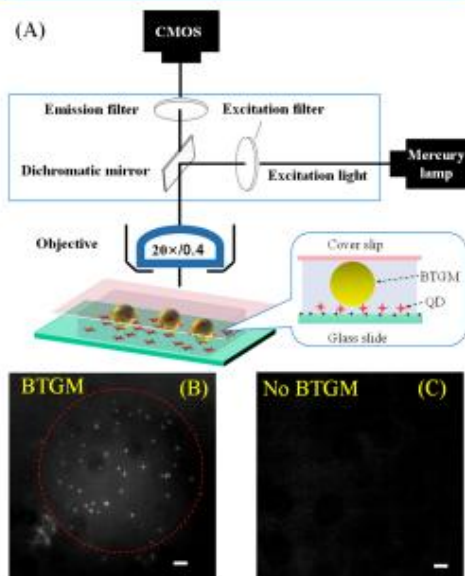


**Figure 1.** (A) Schematic of the single-QD imaging setup. Fluorescent images of QDs (emission, 655 nm) in the (B) presence or (C) absence of BTGM. Scale bars: 11  $\mu\text{m}$ .

positively-charged groups through electrostatic interaction. BTGMs were distributed above the QD layer by natural sedimentation. After sealing with a coverslip, the QDs were observed under a 20 $\times$ /0.4 NA objective and imaged by a CMOS camera. In the presence of BTGMs, bright and randomly distributed fluorescence dots were observed clearly (Figure 1B), and most dots showed a typical "blinking" phenomenon. In the absence of BTGMs, the image was dark and no fluorescent dots appeared (Figure 1C), indicating that the BTGMs played a positive role in QD imaging. The enhancement effect of BTGMs may be attributed to the following aspects: focusing of the excitation light from the mercury lamp, which intensified the QD excitation; directing the radiation of the emitter, which enhanced the collection efficiency of rays; and magnification of the virtual image, which improved the resolution.<sup>24</sup> By using printed lines with 15 and 30  $\mu\text{m}$  widths to test, we found that the bright-field images of these lines were magnified about 2-fold in the presence of BTGMs. So, the scale bars in the region of BTGMs were calibrated by using a 2-fold magnification.

The most straightforward signature of fluorescence arising from a single QD is stepwise photobleaching.<sup>25</sup> Here, the photobleaching curve of QDs was investigated using a 20 $\times$ /0.4 NA air objective combined with BTGMs (Figure 2A). The intensity of the bright fluorescent dot fluctuated in an intermittent on-off model at the first stage, and the signal

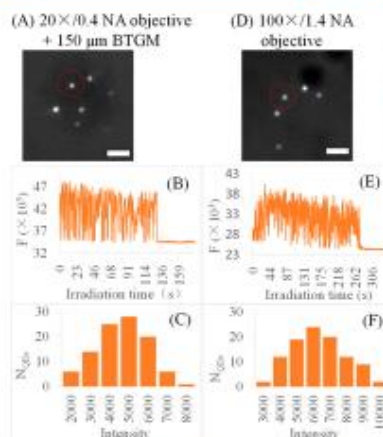


**Figure 2.** Verification of single-QD emission. (A and D) Fluorescent images of QDs. (B and E) Photobleaching curves of QDs corresponding to the dots denoted by the red-dashed box in part A and D. (C and F) Intensity distributions of 100 QDs. Scale bars: 5.5  $\mu\text{m}$  (A) and 2.2  $\mu\text{m}$  (D).

abruptly dropped to the background level after photobleaching (Figure 2B). This tendency was similar to that using a 100 $\times$ /1.4 NA oil objective alone (Figure 2D,E). The difference was that the combination of 20 $\times$ /0.4 NA objective and BTGMs accelerated the photobleaching of QD, which was due to the enhancement of the local excitation intensity. Another signature is the intensity distribution of single QD. The measured fluorescence intensity of 100 QDs displayed a typical Gaussian distribution. The peak value by using a 20 $\times$ /0.4 NA objective with BTGMs was comparable to that using a 100 $\times$ /1.4 NA oil objective. The results of the photobleaching curve and intensity distribution demonstrated that the 20 $\times$ /0.4 NA air objective could resolve the single-QD emission under the assistance of BTGM. Thus, a simple and low-cost method for single-molecule fluorescence imaging is provided. Compared with commercially available oil objectives with high NA, the combination of an air objective (20 $\times$ /0.4 NA) and liquid-immersed microspheres offers three advantages: low cost, a long working distance, and air interface. Although the removal of aberration-correction components from the high NA oil objectives may reduce the cost, we are aware that the low NA air objective is always less expensive than the high NA oil objective regardless of aberration correction. In addition, the long working distance provides a large space between the objective and sample stage and overcomes the limitation of ultrathin coverslips, both of which are helpful for the integration of more functional units in a microdevice and convenient for operation and detection.

**Optimizing the Quality of Single QD Image.** The quality of the fluorescent image is evaluated from two points, namely, the net fluorescence intensity minus the background ( $F_{\text{net}}$ ) and the FOV of single BTGM (Figure 3). Two microspheres with the same sizes but different refraction indices were used as follows: PS sphere ( $n = 1.6$ , 20  $\mu\text{m}$ ) and BTGM ( $n = 2.2$ , 20  $\mu\text{m}$ ). The calculated average  $F_{\text{net}}$  of 10 QDs was  $\sim 820$  au for the PS sphere and  $\sim 1700$  au for BTGM by using the 20 $\times$ /0.4 NA air objective (Figure 3A). The high

打开网站: <http://10.1021/acs=fig2&ref=p>

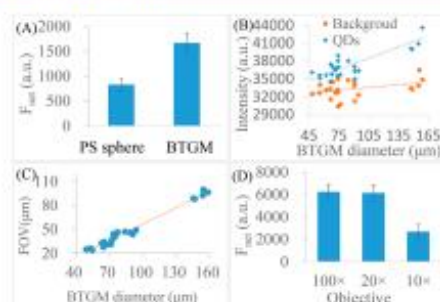


**Figure 3.** Optimization of single-QD imaging. Comparison of the (A)  $F_{\text{net}}$  of the PS spheres (20  $\mu\text{m}$ ,  $n = 1.6$ ) and BTGM (20  $\mu\text{m}$ ,  $n = 2.2$ ). Influence of the diameter of BTGM on the (B) fluorescence intensity and (C) FOV. Comparison of  $F_{\text{net}}$  using 100 $\times$ /1.4 NA objective, 20 $\times$ /0.4 NA objective with 150  $\mu\text{m}$  BTGMs, and 10 $\times$ /0.3 NA objective with 150  $\mu\text{m}$  BTGMs. Parts A, C, and D are the average data of 10 QDs.

refraction index led to a large  $F_{\text{net}}$  which was in accordance with previous reports.<sup>15</sup> The FOV of BTGM was  $\sim 14 \mu\text{m}$ , which was similar to that of the PS sphere. However, the magnifying factor of BTGM was higher than that of the PS sphere, reducing the effective imaging area.

Another affecting factor is the microsphere size. In the experiment, the BTGM size was varied in the range of 50–160  $\mu\text{m}$ . The gaps between the fluorescence of the QDs and the background showed an upward tendency with increasing BTGM size (Figure 3B). When the BTGM size exceeded 160  $\mu\text{m}$ , single-QD emission was difficult to distinguish using the 20 $\times$ /0.4 NA air objective. Meanwhile, the FOV was increased from  $\sim 30 \mu\text{m}$  to  $\sim 110 \mu\text{m}$ , proportional to the BTGM size (Figure 3C). Under the limited density of QDs, the relatively larger FOV contained more QDs in a single image, which is beneficial for data collection in digital immunoassays. In view of the FOV and  $F_{\text{net}}$ , the BTGMs applied in subsequent experiments were  $\sim 150 \mu\text{m}$  with an FOV of  $\sim 100 \mu\text{m}$ . Under the best conditions, the  $F_{\text{net}}$  ( $\sim 6100$  au) of a 20 $\times$ /0.4 NA air objective was comparable to that ( $\sim 6200$  au) of a 100 $\times$ /1.4 NA oil objective, revealing that the 20 $\times$ /0.4 NA air objective with BTGM was adequate for single-QD imaging (Figure 3D). Although the 10 $\times$ /0.3 NA air objective could differentiate most single-QD emissions from the background, the low signal-to-noise ratio may miss a portion of QDs with relatively weak emissions, and considerable information may be lost during the digital assay.

#### Digital Analysis of Cancer Related Biomarker.

Determining the expression level of disease-related biomarkers is important for cancer screening. Here, a digital immunoassay of PSA was performed using a 20 $\times$ /0.4 NA air objective with BTGMs. Figure 4A shows the process flow of a QD-based digital immunoassay, including CAb immobilization, blocking, antigen incubation, QD-labeled DAb incubation, and imaging. Compared with the commonly applied processes that use a high NA objective, the proposed method involved a simple additional step of BTGM sedimentation by gravity. The fluorescent images of immunocomplexes under 1 BTGM were captured at different PSA concentrations (Figure 4B). The fluorescent dots representing a single immunocomplex were differentiated clearly in space and increased with PSA concentration. The quantitative data of the number of QDs

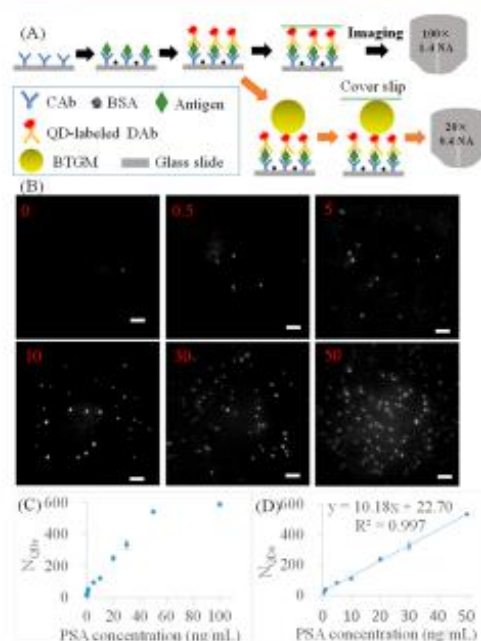


**Figure 4.** Digital analysis of PSA by using a 20 $\times$ /0.4 NA objective with 150  $\mu\text{m}$  BTGMs. (A) Immunoassay procedure. (B) Fluorescent images of single-QD under 1 BTGM with the PSA concentration varied from 0 ng/mL to 50 ng/mL. (C) Plots of  $N_{\text{QDs}}$  against PSA concentration. (D) Standard curve of PSA assay. The statistical results were calculated from five BTGMs. Scale bars, 5.5  $\mu\text{m}$ .

( $N_{\text{QDs}}$ ) were obtained by counting the fluorescent dots at the central region of five BTGMs (Figure 4C). In the range of 0–50 ng/mL,  $N_{\text{QDs}}$  displayed a good linear relationship with PSA concentration (Figure 4D). Once the PSA concentration exceeded 50 ng/mL,  $N_{\text{QDs}}$  did not increase proportionally because the capture antibodies were close to saturation. The limit of detection (LOD) of the PSA assay was 0.17 ng/mL as calculated by using the blank value plus 3 standard deviations, and this LOD was well below the clinical cutoff values. The digital analysis of PSA verified that the combination of BTGM and the 20 $\times$ /0.4 NA air objective provided a simple alternative to single-molecule fluorescence sensors, which may lower the barrier of single-molecule research.

**Clinical Serum Measurement.** The clinical serum has complex components, including ions, small molecules, proteins, and nucleic acids. For specific protein measurement in the serum, the specificity of immuno-recognition is critical. Here, AFP, CEA, SCC, BSA, and NSE were used as interfering proteins to evaluate the specificity. The concentrations of interfering proteins was set to 1.5 nM, which was 5-fold higher than the PSA concentration (0.3 nM). Following the established procedure,  $N_{\text{QDs}}$  obtained from the PSA was greatly higher than that from the interfering proteins, and the interfering signal was down to the level of the blank value (Figure 5A), both of which ensured the high specificity of PSA recognition.

Serum without any dilution has a relatively high background signal due to its complex matrix. The general method is



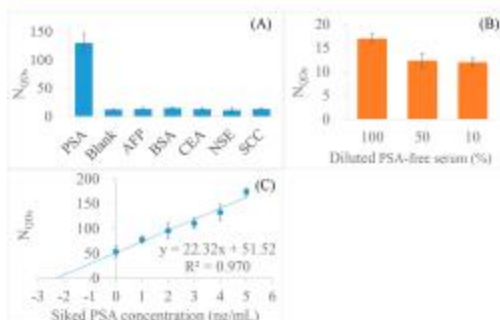


**Figure 5.** PSA assay in the clinical serum. (A) Specificity evaluation. (B) Matrix effect investigation. (C) Standard addition curve of PSA in the serum (data was from 10 BTGMs).

diluting serum with proper folds before analysis. In this study, PSA-free serum was used to determine the proper dilution factor (Figure 5B). When the PSA-free serum was diluted by 2-fold,  $N_{QDs}$  decreased by  $\sim 30\%$ . Further dilution of the PSA-free serum to 10% (v/v) led to no obvious reduction of the background signal. To reduce the background as low as possible, the sera were diluted 2-fold with PBS before the immunoassay.

Figure 5C shows the standard addition curve of the PSA measurement in 50% (v/v) serum. The PSA concentration calculated from the standard addition curve was 2.31 ng/mL, which was relatively higher than the value (1.23 ng/mL) provided by a hospital. The difference may be attributed to the distinct sources of the antibodies and deviation in the size of the BTGMs. The recoveries of the spiked PSA varied in the range of 93.7–110.5%, ensuring the accuracy of PSA measurement from another aspect.

## CONCLUSION

We demonstrated imaging of single-QD by using a  $20\times/0.4$  NA air objective plus liquid immersed microspheres ( $150\text{ }\mu\text{m}$ ,  $n = 2.2$ ). After optimization, BTGM enabled the  $20\times/0.4$  NA air objective a high signal-to-noise ratio, which was comparable to that of the  $100\times/1.4$  NA oil objective, and a relatively large FOV ( $\sim 100\text{ }\mu\text{m}$ ). These characteristics were suitable for single-QD based digital immunoassay. As an example, digital analysis of PSA was performed with a dynamic range of 0–50 ng/mL and a LOD of 0.17 ng/mL. The serum measurement data were close to the values provided by the hospital. In comparison with a high NA oil objective-based digital immunoassay, our proposed method has the potential to be miniaturized and integrated with a portable microscope and facilitates the QD counting assay, which may promote the application of digital immunoassays, especially in low-resource regions.

## AUTHOR INFORMATION

### Corresponding Author

Hongwei Gai – Jiangsu Key Laboratory of Green Synthesis for Functional Materials, School of Chemistry and Materials Science, Jiangsu Normal University, Xuzhou, Jiangsu 221116, China; [orcid.org/0000-0002-1069-9543](https://orcid.org/0000-0002-1069-9543); Email: [gai@jnu.edu.cn](mailto:gai@jnu.edu.cn); Fax: 86-516-83536972

## Authors

Qingquan Zhang – Jiangsu Key Laboratory of Green Synthesis for Functional Materials, School of Chemistry and Materials Science, Jiangsu Normal University, Xuzhou, Jiangsu 221116, China

Jiajia Li – Jiangsu Key Laboratory of Green Synthesis for Functional Materials, School of Chemistry and Materials Science, Jiangsu Normal University, Xuzhou, Jiangsu 221116, China

Xiaoyan Pan – Department of Laboratory Medicine, The Second Affiliated Hospital of Zhejiang University School of Medicine, Hangzhou 310009, China

Xiaojun Liu – Jiangsu Key Laboratory of Green Synthesis for Functional Materials, School of Chemistry and Materials Science, Jiangsu Normal University, Xuzhou, Jiangsu 221116, China

Complete contact information is available at:

<https://pubs.acs.org/10.1021/acs.analchem.1c02709>

## Author Contributions

H. Gai and Q. Zhang conceived of the idea and wrote the manuscript. J. Li and X. Pan carried out the experiments. X. Liu developed the immunoassay analysis.

## Notes

The authors declare no competing financial interest.

## ACKNOWLEDGMENTS

We thank the support from the Natural Science Foundation of China (NSFC Grant 22174056) and Xuzhou Key Plan of R&D (Grant KC20170).

## REFERENCES

- Wegner, K. D.; Hildebrandt, N. *Chem. Soc. Rev.* **2015**, *44*, 4792–4834.
- Jin, D.; Xi, P.; Wang, B.; Zhang, L.; Enderlein, J.; van Oijen, A. M. *Nat. Methods* **2018**, *15*, 415–423.
- Hu, J.; Wang, Z. Y.; Li, C. C.; Zhang, C. Y. *Chem. Commun.* **2017**, *53*, 13284–13295.
- Long, Y.; Zhang, L. F.; Zhang, Y.; Zhang, C. Y. *Anal. Chem.* **2012**, *84*, 8846–8852.
- Liu, X.; Zhang, Y.; Liang, A.; Ding, H.; Gai, H. *Chem. Commun.* **2019**, *55*, 11442–11445.
- Liu, X.; Wu, Z.; Lin, X.; Bu, W.; Qin, L.; Gai, H. *Analyst* **2021**, *146*, 3034–3040.
- Liu, X.; Sun, Y.; Lin, X.; Pan, X.; Wu, Z.; Gai, H. *Anal. Chem.* **2021**, *93*, 3089–3095.
- Zhang, H.; Zhang, K.; Yao, Y.; Liu, Y.; Ji, J.; Huang, X.; Liu, J.; Liu, B. *Anal. Chem.* **2019**, *91*, 9500–9507.
- Jiang, D.; Zhang, Q.; Shen, X.; Wang, L.; Jiang, W. *Talanta* **2010**, *82*, 1003–1009.
- Tao, G.; Lai, T.; Xu, X.; Ma, Y.; Wu, X.; Pei, X.; Liu, F.; Li, N. *Anal. Chem.* **2020**, *92*, 3697–3706.
- Li, C.-C.; Li, Y.; Zhang, Y.; Zhang, C.-y. *TrAC, Trends Anal. Chem.* **2020**, *122*, 115753.
- Jiang, D.; Wang, L.; Jiang, W. *Anal. Chim. Acta* **2009**, *634*, 83–88.
- Liu, X.; Huang, C.; Dong, X.; Liang, A.; Zhang, Y.; Zhang, Q.; Wang, Q.; Gai, H. *Chem. Commun.* **2018**, *54*, 13103–13106.
- Gbenuche, P.; de Torres, J.; Ferrand, P.; Wenger, J. *Appl. Phys. Lett.* **2014**, *105*, 131102.
- Schwartz, J. J.; Stavrakis, S.; Quake, S. R. *Nat. Nanotechnol.* **2010**, *5*, 127–132.
- Guo, M.; Ye, Y.-H.; Hou, J.; Du, B. *Photonics Res.* **2015**, *3*, 339.
- Ye, R.; Ye, Y.-H.; Ma, H. F.; Ma, J.; Wang, B.; Yao, J.; Liu, S.; Cao, L.; Xu, H.; Zhang, J.-Y. *Opt. Lett.* **2013**, *38*, 1829–1831.

- (18) Yang, S.; Taflove, A.; Backman, V. *Opt. Express* **2011**, *19*, 7084–7093.
- (19) Gérard, D.; Devilez, A.; Aouani, H.; Stout, B.; Bonod, N.; Wenger, J.; Popov, E.; Rigneault, H. *J. Opt. Soc. Am. B* **2009**, *26*, 1473–1478.
- (20) Gérard, D.; Wenger, J.; Devilez, A.; Gachet, D.; Stout, B.; Bonod, N.; Popov, E.; Rigneault, H. *Opt. Express* **2008**, *16*, 15297–15303.
- (21) Wang, Z.; Guo, W.; Li, L.; Luk'yanchuk, B.; Khan, A.; Liu, Z.; Chen, Z.; Hong, M. *Nat. Commun.* **2011**, *2*, 218.
- (22) Yang, H.; Cornaglia, M.; Gijss, M. A. *Nano Lett.* **2015**, *15*, 1730–1735.
- (23) Wenger, J.; Gérard, D.; Aouani, H.; Rigneault, H. *Anal. Chem.* **2008**, *80*, 6800–6804.
- (24) Darafsheh, A.; Walsh, G. F.; Dal Negro, L.; Astratov, V. N. *Appl. Phys. Lett.* **2012**, *101*, 141128.
- (25) van den Wildenberg, S. M. J. L.; Prevo, B.; Peterman, E. J. G. A Brief Introduction to Single-Molecule Fluorescence Methods. In *Single Molecule Analysis: Methods in Molecular Biology*, Vol. 783; Humana Press: Totowa, NJ, 2011; pp 81–99.
- (26) Yu, X. X.; Li, J. N.; Kwok, K. C.; Paa, M. C.; Choi, M. M. F.; Shiu, K. K.; Chen, J. Y.; Cheung, N. H. *J. Phys. Chem. C* **2012**, *116*, 18479–18486.
- (27) Jauffred, L.; Richardson, A. C.; Oddershede, L. B. *Nano Lett.* **2008**, *8*, 3376–3380.
- (28) Urban, J. M.; Chiang, W.; Hammond, J. W.; Cogan, N. M. B.; Litzburg, A.; Burke, R.; Stern, H. A.; Gelbard, H. A.; Nilsson, B. L.; Krauss, T. D. *J. Phys. Chem. B* **2021**, *125*, 2566–2576.
- (29) Sarkar, S.; Le, P.; Geng, J.; Liu, Y.; Han, Z.; Zahid, M. U.; Nall, D.; Youn, Y.; Selvin, P. R.; Smith, A. M. *J. Am. Chem. Soc.* **2020**, *142*, 3449–3462.
- (30) Le, P.; Vaidya, R.; Smith, L. D.; Han, Z.; Zahid, M. U.; Winter, J.; Sarkar, S.; Chung, H. J.; Perez-Pinera, P.; Selvin, P. R.; Smith, A. M. *ACS Nano* **2020**, *14*, 8343–8358.
- (31) Palacios, M. A.; Lacy, M. M.; Schubert, S. M.; Manesse, M.; Walt, D. R. *Anal. Chem.* **2013**, *85*, 6639–6645.
- (32) Li, L.; Qu, X.; Sun, J.; Yang, M.; Song, B.; Shao, Q.; Zhang, X.; Jin, W. *Biosens. Bioelectron.* **2011**, *26*, 3688–3691.
- (33) Ho, Y.-P.; Kung, M. C.; Yang, S.; Wang, T.-H. *Nano Lett.* **2005**, *5*, 1693–1697.
- (34) Liu, X.; Huang, C.; Zong, C.; Liang, A.; Wu, Z.; Zhang, Y.; Zhang, Q.; Zhao, W.; Gai, H. *ACS sensors* **2018**, *3*, 2644–2650.
- (35) Zhang, C.-Y.; Johnson, L. W. *Anal. Chem.* **2006**, *78*, 5532–5537.
- (36) Lu, J.; Zong, S.; Wang, Z.; Chen, C.; Zhang, Y.; Wang, H.; Cui, Y. *ACS omega* **2021**, *6*, 8808–8815.



# Multiplexed Homogeneous Immunoassay Based on Counting Single Immunocomplexes together with Dark-Field and Fluorescence Microscopy

Xiaojun Liu,<sup>§</sup> Xinyi Lin,<sup>§</sup> Xiaoyan Pan, and Hongwei Gai\*

Cite This: *Anal. Chem.* 2022, 94, 5830–5837

Read Online

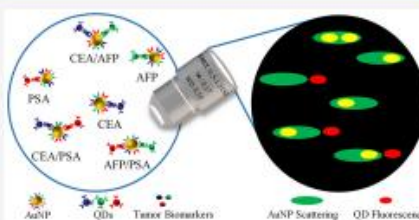
ACCESS |

Metrics & More

Article Recommendations

Supporting Information

**ABSTRACT:** The development of multiplexed immunoassays is impeded by the difficulty in distinguishing labeled immunocomplexes from free probes and nonspecifically bound probes. Here, we attempted to overcome this issue by counting core–satellite-structured immunocomplexes simultaneously using dark-field and fluorescence microscopy. The tumor biomarkers of carcinoembryonic antigen (CEA),  $\alpha$ -fetoprotein (AFP), and prostate-specific antigen (PSA) were chosen as model targets. Gold nanoparticles (AuNPs) with diameters of 70 nm were coated with the detection antibodies of the three targets. Quantum dot (QD) S25, QD S85, and QD 655 were modified with the capture antibodies of CEA, AFP, and PSA, respectively. Then, an immunocomplex containing one AuNP and one or several QDs was formed, whereas free and nonspecifically bound probes had either one AuNP or one QD. When observed with a transmission grating-based spectral microscope, the immunocomplexes had overlapping scattering and fluorescent spectral images and were therefore identified and quantified precisely. The biomarkers inside the immunocomplexes were recognized on the basis of the fluorescent first-order streaks of the QDs. Model biomarkers in buffer and in 12.6% blank plasma were quantified for validation. The limits of detection for CEA, PSA, and AFP in buffer were in dozens of femtomolar and were close to those in blank plasma. The results demonstrated that our approach worked well in distinguishing immunocomplexes from free and nonspecifically bound probes. The successful quantification of the three targets in five human plasma samples verified the reliability of our method in clinical applications.



## INTRODUCTION

Compared with a single biomarker, a panel of protein biomarkers offers a more informative snapshot of disease status<sup>1</sup> and is thus more valuable for physician diagnostics. Multiplexed immunoassays increase measurement precision and reduce sample and reagent consumption, measurement time, and cost per test. Therefore, developing multiplexed immunoassays with adequate sensitivity and specificity for clinical practice is urgently required.

Multiplexed immunoassays can be grouped into heterogeneous and homogeneous immunoassays depending on the need for a separation process. In heterogeneous multiplexed immunoassays, two dominant modes have been developed to identify multiple target molecules: address encoding<sup>2,3</sup> and target encoding.<sup>4,5</sup> In address encoding, each immunocomplex is preassigned a given zone on a sensor and identified on the basis of the position of the generated signal. Typical examples of address encoding are planar microarray-based immunoassays. In target encoding, each kind of immunocomplex is correspondingly labeled with a tag, which is usually either an optical or electrochemical tag. Although heterogeneous multiplexed immunoassays have presented impressive perform-

ance, they are restricted by stringent multiple washing steps that are needed to remove free probes. These multiple washing steps deteriorate antibody–antigen binding and lead to the loss of immunocomplexes. Correspondingly, reproducibility worsens, cumulative error increases, and analytical sensitivity is compromised.

Washing-free homogeneous multiplexed immunoassays have been developed to address the above issues. However, distinguishing immunocomplexes (detection probes bound to the targets) from free probes is a challenge because the tags inside the immunocomplexes and the tags in the unbound detection probes exhibit the same characteristics unless a particular design is used. To date, three strategies have been established to distinguish multiple bound probes from unbound probes without separation: (1) The immunocomplex

Received: December 6, 2021

Accepted: March 24, 2022

Published: April 5, 2022



is captured online, and the signal of the immunocomplex is remarkably higher than that of the unbound detection probe.<sup>6</sup> A core–satellite-structured immunocomplex of a polystyrene bead and multiple upconversion nanoparticle probes was trapped onto the detection plane using holographic optical tweezers, and carcinoembryonic antigen (CEA) and  $\alpha$ -fetoprotein (AFP) were quantified on the basis of the fluorescence intensity of their respective probes. (2) The tag characteristic is obviously changed by target binding. Some special phenomena have been adopted for this purpose. These phenomena include SERS enhancement caused by noble metal nanoparticle plasmonic coupling,<sup>7</sup> Förster resonance energy transfer between fluorescent tags,<sup>8–10</sup> and the localized surface plasmon resonance peak shift of noble metal nanoparticles induced by the change in the surrounding matrix.<sup>11</sup> (3) Immunocomplexes containing the aggregated detection probe are directly distinguished from single, dispersed detection probes via single-particle detection.<sup>12</sup> In this research, the immunocomplex induced by CEA contained quantum dot (QD) 655 and QD 585 and was distinguished on the basis of the unique spectral patterns of dual-colored QD aggregates. Immunocomplexes induced by AFP contained the QD 585 aggregate and were identified on the basis of the spectral blue shift pattern of same-colored QD aggregates.

The random nonspecific binding of detection probes is another issue that limits all immunoassays. In particular, sensing performance is greatly damaged when target abundance is extremely low such that the target's signal is comparable with background signals or noise. Very recently, a study reported a kinetic fingerprinting approach for directly filtering out nonspecific binding for single-plexed immunoassays.<sup>13</sup> In this approach, a high-affinity antibody and a low-affinity fluorescent antibody fragment (Fab) were used as the capture probe and the detection probe, respectively. The specific binding of the Fab to a single target adsorbed onto a cover glass slip was transient and reversible, thus yielding a temporal pattern of repetitive binding–dissociation events. By contrast, Fab-nonspecific binding resulted in few binding–dissociation events at the same location. Fab-specific binding was judged on the basis of the number of binding–dissociation events and the median dwell time in the probe-bound state. Similarly, an approach based on single-particle motion trajectory analysis was developed to identify specifically bound probes.<sup>14</sup> It works by capturing the target on magnetic beads, pulling the target–bead complexes into fL-sized reaction cells modified with antibodies with the aid of a magnet, capturing the target–bead complexes on the bottom of the cells, and monitoring each bead. The specifically bound beads showed characteristic Brownian motion, which is distinct from the motions of the beads in free diffusion and nonspecifically bound beads.

In our previous research of homogeneous immunoassays, we found that the nonspecific binding to the probes of 2 two-colored quantum dots (QDs) dramatically dropped when compared to that of two same-colored QD probes.<sup>12</sup> It might be that the difference in the two-colored QD surface resulted in fewer proteins that could simultaneously nonspecifically bind to the QDs. Inspired by this finding, we attempted to further inhibit the nonspecific binding with gold nanoparticles (AuNPs) and QDs, whose surfaces were hugely different. AuNPs coated with the detection antibodies of three targets were used as scattering probes, and three QDs each of which was modified with the capture antibody of one target were

used as fluorescent probes. When targets were present, the AuNPs bound with the QDs. An immunocomplex, therefore, had one scattering probe and one or several fluorescent probes, whereas a free probe and a probe (both were referred to as unbound probes) that had adsorbed nonspecific interference had either a scattering probe or a fluorescent probe. When observed under a transmission grating-based spectral microscope, the immunocomplex was distinguishable from the unbound probe by its overlapping scattering and fluorescent spectral images. Meanwhile, the biomarker was identified on the basis of the first-order streak of a single QD. As proof of this concept, CEA, AFP, and prostate-specific antigen (PSA) in PBS buffer and in 12.6% blank plasma were quantified. In PBS buffer, the limits of detection (LODs) for CEA, PSA, and AFP were estimated as 30, 50, and 10 fM, respectively. In 12.6% blank plasma, the LODs for CEA, PSA, and AFP were 100, 60, and 20 fM, respectively. The LOD values in PBS buffer were close to those in blank plasma, indicating that our approach worked well for recognizing specifically bound probes. The successful quantification of CEA, PSA, and AFP in five human plasma samples demonstrated the reliability of our method in clinical applications.

## ■ EXPERIMENTAL SECTION

**Chemicals and Materials.** Fluorescent beads with diameters of 2.19  $\mu$ m were purchased from Bangs Laboratories, Inc. (IN). Concentrated AuNPs with diameters of 70, 65, 60, and 55 nm were bought from Nanopartz (CO). Carboxylic QD 525, carboxylic QD 585, carboxylic QD 655, SuperBlock buffer, PBS buffer (pH 7.2), positively charged glass slides, and glass coverslips were purchased from Thermo Fisher Scientific (MA). CEA, AFP, PSA, and their corresponding detection and capture antibodies were acquired from Shanghai Linc-Bio Science Co. Ltd. (Shanghai, China). Single-stranded DNA sequences were customized by Shanghai Sangon Bioengineering Limited Company (Shanghai, China). The sequences of DNA u1 and DNA u2 were HOOC–CCGAGC–SH (5' to 3') and GCTTGCGG (5' to 3'), respectively. Bovine serum albumin (BSA), neuron-specific enolase, and N-(3-(dimethylamino)propyl)-N-ethylcarbodiimide hydrochloride (EDC) were procured from Sigma-Aldrich (MO). An ultrafiltration tube with a molecular weight cutoff of 3 kDa was purchased from Millipore. A size-exclusion column (5/150 SuperoseTM 6 Increase) was obtained from GE Healthcare Life Sciences (PA). Transmission grating (70 lines/mm) was purchased from Edmund Scientific (NJ). Other materials were purchased from local vendors.

**Instrument.** The study involved the following equipment: a Nikon Ti-U microscope (Japan), a Prime-95B CMOS camera from Photometrics Technology (Canada), a 1260 Infinity HPLC from Agilent Technology, an F-4600 fluorescence spectrophotometer from HITACHI (Japan), a Vortex-5 mixer from Thermo Fisher, and a Sorvall legend micro 17R centrifuge from Thermo Fisher.

**Clinical Sample.** The clinical samples were provided by the Second Affiliated Hospital of Zhejiang University Hospital. Each subject signed a written informed consent form. All of the samples were treated in accordance with the procedure from the Institutional Review Board of Jiangsu Normal University.

**Fluorescent Probe Preparation.** The fluorescent probes included CEA capture antibody-modified QD 525, AFP capture antibody-modified QD 585, and PSA capture antibody-modified QD 655. The details of the probe preparation



are as follows with CEA capture antibody-modified QD 525 as an example. In brief, a 2.5  $\mu\text{L}$  aliquot of QD 525 was mixed with 5.0  $\mu\text{L}$  of 5.0 mg/mL EDC (freshly prepared). The mixture was rotated for 25.0 min to activate the carboxylic groups of QD 525. The conjugation of the antibody with the activated QD 525 was finished by rotating the mixture of 10.0  $\mu\text{L}$  of QD 525 and 20.0  $\mu\text{L}$  of the antibody (2.4 mg/mL) in the dark for 4 h. The probe was purified with a 1260 Infinity HPLC equipped with a 5/150 SuperoseTM 6 Increase column. The mobile phase was 50 mM  $\text{NaHCO}_3$  (pH 9.0). The flow rate, injection volume, and detection wavelength were set as 0.3 mL/min, 13  $\mu\text{L}$ , and 224 nm, respectively. As shown in Figure S1, the probes were well separated from the antibodies and QDs. The probes were collected and stored at 4  $^\circ\text{C}$ . Prior to use, the probes were mixed with SuperBlock buffer at a ratio of 20:1, rotated in the dark for 30 min, and quantified on the basis of QD 525 fluorescence intensity in accordance with the equation  $y = 306.17x + 157.33$ . The equations used for the QD 585 and QD 655 probes were  $y = 1417.3x - 522.77$  and  $y = 709.43x - 97.024$ , respectively.

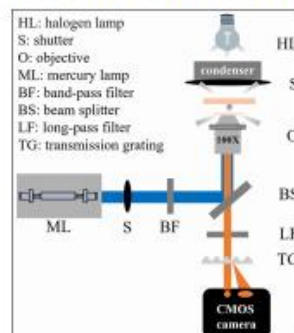
**Scattering Probe Preparation.** AuNPs coated with the detection antibodies of CEA, AFP, and PSA were designed as the scattering probe. The coating process included two steps: the modification of AuNPs with dsDNA and the linkage of the detection antibodies to the immobilized DNA. The AuNPs were modified with dsDNA in accordance with the procedure described by Liu et al.<sup>15</sup> In brief, 447.5  $\mu\text{L}$  of 2.4  $\mu\text{M}$  DNA u1, 165.4  $\mu\text{L}$  of 6.5  $\mu\text{M}$  DNA u2, and 50  $\mu\text{L}$  of AuNPs were mixed well. After the addition of 25.9  $\mu\text{L}$  of 4.0 M NaCl and 28.2  $\mu\text{L}$  of PBS, the mixture was immediately placed in a freezer at  $-20$   $^\circ\text{C}$  and kept overnight. After thawing at room temperature, excessive dsDNA was removed through centrifugation twice at 13 000 rpm and 18  $^\circ\text{C}$ . The dsDNA-modified AuNPs were mixed with 2.0  $\mu\text{L}$  of 10 mg/mL EDC and rotated for 20 min at room temperature to activate the carboxylic groups. The AuNPs were then washed and resuspended with 155 mM NaCl and subsequently mixed with the detection antibodies of CEA, AFP, PSA, and BSA at the ratios of 1:32:32:386. The conjugation of the antibodies with the dsDNA took 3 h and then was terminated with 4.0 mM Tris buffer. The antibody-modified AuNPs were purified through sequential centrifugation processes: one at 13 000 rpm and another at 2500 rpm. The AuNP probes were quantified in accordance with the absorbance intensity (extinction coefficient:  $3.64 \times 10^{10} \text{ M}^{-1} \text{ cm}^{-1}$ ).

**Immunoreaction.** Immunoreaction assays were conducted in two media, namely, PBS buffer and blank plasma. The procedure is detailed below with the immunoreaction in PBS buffer as an example. AFP, CEA, and PSA were dissolved in PBS buffer separately to prepare a series of standard solutions with various concentrations. The three QD probes, the AuNP probe, 5.0  $\mu\text{L}$  of the AFP standard solution, 5.0  $\mu\text{L}$  of the CEA standard solution, and 5.0  $\mu\text{L}$  of the PSA standard solution were mixed, and the mixture was filled up to 50.0  $\mu\text{L}$  with PBS buffer. The concentrations of the QD 525, QD 585, QD 655, and AuNP probes were 80.0, 60.0, 60.0, and 4.0 pM, respectively. After rotation for 2 h in the dark, the immunoreaction solution was immediately diluted three times and used to prepare microscopy specimens. The immunoreaction in blank plasma was conducted in a way similar to that in PBS buffer except that 6.3  $\mu\text{L}$  of blank plasma was added to the immunoreaction solution. Note that the blank plasma was the plasma fraction without AFP, PSA, and

CEA. The blank plasma was obtained by filtering 10 plasma samples with a centrifugal ultrafiltration tube with a molecular weight cutoff of 3.0 kDa. Each immunoreaction was repeated three times.

**Spectral Scattering Image and Fluorescent Image of Immunoreaction Solution.** An inverted microscope equipped with a dark-field model and fluorescent model was used to take the spectral scattering image and the fluorescent image of an immunoreaction solution. As shown in Scheme 1, the dark-

**Scheme 1.** Inverted Single-Particle (Spectral) Microscope with Switchable Dark-Field and Fluorescent Modes



field model and the fluorescent model shared one common emission optical path and had the respective excitation optical paths. Therefore, the dark-field model and the fluorescent model could be switchable simply by controlling the excitation optical path shutter. A detachable transmission grating was inserted before the CMOS camera to capture spectral images. A beam from an emitter was divided into two by the transmission grating. One was in the original transmission direction and referred to as a zeroth-order dot. Another was away from the original direction and referred to as the first-order streak. The wavelength of the emitter is determined by the equation:  $\lambda = d1 \times Cs/d2$ , where  $d2$ ,  $Cs$ , and  $d1$  are the distance between the transmission grating and the CMOS, the grating constant, and the distance between the zeroth-order dot and the corresponding first-order streak (dot-streak distance), respectively.

A microscopy specimen was prepared as follows: 2.2  $\mu\text{L}$  of an immunoreaction solution was dropped onto a positively charged slide. A slip was placed on the drop immediately, and the slide and slip were sealed with nail-polishing oil. The specimen was ready for spectral image acquisition after being allowed to stand for some time. Note that the particle concentration was below 0.10 nM, a prerequisite for single-particle spectral imaging. A total of 17 sites of the specimen were randomly selected and imaged sequentially with the dark-field and fluorescent modes.

**Image Analysis.** Images were analyzed using ImageJ software. The scattering and fluorescent images of a solution were colored in green and in red, respectively, and then merged. In the spectral image, a zeroth-order dot was matched with its first-order streak on the basis of position. In our previous studies, this approach is a common method for

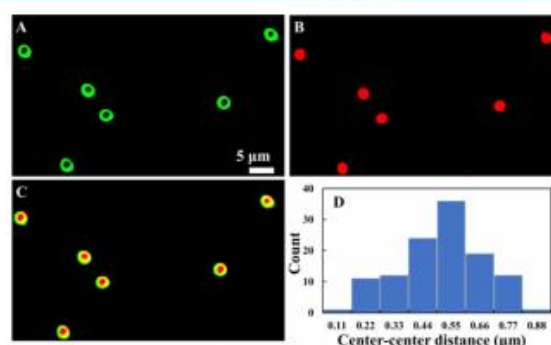
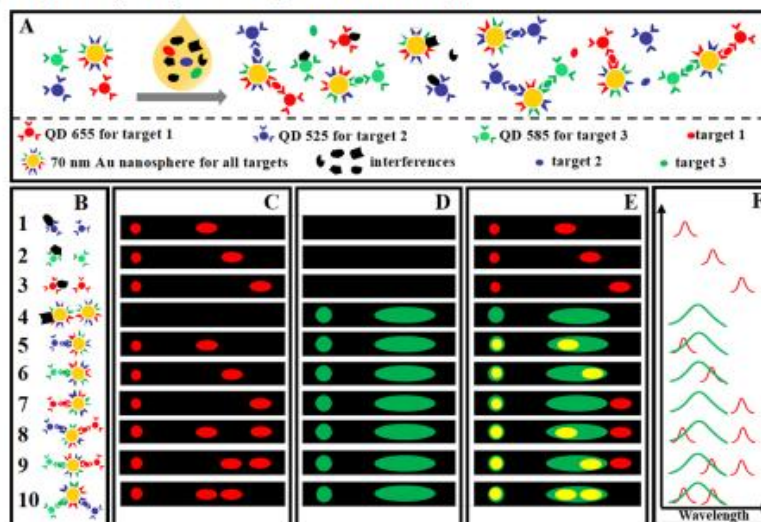


Figure 1. (A) Bead scattering image colored in green; (B) bead fluorescent image colored in red; (C) merged image; and (D) center-center distance distribution of randomly selected beads.

Scheme 2. Schematic of the Proposed Principle of the Multiplexed Immunoassay: (A) Three-Plexed, Homogeneous Immunoreaction; (B) Possible Probes in the Immunoreaction; (C) Corresponding Fluorescent Spectral Patterns Colored in Red; (D) Corresponding Scattering Spectral Patterns Colored in Green; (E) Corresponding Merged Images (C) and (D) Pictures; and (F) Corresponding Converted Spectra from the Panel (E)



judging the origin of the zeroth-order dot and the first-order streak. In brief, when a curve drawn by connecting the dots was similar to the one linking the streaks, the dot and streaks in the same positions were paired. In the merged spectral image of an immunoreaction solution, the yellow zeroth-order dots and the green zeroth-order dots were counted. The QDs inside a yellow zeroth-order dot were identified on the basis of the dot-streak distance and counted. The distance distributions of the three QDs did not overlap with each other (Figure S2). Note that the zeroth-order dot (the first-order streak) with a streak (dot) that was not in the same image was not counted.

The images of 12 randomly selected sites on each specimen were processed through the above method.

**Clinical Sample Test.** The responses of our probes to five clinical samples and their aliquots spiked with the three targets were measured using our approach. The immunoreaction conditions for the samples were similar to those in PBS buffer, except that the standard solutions of the targets were replaced with 6.25  $\mu\text{L}$  of the clinical samples.



## RESULTS AND DISCUSSION

**Overlap between the Scattering and Fluorescent Images of Single Particles.** Fluorescent beads with scattering activity were used to investigate the overlap between the scattering and fluorescent images of single particles. The beads were sequentially imaged in dark-field and fluorescent modes (Scheme 1). The scattering and fluorescent images were indicated by green and red colors (Figure 1A,B), respectively, and merged in Figure 1C (subsequent images were processed in the same way). The bead was in the shape of a dot and a ring in the fluorescent and scattering images, respectively. The morphological difference of the bead between the two images was attributed to the difference in distribution between the scattering and fluorescent compositions. In the merged image, a yellow ring was surrounded by a thin annulus in green, and the size of the yellow ring was almost identical to that of the ring in the scattering image. These changes indicated that the overwhelming majority of the scattering image of the bead was trapped in the fluorescent image. The distance between the center of the scattering image and that of the fluorescent image (center–center distance) was used to further assess the overlap. The center–center distance was calculated using the center coordinates of the fluorescent and scattering images that were obtained from the contour map generated by MATLAB software. Figure 1D presents the center–center distance distribution of randomly selected beads. The median of the distance was measured as 0.55  $\mu\text{m}$ . The small center–center distance implied that with our microscopy setup, the fluorescent image of a particle overlapped with the scattering image perfectly.

**Principle of the Proposed Method.** AuNPs with a diameter of 70 nm and three QDs (QD 525, QD 585, and QD 655) were used as the scattering and fluorescent tags, respectively. The three QDs were selected because their fluorescence spectra did not overlap with each other (Figure S2). As shown in Scheme 2A, the AuNP probes were coated with the detection antibodies of the three targets, and a specific QD probe was modified with the capture antibodies of a specific target. An immunocomplex induced by targets contained two kinds of tags, whereas unbound probes in forms of the free probes and the probes coated with interference had only one kind of tag. Scheme 2B presents all of the possible probes in the immunoreaction. Rows 1–4 display the unbound probes. Rows 5–7 show the immunocomplexes that were composed of one AuNP and one QD. Rows 8–10 present the immunocomplexes with one AuNP and two QDs. Immunocomplexes with one AuNP and more than two QDs and those with one AuNP and two same-colored QDs were not observed in our experiments (see details in the Supporting Information). The spectral images of single QDs or single AuNPs can be obtained using a transmission grating-based spectral microscope. Detailed explanations for the spectral image have been reported in our previous publications.<sup>16–22</sup> Their corresponding fluorescent spectral images, which were colored in red, and their scattering spectral images, which were colored in green, are depicted in Scheme 2C,D, respectively. Images in Scheme 2C,D are merged in 2E. The spectral image of a particle is composed of one zeroth-order spot and one first-order streak, which can be converted into its spectrum as shown in Scheme 2F. The scattering zeroth-order dot of an immunocomplex overlapped with its fluorescent zeroth-order dot. The reasons are given in the

Supporting Information. The overlapping regions of the fluorescent and scattering images turned yellow. Obviously, the immunocomplexes were distinguishable from the unbound probes as yellow dots. The fluorescent streaks of QD 525 and QD 585 were packed whole into the left and the right of the scattering streak of the AuNP, respectively. The fluorescent streak of QD 655 was adjacent to the right of the AuNP scattering streak. Therefore, for an immunocomplex with QD 525 (QD 585), the red fluorescent streak was “trapped” in the left (right) part of the green scattering streak, yielding the overlapping region in yellow. For an immunocomplex with QD 655, the red fluorescent streak was adjacent to the right part of the green scattering streak. Therefore, the interiors of the immunocomplexed QD 525 and QD 585 were identified on the basis of the yellow streak’s position, and QD 655 was characterized by the red fluorescent streak adjacent to the right of the green scattering streak. In summary, two steps were needed to identify targets in the merged image. The first step was to distinguish the immunocomplexes from free probes and nonspecifically bound probes on the basis of the presence of yellow dots. The second step was to identify QDs in an immunocomplex on the basis of the first-order streaks. If the scattering streak of an immunocomplex was partially yellow, the yellow on the left and on the right indicated the presence of QD 525 and QD 585, respectively; if not, the immunocomplex fluorescent streak adjacent to its scattering streak would be observed, indicating the presence of QD 655.

QD 525, QD 585, and QD 655 were coated with the capture antibodies of CEA, AFP, and PSA, respectively, to demonstrate the principle of our method. The AuNPs were coated with the detection antibodies of the three proteins. The ensemble fluorescence intensity of the QD probes did not obviously decrease after immunoreaction (Figure S3), therefore excluding the remarkable quenching of the fluorescent probes caused by the scattering probes in proximity. The merged spectral patterns of the immunoreaction solution with antigens and the control solution without antigens are displayed in Figure 2A,B. The dot and the streak originating from the same single particle were paired in accordance with their positions.<sup>20–22</sup> The zeroth-order dot and the first-order streak from an individual AuNP were labeled with triangles in the same color. For example, at the top of Figure 2A, the spot and streak labeled with yellow triangles were from the same AuNP. The

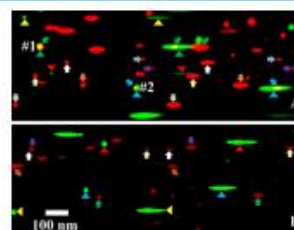
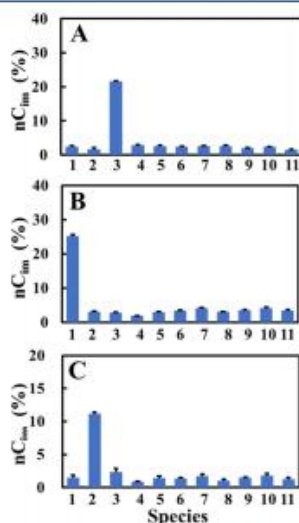


Figure 2. Typical spectral images of probes with (A) and without (B) targets merging the scattering image in green and the fluorescent image in red. The zeroth-order dot and the first-order streak from an individual AuNP are labeled with triangles in the same color. The zeroth-order dot and the first-order streak from an individual QD (QD aggregate) are labeled with arrows in the same color. The scale bar shows wavelength rather than physical size.



zeroth-order dot and the first-order streak from a QD or QD aggregate were labeled with arrows in the same color. In Figure 2B, as expected, the zeroth-order dots were either green or red without the targets. The appearance of the yellow zeroth-order dots in the presence of the targets indicated the presence of immunocomplexes in Figure 2A. For immunocomplex #1, the yellow streak was on the left of the scattering streak, and a fluorescent streak was adjacent to the right of the scattering streak, indicating the presence of CEA and PSA as depicted above. For immunocomplex #2, the location of the yellow streak on the right of the scattering streak implied the presence of AFP. The results verified that CEA, PSA, and AFP could be simultaneously detected using our method.

**Cross-Reactivity and Selectivity.** Under the optimized conditions (Figure S3), cross-reactivity among the three targets was evaluated by comparing the response of the probes to the solutions containing only the single target as shown in Figure 3. The response was weighed on the basis of the normalized



**Figure 3.** Cross-reactivity and selectivity. (A) Response of the probe for AFP to possible interference, (B) response of the probe for PSA to possible interference, and (C) response of the probe for CEA to possible interference. 1–11 represent PSA, CEA, AFP, PBS, blank plasma, proteins, anions, cations, carbohydrates, amino acids, and DNA sequences, respectively. Proteins: bovine serum albumin and neuron-specific enolase; anions:  $\text{Cl}^-$ ,  $\text{SO}_4^{2-}$ ,  $\text{CO}_3^{2-}$ ,  $\text{HCO}_3^-$ , and  $\text{SO}_3^{2-}$ ; cations:  $\text{K}^+$ ,  $\text{Na}^+$ ,  $\text{Ca}^{2+}$ ,  $\text{Fe}^{2+}$ , and  $\text{Cu}^{2+}$ ; carbohydrates: glucose,  $\alpha$ -mannose,  $\alpha$ -fructose,  $\beta$ -lactose; amino acids: phenylalanine, threonine, lysine, leucine, tryptophan, and valine; DNA sequences: (A)20CGCTCCTCG and (A)20CGCTCCTCGAAGC.

counts of the immunocomplexes. This normalized immunocomplex count was calculated in accordance with the equation  $nC_{im} = C_{im}/C_{Au}$ , where  $nC_{im}$ ,  $C_{im}$ , and  $C_{Au}$  represent the normalized count of the immunocomplexes, the count of the immunocomplexes, and the count of the AuNPs, respectively. For the AFP probes (Figure 3A), the  $nC_{im}$  value of AFP was

considerably higher than that of the noncorresponding targets at the same concentrations, and the  $nC_{im}$  values of the noncorresponding targets were close to those of PBS. The same trends were observed for the probes for CEA and PSA (Figure 3B,C). The results demonstrated the presence of negligible interference between the three targets, indicating that AFP, CEA, and PSA could be quantified individually in a single run without interference from each other. The responses of our probes to species in blood were tested to further validate selectivity (Figure 3). The concentrations of the possible interference were five times the target concentration. Blank plasma was prepared by removing PSA, CEA, and AFP with an ultrafiltration tube with a molecular weight cutoff of 3.0 kDa. The  $nC_{im}$  values of the species, including blank plasma, were close to those of PBS and smaller than those of the targets, indicating the good selectivity of our probes.

**Sensing Performance.** The responses of our probes to the three targets in PBS were measured to assess sensitivity. Figure 4 presents the relationship between the normalized immuno-

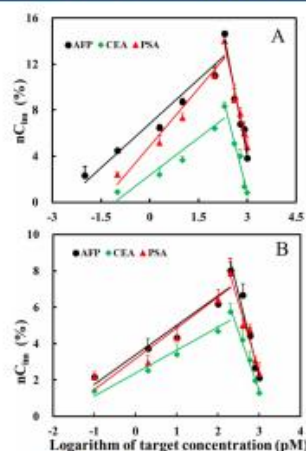


**Figure 4.** Plot of the normalized counts of immunocomplexes against the concentration of the targets in PBS buffer (A) and in blank plasma (B).

complex counts and target concentrations. The curves had an inverted V shape. These V-shaped working curves have been found in our previous homogeneous immunoassays at the single-particle level.<sup>12,15,16</sup> We have also elaborated on the reasons for and how to use the curves. In brief, the target–probe compounds began to form when the targets were in amounts that were excessive for the probes. With the increase in target concentration, the formation of the target–probe compounds increased and that of probe–target–probe compounds decreased, resulting in the reduction in  $nC_{im}$ . The  $nC_{im}$  values of a sample and a sample spiked with the target were needed to identify the appropriate curve for the sample. If the  $nC_{im}$  of the spiked sample was large, the curve with the positive slope was appropriate for the sample. Otherwise, the curve with the negative slope was used. The LODs for AFP, CEA, and PSA were estimated to be 10, 30,

Table 1. Comparison between Values Measured by Us and by the Hospital

sample number	biomarker	values measured by the hospital (pM)	our values		
			plasma (nM)	spiked plasma (pM)	recovery (%)
1	CEA	184 ± 20	151 ± 36	585 ± 105	109 ± 22
	AFP	379 ± 45	166 ± 18	549 ± 174	96 ± 14
	PSA	106 ± 9	79 ± 11	506 ± 105	107 ± 12
2	CEA	2086 ± 222	2404 ± 408	4908 ± 356	104 ± 9
	AFP	2407 ± 185	2586 ± 117	4818 ± 393	93 ± 9
	PSA	356 ± 31	380 ± 59	730 ± 35	91 ± 2
3	CEA	3124 ± 382	3232 ± 369	5257 ± 412	84 ± 11
	AFP	779 ± 101	764 ± 149	1687 ± 165	115 ± 8
	PSA	60 ± 6	60 ± 22	150 ± 18	100 ± 17
4	CEA	23 ± 2	18 ± 1	55 ± 2	92 ± 3
	AFP	3571 ± 203	3218 ± 190	6261 ± 393	95 ± 16.5
	PSA	204 ± 18	201 ± 80	608 ± 50	102 ± 20
5	CEA	10 ± 2	13 ± 6	52 ± 4	97 ± 16
	AFP	47 ± 5	36 ± 14	114 ± 13	96 ± 17
	PSA	1024 ± 120	888 ± 210	2375 ± 248	93 ± 3

and 50 fM at a signal-to-noise ratio of 3, respectively. These values indicated that (1) our approach offered sensitivity comparable to multiplexed heterogeneous immunoassays,<sup>3,21–26</sup> having the advantages of short measurement time and easy operations, and (2) the sensitivity of our approach was improved by at least 10 times compared to the multiplexed homogeneous immunoassays.<sup>7–10</sup> The good performance of our immunoassay could be attributed to the accurate identification of each immunocomplex.

The responses of our probes to the three targets in 12.6% blank plasma were determined to further assess sensitivity. Figure 4 shows the plot of the  $nC_m$  values against the target concentration. The working curves in blank plasma were similar to those in PBS. The LODs for AFP, CEA, and PSA were estimated to be 0.02, 0.10, and 0.06 pM at a signal-to-noise ratio of 3, respectively. The excellent agreement of these values with those in PBS implied that our probes worked well in complex media.

**Clinical Sample Test.** The values of CEA, AFP, and PSA in human plasma measured by our approach were compared with those measured by the single-plexed ECL immunoassay used in hospitals to demonstrate the feasibility of our method in clinical applications. As shown in Table 1, our values basically agreed with those measured by the hospital, indicating that our probes were reliable in clinical practice.

## CONCLUSIONS

A triple-plexed homogeneous digital immunoassay was established on the basis of distinguishing core–satellite-structured immunocomplexes from unbound and nonspecifically bound probes through dark-field and fluorescence microscopy. AuNPs with diameters of 70 nm were used as the scattering tags, and QD 525, QD 585, and QD 655 were applied as the fluorescent tags. The immunocomplexes contained AuNPs and QDs and were therefore distinguishable from unbound and nonspecifically bound probes based on the overlap between the scattering zeroth-order dot and the fluorescent zeroth-order dot. The QDs inside immunocomplexes were further recognized in accordance with first-order streaks to identify biomarkers. Our results demonstrated that our approach worked well in distinguishing immunocomplexes from free and nonspecifically bound probes. The successful quantification of the three targets in five human plasma

samples verified the reliability of our method in clinical applications.

## ASSOCIATED CONTENT

### Supporting Information

The Supporting Information is available free of charge at <https://pubs.acs.org/doi/10.1021/acs.analchem.1c05269>.

Size-exclusion chromatographic graphs of the three fluorescent probes; typical spectral images of QD 525, QD 585, QD 655, and AuNPs; distributions of dot–streak distance of QD 525, QD 585, QD 655, and AuNPs; the reasons of the overlap between the zeroth-order dots of AuNPs and the QDs inside an immunocomplex; the ensemble intensity of fluorescent probes before and after immunoreaction; and experimental condition optimization (PDF)

## AUTHOR INFORMATION

### Corresponding Author

Hongwei Gai – School of Chemistry and Materials Science, Jiangsu Normal University, Xuzhou 221116 Jiangsu, China; [orcid.org/0000-0002-1069-9543](https://orcid.org/0000-0002-1069-9543); Email: [gai@jnu.edu.cn](mailto:gai@jnu.edu.cn)

### Authors

Xiaojun Liu – School of Chemistry and Materials Science, Jiangsu Normal University, Xuzhou 221116 Jiangsu, China  
Xinyi Lin – School of Chemistry and Materials Science, Jiangsu Normal University, Xuzhou 221116 Jiangsu, China  
Xiaoyan Pan – School of Medicine, the Second Affiliated Hospital of Zhejiang University, Hangzhou 310009 Zhejiang, China

Complete contact information is available at:

<https://pubs.acs.org/doi/10.1021/acs.analchem.1c05269>

### Author Contributions

<sup>§</sup>X.L. and X.L. contributed equally.

### Notes

The authors declare no competing financial interest.



## ■ ACKNOWLEDGMENTS

The authors thank the support from the Natural Science Foundation of China (NSFC 22174056, 21775057).

## ■ REFERENCES

- (1) Jones, A.; Dhanapala, L.; Kankanamuge, R. N. T.; Kumar, C. V.; Rudling, J. F. *Anal. Chem.* 2020, 92, 345–362.
- (2) Shen, Y.; Modha, S.; Tsutsui, H.; Mulchandani, A. *Biosens. Bioelectron.* 2021, 171, No. 112721.
- (3) Tabakman, S. M.; Lau, L.; Robinson, J. T.; Price, J.; Sherlock, S. P.; Wang, H.; Zhang, B.; Chen, Z.; Tangsombatvisit, S.; Jarrell, J. A.; Utz, P. J.; Dai, H. *Nat. Commun.* 2011, 2, No. 466.
- (4) Lin, C. T.; Zhang, Y. *Biosens. Bioelectron.* 2007, 22, 1197–1204.
- (5) Li, W.; Jiang, W.; Dai, S.; Wang, L. *Anal. Chem.* 2016, 88, 1578–1584.
- (6) Li, C.-Y.; Cao, D.; Qi, C.-B.; Kang, Y.-F.; Song, C.-Y.; Xu, D.-D.; Zheng, B.; Pang, D.-W.; Tang, H.-W. *Anal. Chem.* 2018, 90, 2639–2647.
- (7) Wang, Y.; Tang, L.-J.; Jiang, J.-H. *Anal. Chem.* 2013, 85, 9213–9220.
- (8) Kokko, T.; Liljenback, T.; Peltola, M. T.; Kokko, L.; Soukka, T. *Anal. Chem.* 2008, 80, 9763–9768.
- (9) Geißler, D.; Charbonniere, L. J.; Ziesel, R. F.; Butlin, N. G.; Loehmannsroeben, H.-G.; Hildebrandt, N. *Angew. Chem., Int. Ed.* 2010, 49, 1396–1401.
- (10) Geißler, D.; Stüßler, S.; Loehmannsroeben, H.-G.; Hildebrandt, N. *J. Am. Chem. Soc.* 2013, 135, 1102–1109.
- (11) Chen, J. S.; Chen, P. F.; Lin, H. T. H.; Huang, N.-T. *Analyst* 2020, 145, 7654–7661.
- (12) Liu, X.; Sun, Y.; Lin, X.; Pan, X.; Wu, Z.; Gai, H. *Anal. Chem.* 2021, 93, 3089–3095.
- (13) Chatterjee, T.; Knappik, A.; Sandford, E.; Tewari, M.; Choi, S. W.; Strong, W. B.; Thrush, E. P.; Oh, K. J.; Liu, N.; Walter, N. G.; Johnson-Buck, A. *Proc. Natl. Acad. Sci. U.S.A.* 2020, 117, 22815–22822.
- (14) Akama, K.; Noji, H. *Lab. Chip* 2020, 20, 2113–2121.
- (15) Liu, X.; Zhang, Y.; Liang, A.; Ding, H.; Gai, H. *Chem. Commun.* 2019, 55, 11442–11445.
- (16) Liu, X.; Huang, C.; Dong, X.; Liang, A.; Zhang, Y.; Zhang, Q.; Wang, Q.; Gai, H. *Chem. Commun.* 2018, 54, 13103–13106.
- (17) Liu, X.; Wu, Z.; Zhang, Q.; Zhao, W.; Zong, C.; Gai, H. *Anal. Chem.* 2016, 88, 2119–2124.
- (18) Liu, X.; Wu, Z.; Lin, X.; Bu, W.; Qin, L.; Gai, H. *Analyst* 2021, 146, 3034–3040.
- (19) Shi, X.; Meng, X.; Sun, L.; Liu, J.; Zheng, J.; Gai, H.; Yang, R.; Yeung, E. S. *Lab. Chip* 2010, 10, 2844–2847.
- (20) Liu, X.; Zhang, Q.; Tu, Y.; Zhao, W.; Gai, H. *Anal. Chem.* 2013, 85, 11851–11857.
- (21) Shi, X.; Li, M.; Zhao, W.; Liang, A.; Liu, X.; Gai, H. *Sens. Actuators, B* 2015, 207, 308–312.
- (22) Shi, X.; Xie, Z.; Song, Y.; Tan, Y.; Yeung, E. S.; Gai, H. *Anal. Chem.* 2012, 84, 1504–1509.
- (23) Bai, X.-R.; Wang, L.-H.; Ren, J.-Q.; Bai, X.-W.; Zeng, L.-W.; Shen, A.-G.; Hu, J.-M. *Anal. Chem.* 2019, 91, 2955–2963.
- (24) Liu, B.; Zhao, X.; Jiang, W.; Fu, D.; Gu, Z. *Nanoscale* 2016, 8, 17465–17471.
- (25) Lee, J. U.; Nguyen, A. H.; Sim, S. J. *Biosens. Bioelectron.* 2015, 74, 341–346.
- (26) Chen, R.; Liu, B.; Ni, H.; Chang, N.; Luan, C.; Ge, Q.; Dong, J.; Zhao, X. *Analyst* 2019, 144, 4051–4059.

## ■ Recommended by ACS

## Digital Duplex Homogeneous Immunoassay by Counting Immunocomplex Labeled with Quantum Dots

Xiaojuan Liu, Hongwei Gai, et al.

FEBRUARY 04, 2021

ANALYTICAL CHEMISTRY

READ

## Self-Validated Homogeneous Immunoassay by Single Nanoparticle in-Depth Scrutinization

Zili Huang, Yili Lv, et al.

JANUARY 08, 2020

ANALYTICAL CHEMISTRY

READ

## Single-Particle Mobility Analysis Enables Ratiometric Detection of Cancer Markers under Darkfield Tracking Microscopy

Yancao Chen, Xiao-Bing Zhang, et al.

JULY 06, 2020

ANALYTICAL CHEMISTRY

READ

## Rapid, Cost-Effective Peptide/Nucleic Acid-Based Platform for Therapeutic Antibody Monitoring in Clinical Samples

Marco Mosenig, Rudy Ippolito, et al.

SEPTEMBER 10, 2020

ACCS SENSORS

READ

Get More Suggestions &gt;



## 4、工作站条件保障

### 4.1 外聘专家聘书





## 4.2 知识产权情况

证书号 第5715770号





# 发明专利证书

发明名称：一种基于银纳米三角与 Ag<sup>+</sup>协同体系的 As(III)检测方法

发明人：宗成华;赵文峰;金潇婷;吕氏

专利号：ZL 2020 1 1405334.9

专利申请日：2020 年 12 月 03 日

专利权人：江苏师范大学

地址：221116 江苏省徐州市铜山新区上海路 101 号

授权公告日：2023 年 01 月 31 日      授权公告号：CN 112540080 B

国家知识产权局依照中华人民共和国专利法进行审查，决定授予专利权，颁发发明专利证书并在专利登记簿上予以登记。专利权自授权公告之日起生效。专利权期限为二十年，自申请日起算。

专利证书记载专利权登记时的法律状况。专利权的转移、质押、无效、终止、恢复和专利权人的姓名或名称、国籍、地址变更等事项记载在专利登记簿上。



局长  
申长雨





第 1 页 (共 2 页)

其他事项参见续页

证书号 第 5715770 号

专利权人应当依照专利法及其实施细则规定缴纳年费。本专利的年费应当在每年 12 月 03 日前缴纳。未按照规定缴纳年费的，专利权自应当缴纳年费期满之日起终止。

申请日时本专利记载的申请人、发明人信息如下：

申请人：

江苏师范大学

发明人：

宗成华; 赵文峰; 金满婷; 吕氏



证书号 第5902750号



## 发明专利证书

发 明 名 称：一种呼出气冷凝液及血清中甲醛的检测方法

发 明 人：宗成华;葛梦怡;于洋

专 利 号：ZL 2021 1 0504019.X

专 利 申 请 日：2021年05月10日

专 利 权 人：江苏师范大学

地 址：221116 江苏省徐州市铜山新区上海路101号

授 权 公 告 日：2023年04月21日

授 权 公 告 号：CN 113237865 B

国家知识产权局依照中华人民共和国专利法进行审查，决定授予专利权，颁发发明专利证书并在专利登记簿上予以登记。专利权自授权公告之日起生效。专利权期限为二十年，自申请日起算。

专利证书记载专利权登记时的法律状况。专利权的转移、质押、无效、终止、恢复和专利权人的姓名或名称、国籍、地址变更等事项记载在专利登记簿上。



局长  
申长雨

申长雨



第1页(共2页)

其他事项参见续页

证书号第5902750号

专利权人应当依照专利法及其实施细则规定缴纳年费。本专利的年费应当在每年05月10日前缴纳。未按照规定缴纳年费的，专利权自应当缴纳年费期满之日起终止。

申请日时本专利记载的申请人、发明人信息如下：

申请人：

江苏师范大学

发明人：

宗成华;葛梦怡;于洋



证书号 第6384279号



## 发明专利证书

发 明 名 称：一种基于微流控液滴的核壳二氧化硅微球制备方法

发 明 人：盖宏伟;钟紫茵;张清泉;范雨欣;李依洛

专 利 号：ZL 2022 1 0291957.0

专 利 申 请 日：2022年03月23日

专 利 权 人：江苏师范大学

地 址：221116 江苏省徐州市铜山新区上海路101号

授 权 公 告 日：2023年10月03日

授 权 公 告 号：CN 114699999 B

国家知识产权局依照中华人民共和国专利法进行审查，决定授予专利权，颁发发明专利证书并在专利登记簿上予以登记。专利权自授权公告之日起生效。专利权期限为二十年，自申请日起算。

专利证书记载专利权登记时的法律状况。专利权的转移、质押、无效、终止、恢复和专利权人的姓名或名称、国籍、地址变更等事项记载在专利登记簿上。



局长  
申长雨

申长雨



第1页(共2页)

其他事项参见续页

证书号第6384279号

专利权人应当依照专利法及其实施细则规定缴纳年费。本专利的年费应当在每年03月23日前缴纳。未按照规定缴纳年费的，专利权自应当缴纳年费期满之日起终止。

申请日时本专利记载的申请人、发明人信息如下：

申请人：

江苏师范大学

发明人：

盖宏伟;钟紫茵;张清泉;范雨欣;李依洛

证书号 第6552345号



## 发明专利证书

发 明 名 称: 一种肿瘤基因检测试剂盒组装设备

发 明 人: 卜令斌;张瑞;柴艳群;刘秀财;曹金梁;祝田

专 利 号: ZL 2023 1 0627674.3

专利申请日: 2023年05月30日

专 利 权 人: 阔然医学检验实验室(徐州)有限公司

地 址: 221000 江苏省徐州市淮海国际港务区徐州永嘉科技园B  
07号楼-1-102号1-3层

授权公告日: 2023年12月12日

授权公告号: CN 116571982 B

国家知识产权局依照中华人民共和国专利法进行审查, 决定授予专利权, 颁发发明专利证书并在专利登记簿上予以登记。专利权自授权公告之日起生效。专利权期限为二十年, 自申请日起算。

专利证书记载专利权登记时的法律状况。专利权的转移、质押、无效、终止、恢复和专利权人的姓名或名称、国籍、地址变更等事项记载在专利登记簿上。



局长  
申长雨

申长雨



第1页(共2页)

其他事项参见续页



证书号第6552345号

专利权人应当依照专利法及其实施细则规定缴纳年费。本专利的年费应当在每年05月30日前缴纳。  
未按照规定缴纳年费的，专利权自应当缴纳年费期满之日起终止。

申请日时本专利记载的申请人、发明人信息如下：

申请人：  
    罔然医学检验实验室（徐州）有限公司

发明人：  
    卜令斌;张瑞;柴艳群;刘秀财;曹金梁;祝田

证书号 第18594275号



## 实用新型专利证书

实用新型名称：一种微生物样本灭活处理箱

发 明 人：刘秀财;卜令斌;董新波

专 利 号：ZL 2022 2 1482435.0

专 利 申 请 日：2022年06月15日

专 利 权 人：阔然医学检验实验室（徐州）有限公司

地 址：221000 江苏省徐州市泉山区徐州永嘉科技园B07号楼-1-1  
02号1-3层

授 权 公 告 日：2023年03月14日

授 权 公 告 号：CN 218620807 U

国家知识产权局依照中华人民共和国专利法经过初步审查，决定授予专利权，颁发实用新型专利证书并在专利登记簿上予以登记。专利权自授权公告之日起生效。专利权期限为十年，自申请日起算。

专利证书记载专利权登记时的法律状况。专利权的转移、质押、无效、终止、恢复和专利权人的姓名或名称、国籍、地址变更等事项记载在专利登记簿上。



局长  
申长雨

申长雨



第1页(共2页)

其他事项参见续页

证书号第18594275号

专利权人应当依照专利法及其实施细则规定缴纳年费。本专利的年费应当在每年06月15日前缴纳。未按照规定缴纳年费的，专利权自应当缴纳年费期满之日起终止。

申请日时本专利记载的申请人、发明人信息如下：

申请人：

嗣然医学检验实验室（徐州）有限公司

发明人：

刘秀财;卜令斌;董新波



证书号 第20493195号



## 实用新型专利证书

实用新型名称：一种肿瘤基因检测取样装置

发 明 人：卜令斌;柴艳群;张瑞;曹金梁;祝田;刘秀财

专 利 号：ZL 2023 2 1815563.7

专 利 申 请 日：2023年07月11日

专 利 权 人：阔然医学检验实验室（徐州）有限公司

地 址：221000 江苏省徐州市淮海国际港务区徐州永嘉科技园B  
07号楼-1-102号1-3层

授 权 公 告 日：2024年02月20日

授 权 公 告 号：CN 220508484 U

国家知识产权局依照中华人民共和国专利法经过初步审查，决定授予专利权，颁发实用新型专利证书并在专利登记簿上予以登记。专利权自授权公告之日起生效。专利权期限为十年，自申请日起算。

专利证书记载专利权登记时的法律状况。专利权的转移、质押、无效、终止、恢复和专利权人的姓名或名称、国籍、地址变更等事项记载在专利登记簿上。



局长  
申长雨

申长雨



第1页(共2页)

其他事项参见续页

证书号第20493195号

专利权人应当依照专利法及其实施细则规定缴纳年费。本专利的年费应当在每年07月11日前缴纳。未按照规定缴纳年费的，专利权自应当缴纳年费期满之日起终止。

申请日时本专利记载的申请人、发明人信息如下：

申请人：

隅然医学检验实验室（徐州）有限公司

发明人：

卜令斌;柴艳群;张瑞;曹金梁;祝田;刘秀财

证书号 第20561678号



## 实用新型专利证书

实用新型名称：一种肿瘤基因检测试剂存放箱

发 明 人：卜令斌;张瑞;柴艳群;刘秀财;曹金梁;祝田

专 利 号：ZL 2023 2 2055211.2

专 利 申 请 日：2023年08月01日

专 利 权 人：阔然医学检验实验室（徐州）有限公司

地 址：221000 江苏省徐州市淮海国际港务区徐州永嘉科技园B  
07号楼-1-102号1-3层

授 权 公 告 日：2024年03月12日

授 权 公 告 号：CN 220577811 U

国家知识产权局依照中华人民共和国专利法经过初步审查，决定授予专利权，颁发实用新型专利证书并在专利登记簿上予以登记。专利权自授权公告之日起生效。专利权期限为十年，自申请日起算。

专利证书记载专利权登记时的法律状况。专利权的转移、质押、无效、终止、恢复和专利权人的姓名或名称、国籍、地址变更等事项记载在专利登记簿上。



局长  
申长雨

申长雨



第1页(共2页)

其他事项参见续页



证书号第20561678号

专利权人应当依照专利法及其实施细则规定缴纳年费。本专利的年费应当在每年08月01日前缴纳。未按照规定缴纳年费的，专利权自应当缴纳年费期满之日起终止。

申请日时本专利记载的申请人、发明人信息如下：

申请人：

固然医学检验实验室（徐州）有限公司

发明人：

卜令斌;张瑞;柴艳群;刘秀财;曹金梁;祝田

证书号第20918180号



## 实用新型专利证书

实用新型名称：一种肿瘤基因检测用的样品保存装置

发 明 人：卜令斌;刘秀财;曹金梁;祝田;柴艳群;张瑞

专 利 号：ZL 2023 2 2595609.5

专 利 申 请 日：2023年09月22日

专 利 权 人：阔然医学检验实验室（徐州）有限公司

地 址：221000 江苏省徐州市徐州淮海国际港务区徐州永嘉科技园B07号楼-1-102号1-3层

授 权 公 告 日：2024年05月10日 授 权 公 告 号：CN 220925078 U

国家知识产权局依照中华人民共和国专利法经过初步审查，决定授予专利权，颁发实用新型专利证书并在专利登记簿上予以登记。专利权自授权公告之日起生效。专利权期限为十年，自申请日起算。

专利证书记载专利权登记时的法律状况。专利权的转移、质押、无效、终止、恢复和专利权人的姓名或名称、国籍、地址变更等事项记载在专利登记簿上。



局长  
申长雨

申长雨



第1页(共2页)

其他事项参见续页

证书号第20918180号

专利权人应当依照专利法及其实施细则规定缴纳年费。本专利的年费应当在每年09月22日前缴纳。未按照规定缴纳年费的，专利权自应当缴纳年费期满之日起终止。

申请日时本专利记载的申请人、发明人信息如下：

申请人：

固然医学检验实验室（徐州）有限公司

发明人：

卜令斌;刘秀财;曹金梁;祝田;柴艳群;张瑞



证书号 第20882222号



## 实用新型专利证书

实用新型名称：一种防止肿瘤基因检测设备晃动的支撑设备

发 明 人：卜令斌;柴艳群;刘秀财;张瑞;曹金梁;祝田

专 利 号：ZL 2023 2 2690903.4

专 利 申 请 日：2023年10月08日

专 利 权 人：阔然医学检验实验室（徐州）有限公司

地 址：221000 江苏省徐州市淮海国际港务区徐州永嘉科技园B  
07号楼-1-102号1-3层

授 权 公 告 日：2024年05月03日

授 权 公 告 号：CN 220891589 U

国家知识产权局依照中华人民共和国专利法经过初步审查，决定授予专利权，颁发实用新型专利证书并在专利登记簿上予以登记。专利权自授权公告之日起生效。专利权期限为十年，自申请日起算。

专利证书记载专利权登记时的法律状况。专利权的转移、质押、无效、终止、恢复和专利权人的姓名或名称、国籍、地址变更等事项记载在专利登记簿上。



局长  
申长雨

申长雨



第1页(共2页)

其他事项参见续页

证书号第20918180号

专利权人应当依照专利法及其实施细则规定缴纳年费。本专利的年费应当在每年09月22日前缴纳。未按照规定缴纳年费的，专利权自应当缴纳年费期满之日起终止。

申请日时本专利记载的申请人、发明人信息如下：

申请人：

阔然医学检验实验室（徐州）有限公司

发明人：

卜令斌;刘秀财;曹金梁;祝田;柴艳群;张瑞

中华人民共和国国家版权局  
计算机软件著作权登记证书

证书号： 软著登字第5940403号

软件名称： 阔然医学基因高通量测序信息化管理系统  
V1.0

著作权人： 阔然医学检验实验室（徐州）有限公司

开发完成日期： 2020年01月01日

首次发表日期： 未发表

权利取得方式： 原始取得

权利范围： 全部权利

登记号： 2020SR1061707

根据《计算机软件保护条例》和《计算机软件著作权登记办法》的规定，经中国版权保护中心审核，对以上事项予以登记。



No. 06383601



2020年09月08日



中华人民共和国国家版权局  
计算机软件著作权登记证书

证书号： 软著登字第5940396号

软件名称： 阔然基因医学突变融合检测流程分析软件  
V1.0

著作权人： 阔然医学检验实验室（徐州）有限公司

开发完成日期： 2019年12月20日

首次发表日期： 未发表

权利取得方式： 原始取得

权利范围： 全部权利

登记号： 2020SR1061700

根据《计算机软件保护条例》和《计算机软件著作权登记办法》的规定，经中国版权保护中心审核，对以上事项予以登记。



No. 06383600



2020年09月08日

中华人民共和国国家版权局  
计算机软件著作权登记证书

证书号： 软著登字第11325761号

软件名称： 癌症靶点试剂研发项目运营系统  
V1.0

著作权人： 阔然医学检验实验室（徐州）有限公司

开发完成日期： 2023年05月15日

首次发表日期： 未发表

权利取得方式： 原始取得

权利范围： 全部权利

登记号： 2023SR0738590

根据《计算机软件保护条例》和《计算机软件著作权登记办法》的规定，经中国版权保护中心审核，对以上事项予以登记。



No. 13120314



2023年06月28日



中华人民共和国国家版权局  
计算机软件著作权登记证书

证书号： 软著登字第11325762号

软件名称： 肿瘤基因检测大数据可视化分析软件  
V1.0

著作权人： 阔然医学检验实验室（徐州）有限公司

开发完成日期： 2023年05月19日

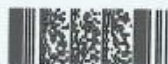
首次发表日期： 未发表

权利取得方式： 原始取得

权利范围： 全部权利

登记号： 2023SR0738591

根据《计算机软件保护条例》和《计算机软件著作权登记办法》的规定，经中国版权保护中心审核，对以上事项予以登记。



No. 13120315



2023年06月28日



中华人民共和国国家版权局  
计算机软件著作权登记证书

证书号： 软著登字第12149063号

软件名称： 脑胶质瘤检测标志物筛选系统  
V1.0

著作权人： 阔然医学检验实验室（徐州）有限公司

开发完成日期： 2023年08月11日

首次发表日期： 未发表

权利取得方式： 原始取得

权利范围： 全部权利

登记号： 2023SR1561890

根据《计算机软件保护条例》和《计算机软件著作权登记办法》的规定，经中国版权保护中心审核，对以上事项予以登记。



2023年12月05日

中华人民共和国国家版权局  
计算机软件著作权登记证书

证书号： 软著登字第12149079号

软件名称： 肝癌检测技术临床应用软件  
V1.0

著作权人： 阔然医学检验实验室（徐州）有限公司

开发完成日期： 2023年09月09日

首次发表日期： 未发表

权利取得方式： 原始取得

权利范围： 全部权利

登记号： 2023SR1561906

根据《计算机软件保护条例》和《计算机软件著作权登记办法》的规定，经中国版权保护中心审核，对以上事项予以登记。



2023年12月05日



中华人民共和国国家版权局  
计算机软件著作权登记证书

证书号： 软著登字第12149089号

软件名称： 个体化肿瘤基因检测与精准治疗系统  
V1.0

著作权人： 阔然医学检验实验室（徐州）有限公司

开发完成日期： 2023年06月24日

首次发表日期： 未发表

权利取得方式： 原始取得

权利范围： 全部权利

登记号： 2023SR1561916

根据《计算机软件保护条例》和《计算机软件著作权登记办法》的规定，经中国版权保护中心审核，对以上事项予以登记。



2023年12月05日



中华人民共和国国家版权局  
计算机软件著作权登记证书

证书号： 软著登字第12149105号

软件名称： 癌症靶点试剂开发应用软件  
V1.0

著作权人： 阔然医学检验实验室（徐州）有限公司

开发完成日期： 2023年04月14日

首次发表日期： 未发表

权利取得方式： 原始取得

权利范围： 全部权利

登记号： 2023SR1561932

根据《计算机软件保护条例》和《计算机软件著作权登记办法》的规定，经中国版权保护中心审核，对以上事项予以登记。



2023年12月05日

中华人民共和国国家版权局  
计算机软件著作权登记证书

证书号： 软著登字第12182709号

软件名称： 肿瘤基因检测技术研究平台  
V1.0

著作权人： 阔然医学检验实验室（徐州）有限公司

开发完成日期： 2023年05月16日

首次发表日期： 未发表

权利取得方式： 原始取得

权利范围： 全部权利

登记号： 2023SR1595536

根据《计算机软件保护条例》和《计算机软件著作权登记办法》的规定，经中国版权保护中心审核，对以上事项予以登记。



2023年12月08日



#### 4.3 实验环境及仪器展示





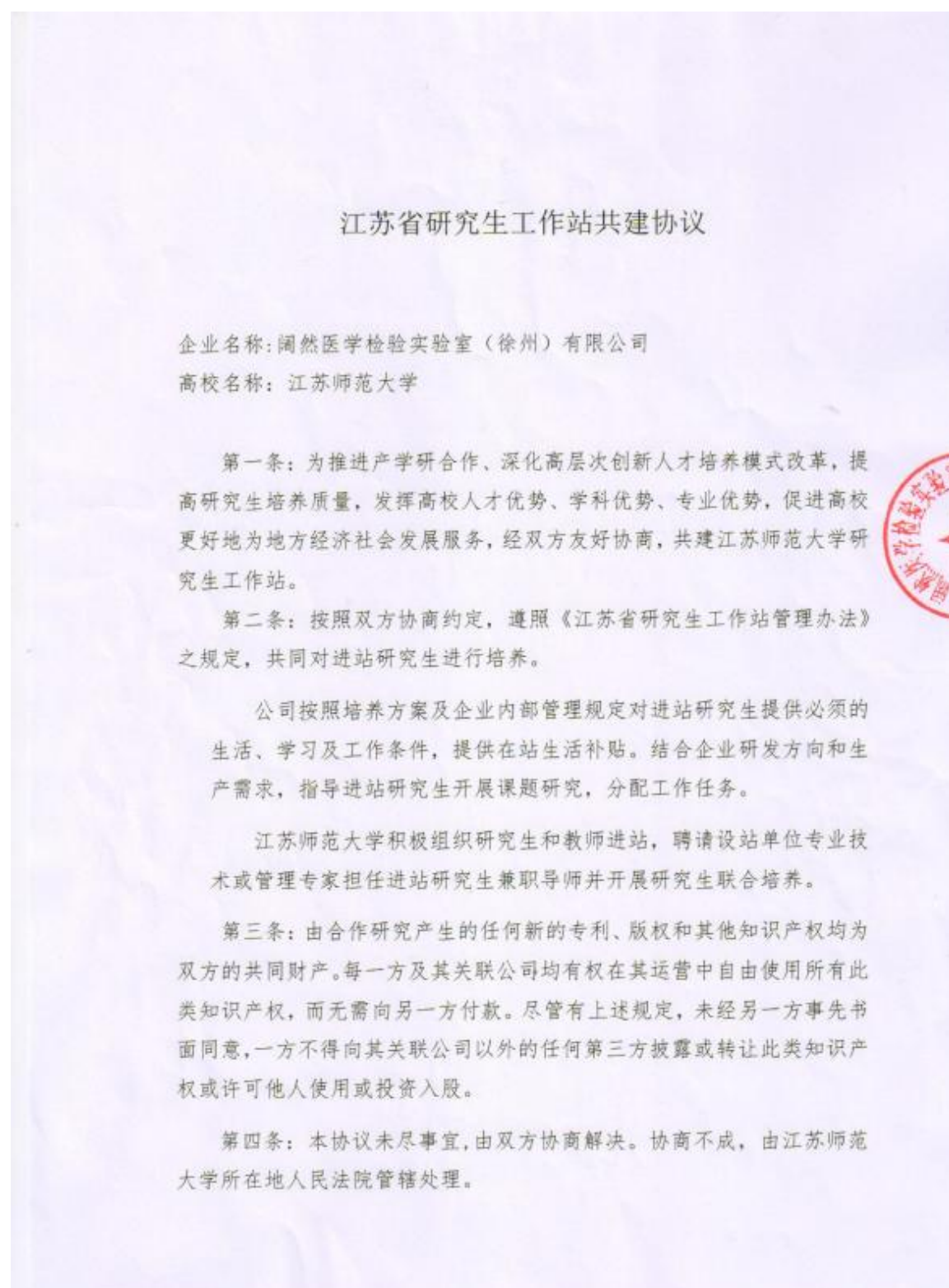






## 5、共建协议

### 5.1 江苏省研究生工作站共建协议





第五条：本协议正式文本一式二份，协议双方各执一份。

企业名称（盖章）



高校名称（盖章）



企业法定代表人签章：



高校负责人签章：

周汝光

2024 年 6 月 1 日

2024 年 6 月 1 日